Title
Cellular Adhesion and Molecular Transport: Stochastic Phenomena

Author
Lin, KuanPo

Publication Date
2021

UNIVERSITY OF CALIFORNIA SAN DIEGO

Cellular Adhesion and Molecular Transport: Stochastic Phenomena

A dissertation submitted in partial satisfaction of the
requirements for the degree Doctor of Philosophy

in

Structural Engineering

by

Kuan-Po Lin

Committee in charge:

Professor Robert J. Asaro, Chair
Professor Pedro J. Cabrales Arevalo
Professor Jiun-Shyan Chen
Professor Shabnam J. Semnani
Professor Qiang Zhu

2021

The Dissertation of Kuan-Po Lin is approved, and it is acceptable in quality and form for publication on microfilm and electronically.

University of California San Diego

2021

DEDICATION

I dedicate my dissertation work to my family and many friends. Without their constant support this dissertation was not possible.

I am thankful for all the ones guiding me and motivating me throughout my life.

I dedicate this dissertation to all the people in my life who touch my heart.

TABLE OF CONTENTS

LIST OF FIGURES

LIST OF TABLES

ACKNOWLEDGEMENTS

I would first like to express my deepest appreciation to Professor Robert Asaro for his consistent support and guidance throughout these years. Professor Asaro continuously provide invaluable advice and was always willing and enthusiastic to assist in any way he could during this research. I would like to extend my gratitude to Professor Qiang Zhu for collaboration. Furthermore, I'm extremely grateful to my committee, for their practical suggestions and thoughtful comments on this dissertation.

I would also like to thank the colleagues and all the staffs in the Structural Engineering department, for the relentless support and opportunities. In addition, it is a pleasure to thank my friends for the wonderful times we shared, especially the Friday night dinners.

Finally, my deep and sincere gratitude to my parents for their unconditional trust, timely encouragement and unparalleled love. I am grateful to my sister for always being there for me as a friend. Thanks again to everyone who made this dissertation and me possible.

Chapter 2, in full, is a reprint of the material as it appears in *Biophysical journal* 117.9 (2019): 1599-1614. Asaro, Robert; Lin, Kuan-Po; Zhu, Qian, 2019. The dissertation author was the primary investigator and author of this paper.

Chapter 3, in part is currently being prepared for submission for publication of the material. Lin, Kuan-Po; Asaro, Robert. The dissertation author was the primary investigator and author of this material.

Chapter 4, in full, is a reprint of the material as it appears in *Physical Review E* 97.4 (2018): 042401. Asaro, Robert; Zhu, Qian; Lin, Kuan-Po, 2017. The dissertation author was the primary investigator and author of this paper.

VITA

2009-2013	B.S. in Civil Engineering, National Taiwan University
2013-2015	M.S. in Civil Engineering, National Taiwan University
2016-2017	Graduate Research Assistant, University of California San Diego
2017-2021	Graduate Teaching Assistant, University of California San Diego
2021	Ph. D. in Structural Engineering, University of California San Diego

PUBLICATIONS

"Diffusion-advection within dynamic biological gaps driven by structural motion." *Physical Review E* 97.4 (2018): 042401.
"Mechanosensitivity occurs along the adhesome's force train and affects traction stress." *Biophysical journal* 117.9 (2019): 1599-1614.
"Nascent adhesion clustering: integrin-integrin and integrin-substrate interactions" *Biophysica* (Prepared)

ABSTRACT OF THE DISSERTATION

Cellular Adhesion and Molecular Transport: Stochastic Phenomena

by

Kuan-Po Lin

Doctor of Philosophy in Structural Engineering

University of California San Diego, 2021

Professor Robert J. Asaro, Chair

The stochastic nature of many fundamental cellular mechanisms such as adhesion, the development of traction forces, and of molecular transport is quite different than typical deterministic structures. Biological structures are truly stochastic in their basic function even when subjected to purely deterministic applied loading. Herein are discussed two areas of vital biological cellular processes, *viz.* 1) adhesion and the development of traction force and 2) molecular transport.

Cell adhesion is important for cells to sense and react to the environments. The process of force development along the adhesome within cell focal adhesions is specifically considered. A holistic analysis is presented that explicitly includes the role of a major set of force-bearing proteins involved in force transmission along a "model adhesome" and that leads to the development of traction stress. Our analysis provides a rational description for the various levels of traction stresses that have been reported and of the effect of substrate stiffness. Our approach has the advantage of being quite clear as to how each constituent contributes to the net development of force and traction stress.

Nascent adhesions are general precursor to the formation of focal adhesions. Nascent adhesions form when cells come into contact with substrates at all rigidities and generally involve the clustering of ligated integrins that may recruit un-ligated integrins. The flexible, adaptable model we present provides a clear explanation of how these conserved cluster features come about. Our model is based on the interaction among ligated and un-ligated integrins that arise due to deformations that are induced in the cell membrane-cell glycocalyx and substrate system due to integrin activation and ligation. Our simulations reveal effects of various key parameters related to integrin activation and ligation as well as some unexpected and previously unappreciated effects of parameters including integrin mobility and substrate rigidity.

To study the significance of advection in the transport of solutes, or particles, within thin biological gaps(channels), we theoretically examine the process driven by stochastic fluid flow caused by random thermal structural motion and compare it with transport *via* diffusion. The model geometry chosen resembles the synaptic cleft. Our model analysis thus provides unambiguous insight into the prospect of competition of advection *vs.* diffusion within biological gap-like structures. The importance of the random, versus a regular, nature of structural motion and of the resulting transient nature of advection under random motion are made clear in our analysis.

Chapter 1

Introduction

This thesis contains the results of a number of studies of fundamental cellular mechanisms such as adhesion, the development of traction forces cell's impose on substrates they adhere to, and of molecular transport. Throughout these developments the stochastic nature of the various elements involved in these processes will become evident. Hence the analysis involved is quite different than that typical of more deterministic structures such as civil structures. In the latter case typical random variables may include loading such as stochastic seismic loading whereas the response of the structural elements is essentially deterministic. For biological, *e.g.* cellular, structures both loading (*i.e.* the mechanical stimuli) and the basic response of the structural elements are generally stochastic in nature. For this reason a brief discussion is given of the stochastic nature of two such elements, *viz.* 1) the stochastic unfolding-refolding of talin that plays a strong role in cell adhesion and 2) molecular bonding *via* the so-called *catch bond* such as in integrins, an important class of cell adhesion molecules (CAMS). These brief discussions should be of value to make the more detailed presentations of Chapter 2, 3 and 4.

1.1 Overview

This thesis will present the findings of three basic studies of phenomena critical and common to a nearly ubiquitous line of cell types; in particular, herein are discussed studies of cell adhesion, vital to cell motility, and of molecular transport. As it happens, and as noted above, a common theme in these three studies is the stochastic nature of the mechanisms involved at various, if not at all, the steps and stages of the processes involved. Viewed as structures, it will be appreciated that biological structures, by the nature of their various components, are not deterministic as, for example civil structures, but are truly stochastic in their basic function when subjected to applied loading; we will see by examples that this loading may also be random, yet we will see that the response of the "structure" itself is stochastic even when subject to deterministic forms of loading.

Cell adhesion and the development of traction force is presented first in Chapter 2, where the process of cell migration driven by traction forces, is metaphorically described as a river raft being towed atop a river bottom. This rough analogy makes clear the importance of the stochastic nature of the attachments of "ropes" and "anchors" and even the stochastic mechanisms of attachments and anchoring *vs.*, on the other hand, the simple deterministic nature attaching and anchoring in an actual river raft.

The second main presentation addresses the basic process of *nascent adhesion* formation, *i.e.* the process by which cellular adhesions initiate; this is presented in Chapter 3. This process involves force affected diffusion of integrins - molecules that serve as mobile anchors - as controlled by their ability to deform a cell's membrane. This leads to clustering of integrins attached to adhesion proteins such as talin that is also included in the earlier study of adhesions. Here it is shown, as also in the discussion of adhesion, that the bonding of integrins is itself stochastic as it is, in fact a reversible chemical reaction. This introduces the idea of *expectation times for bonding* and stochastic response, as opposed to permanent bonds. The development of interactions among integrins driven by their ability to deform cell membranes is an entirely novel theoretical development described in Chapter 3.

In Chapter 4, a treatment of stochastic force driven diffusion-advection is presented. The specific context is diffusion-advection driven by thermally driven motion of a synapse.

The stochastic, thermally driven motion of the synapse creates a random fluid flow advection-diffusion process that mediates molecular transport. The concept and methods introduced, however, are more generally applicable to diffusion-advection processes in biological cellular system.

To set the stage for Chapters 2, 3, and 4, I first briefly describe the basic stochastic nature of two elements of our processes of cellular adhesion, *viz.* the mechanical response of talin and the operation of a catch bond that is typical of integrins.

1.2 Overview of mechanosensing train

Cell adhesion is essential for cells to sense and respond to the biophysical properties of the environment. Mechanotransduction, induced by the retrograde flow of the cell's intracellular actin cytoskeleton (*aka* hereafter "actin") *via* a series of proteins [7–9] that are bound, from the cell's nucleus, to each other and ultimately to the cell's extracellular matrix is essential to the process of cell differentiation [7–9]. The transmitted forces to the nucleus stimulate gene expression and thereby mediate cell differentiation. We consider a model that contains actin(myosin)-vinculin-talin-integrin-ligand(extracelular matrix)-substrate as the basis of the so called *force-train* that stimulates mechanotransduction. It is by the action of the force train, *aka* the *adhesome*, that traction forces and stresses are developed. As noted, the current study will follow an essential, yet detailed, account of a model adhesome's force-train with account given to the major players, including the actin(myosin) cytoskeleton, talin, vinculin, integrins, and ligands that are incorporated into the extracellular matrix. Vinculin provides for the essential bonding of talin to the actin cytoskeleton. Indeed, analysis of the key elements demonstrates mechanosensitivity within each element, *e.g.* at each stage in the process of force generation effects of substrate rigidity are observed. We shall also point out a number of mediating effects of the substrate in addition to its simple rigidity. We now provide additional perspective by using Fig. 1.1, that depicts a sort of metaphorical representation of the force train as it operates in a cell's migration. The metaphor of a river raft is used for this purpose.

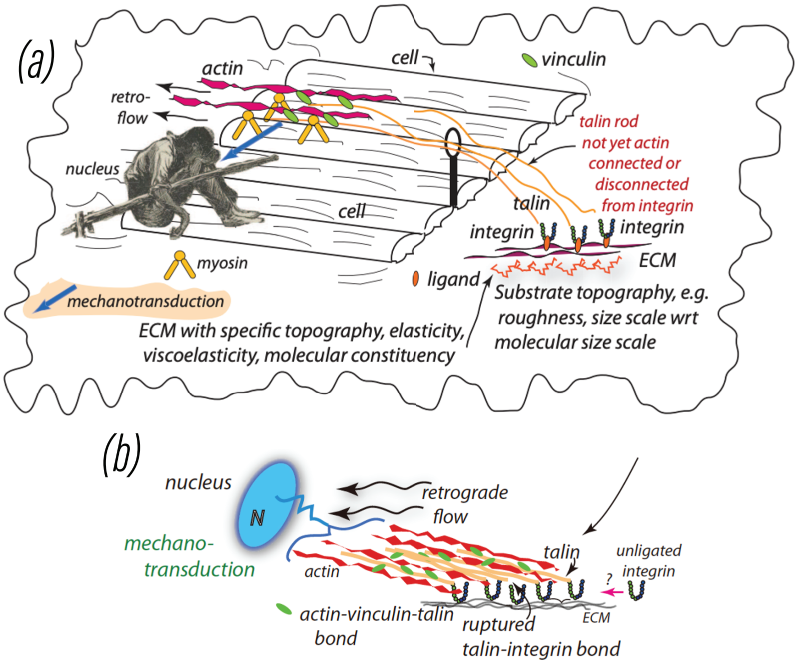

Figure 1.1. (a) The actin-vinculin-talin-integrin-ligand-substrate adhesome as we consider it *vis-à-vis* cell traction forces and stresses driving cell migration. The figure of a man represents the cell nucleus subject to mechanotransductive stimuli (blue arrow) from the forces within the skeleton. (b) The adhesome in a cell. Actin is in red attached to talin *via* vinculin; talin is attached to integrins that then bond to ECM ligands.

Actual river rafts, such as depicted in Fig. 1.1 are anchored, or propelled, by the action of their human engines (identified with the cell's myosin/actin cytoskeleton) throwing out ropes (identified with talin) with attached anchors (identified with integrins) that sink to the river bottom (that is identified with the ECM) where the anchors "catch" on to nooks and crannies (identified with the ECM's ligands) lying within the river bottom. Clearly the physical nature of the river bottom, *e.g.* its topology and roughness, stiffness and the presence of nooks and crannies amenable to being "hooked" will play strong roles in establishing secure anchorage or generating sufficient forces for propulsion. Now a cell behaves in a somewhat reversed fashion, yet viewing the cell as a river raft, we envision that as anchors fix onto (*i.e.* bond to) to the ECM (river bottom), talin rods (ropes) are activated and then bind to integrins and then bind to actin that is driven by myosin contractile motors. Note that when talin is disconnected either at actin, or at integrin/ligands, the substrate may relax to its unloaded state. Thus it is clearly important to know how the substrate will respond, most especially if it is time dependent, *e.g.* viscoelastic. The integrin-ligand-substrate anchorage is, however, the starting point for of mechano-sensitivity and transduction. This, in turn, involves far more than simply the "bulk stiffness" of the "substrate". It involves substrate/ECM features such as, *inter alia*, substrate topography, including nano-scale texture and roughness, and the patterning of all such features [10–17]. Indeed, the influence of surface topography has been known for over half a century [18] and yet there is essentially no mechanistic understanding of it to date. Hence, there are no clear guidelines for any cellular system for true *optimization* of substrate design for achieve specific outcomes. This is clearly a most pointed and vital area that needs focused attention as has also been pointed out by Lord *et al.* [10]. Hence, it is vital to understand the operation of talin and the mechanisms of its binding (*i.e.* attachment) to actin and to integrins and their bounding to the ligands of the ECM.

1.3 Talin and connections to actin

Figure. 1.2 shows a schematic representation of talin [7] and its various binding sites [7, 19]. Integrin binding sites are designated as "IBSi" and actin binding sites by "ABSi" [7, 19]. Actin binding initiates at $ABS3$ at the C-terminal [20] while integrin binds at $IBS1$. Extra binding sites known as cryptic actin-vinculin-talin (VBSs) exist within the folded domains $R1 - R3$, $R6 - R8$ and $R10 - R11$. Those VBS's are only exposed when corresponding domains are unfolded [1, 2, 7, 19, 21, 22]. We thus note that talin, an extended protein composed of multiple domains, undergoes reversible unfolding-refolding reactions [23]. As such it displays a strongly rate dependent force *vs.* extension response that is highly stochastic. Moreover, and most important, actin bindings sites are located as *cryptic binding* sites within the folded domains. This means that in order for talin to suppoprt progressively increasing forces, as a function of time, unfolding must occur to expose the required VBS's to bind talin to actin and thereby support the increasing force level. A general framework for describing unfolding is presented below and applied to literature data obtained for talin by way of calibration; this is but one of the stochastic features of the overall process.

It should be noted that, when domains unfold, talin is extended in length. If an imposed stretching rate is imposed on talin, for example, this will lead to load, *i.e.* force, drops as shown and discussed below.

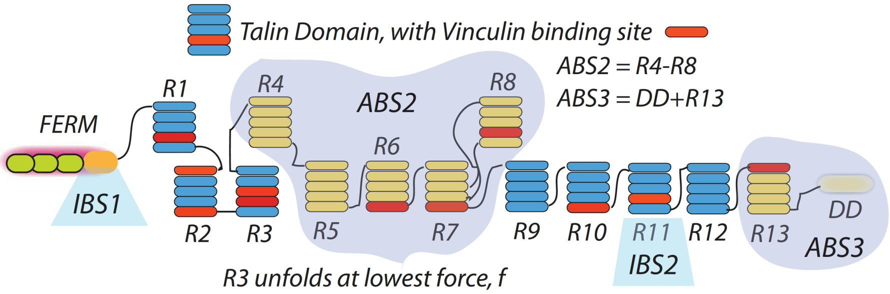

Figure 1.2. Model for a talin monomer. Note actin (ABS's), integrin (IBS's), and actin-vinculin-talin (VBS's) binding sites on talin. Note also the various domains $R1 - R13$ that may unfold and expose cryptic vinculin bonding sites that are indicated in various domains and are marked in red.

1.3.1 Transition state theory of protein unfolding-refolding

Using various sets of comprehensive experimental results of the force induced unfolding and refolding of single molecules of talin, a theoretical framework for unfoldings-refoldings originally developed for spectrin [23] has been calibrated. For example, considering the transitions between two states $f \leftrightarrows u$, folded (f) and unfolded (u), separated by energy barriers $\Delta E_{f\to u}$ and $\Delta E_{u\to f}$, the energy barriers can be expressed as, *e.g.* for unfolding

$$\begin{aligned} \Delta E_{f\to u} &\approx \Delta E^0_{f\to u} + \frac{\partial \Delta E_{f\to u} \partial f}{f} + \ldots \\ \Delta E_{f\to u} &\approx \Delta E^0_{f\to u} - f \Delta x_{f\to u} + \ldots \end{aligned} \tag{1.1}$$

Formally an activation length for unfolding may be defined as $\Delta x_{f\to u} \equiv -\partial \Delta E_{f\to u}/\partial f$. Using the usual transition state rate theoretical Arrhenius rate relation, and if the higher derivatives were neglected in the expansion above, we obtain for the unfolding rate

$$k_{f\to u} = \overrightarrow{k} k^0_{f\to u} \mathrm{e}^{f \Delta x_{f\to u}/kT}, \tag{1.2}$$

where $\overrightarrow{k}$ is a frequency term that is related to the attempt frequency of the $f\to u$ transition and $k^0_{f\to u}$ is the activation energy at zero F. Here k is Boltzmann's constant and T is the absolute temperature. Following a similar approach, the refolding rate can be described as

$$k_{u\to f} = \overleftarrow{k} k^0_{u\to f} \mathrm{e}^{f \Delta x_{u\to f}/kT}. \tag{1.3}$$

Now, if we let number of unfolded domains be N_u and total number of domains be N, $\phi_u = N_u/N$ as the fraction of unfolded, we would have balance rates at equilibrium for the reaction $f \leftrightarrows u$

$$(N - N_u)k_{f\to u} = N_u(k_{u\to f}). \tag{1.4}$$

This then leads to the relationship between projected end-to-end distance, x, and thus

$$\frac{x}{NL_f} = (1-\phi_u)\frac{x_f}{L_f} + \phi_u\frac{x_u}{L_u}\Big(\frac{L_u}{L_f}\Big), \tag{1.5}$$

with L_f and L_u being the contour lengths of the folded and unfolded domains, respectively and x_f and x_u being the projections extensions, in the direction of f of folded and unfolded domains, respectively; N is the total number of folded (N_f) plus unfolded (N_u) domains.

A freely jointed polymer chain model [24] was then used which leads to the relation

$$\frac{x}{NL_f} = (1-\phi_u)\mathcal{L}\Big(\frac{2fp_f}{kT}\Big) + \phi_u\mathcal{L}\Big(\frac{2fp_u}{kT}\Big)\Big(\frac{L_u}{L_f}\Big), \tag{1.6}$$

where $\mathcal{L}(\zeta) = \coth\zeta - 1/\zeta$, and p_i is the persistence length of an folded or unfolded domain, *i.e.* $i = f, u$.

Example force *vs.* time response are shown in Fig. 1.3 for the case where a fixed stretching rate, $\dot{x}$, is imposed. The two cases correspond to two different stiffness of the substrate to which talin is assumed to be bound. For perspective, it is noted that retrograde flow speeds are reported to be in the range of 1-600nm/s [25–29]; here we imposed a constant stretching rate of $\dot{x} = 100$nm/s. Variable stretching rate is to be discussed later in Chapter 2. One end of talin is assumed to be bound with actin in $ABS3$ and the other end is to be bound with integrin at $IBS1$.

Two cases are shown here, *viz.*, one where talin is connected to a compliant substrate with $k_s = 0.1$pN/nm and another to a stiff substrate stiffness with $k_s = 50$pN/nm. Substrates stiffness affects not only the magnitude of the force that develops but the time rate at which force develops. As experimentally reported and expected, $R3$ domains unfold

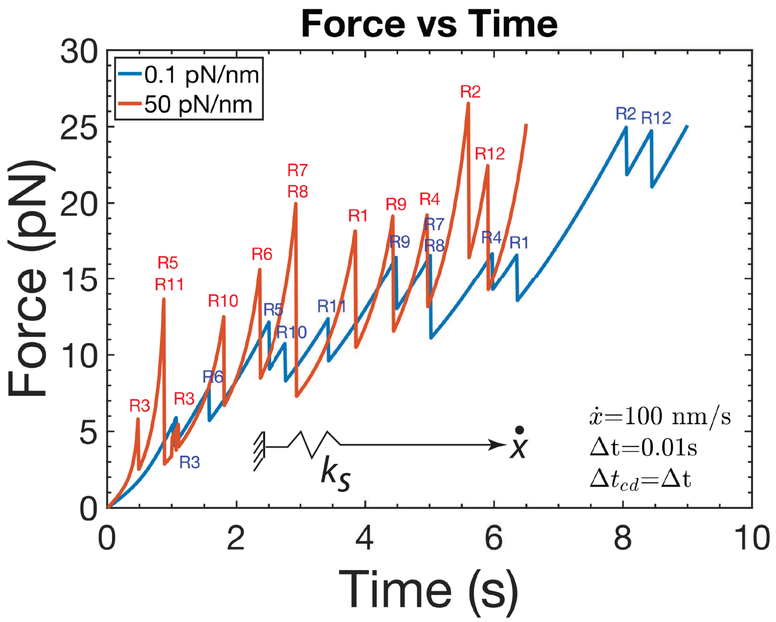

Figure 1.3. Force along talin rod *vs.* time at a stretching rate of $\dot{x} = 100\text{nms}^{-1}$. Unfolding events of talin domains are indicated at the associated force peaks.

first at lowest force levels [1, 2, 19]. The load drops mentioned above are clearly noticeable, and it is also seen that, although the onset of an unfolding event is a random process, the various domains tend to unfold at their own particular force levels; for example R3 tends to unfold at lower forces. Note also that R3 unfolds at shorter times with a stiff substrate; this sort of effect of substrate stiffness is important to ensure that sufficient reinforcement exists for talin-actin bonding to support the rising force levels; this is discussed in more detail in Chapter 2.

A comparison of predicted results and experimental results is shown in Fig. 1.4; note that in this case an imposed force *vs.* time was used. This sort of data is obtained by using atomic force microscopy (AFM) techniques to apply a rising force (or a stretching rate) to a single molecule of talin bound to a substrate. In this case unfolding leads to sudden extensions of talin length. The detailed numerical calibrations are discussed in Chapter 2, Appendix A. As discussed in Chapter 2, Appendix B, the appearance of these vinculin-actin binding sites then sets the stage for the attachment of the force-bearing talin within the force train.

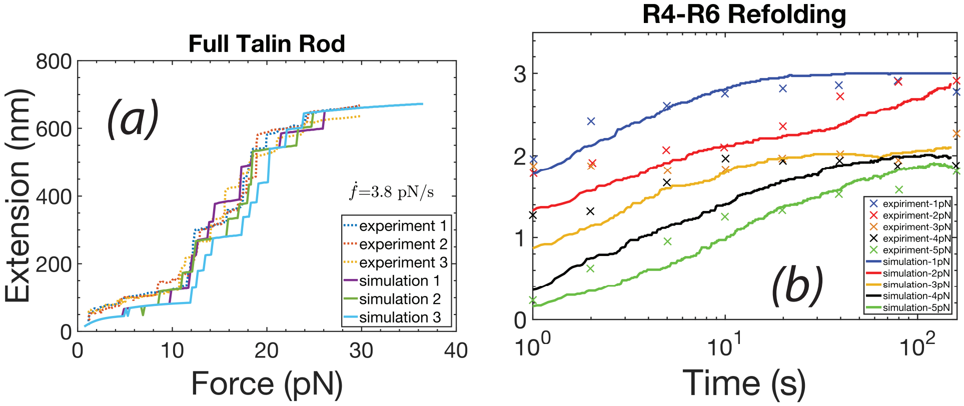

Figure 1.4. (a) Unfolding of a full talin rod compared to the experimental measurements of Yao *et al.* [1, 2]; unfolding as observed under imposed force rate. (b) Talin domain refolding.

1.4 Catch bonds

As the results from Fig. 1.3 assume that talin is bound with actin and integrins, the question arises if these bonds can indeed support the force *vs.* time response such as shown there. Note that the bonding dynamics itself, *e.g.* talin-integrin bond, is stochastic. Integrin bonds are of a type called *catch-bonds*. The *catch bond* is so-called because of its two-state nature in which the configurational nature of its "state 2", being in an extended and open nature, is able to support higher forces than when it is in its "state 1" that supports only lower forces.

In Fig. 1.5a, the energy landscape of the catch bond model is schematically sketched. Integrins have two minimal energy conformations separated by energy barriers. The two

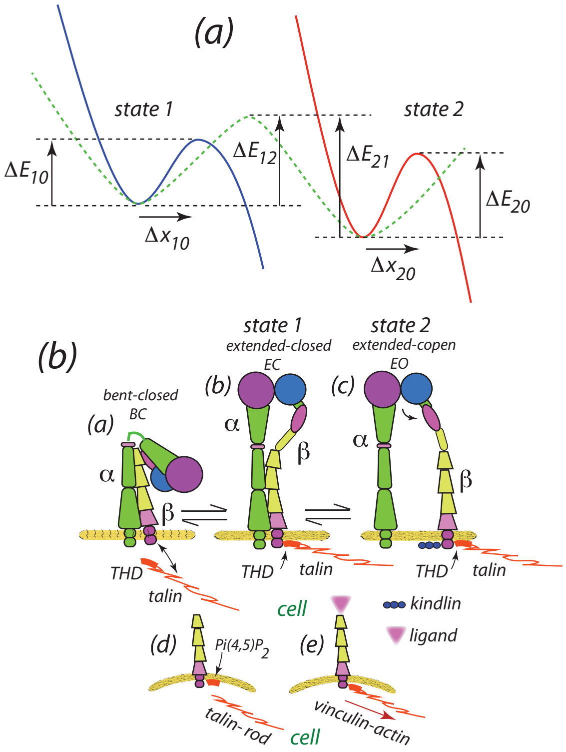

Figure 1.5. (a) Energy landscape of an catch-bond model and activation length. (b) Three conformation states of $\alpha_{III}b\beta_3$ integrins. Note the transitions between states $1 \leftrightarrows 2$ and those between $1 \leftrightarrows 0$ and $2 \leftrightarrows 0$, all of which are force dependent.

states correspond to two different conformation states of integrins as shown in Fig. 1.5b. The *activation distance* is Δx_{ij}, and ΔE_{ij} is the barrier height between states i and j. In its rest state, *i.e.* state 0, the *bent-closed* state, the molecule is inactive. Hence, the energy barrier from state 0 to state 1 is ΔE_{01} and from state 0 to state 2 is ΔE_{02}. The transition rate between state i and state j in the absence of force is k^0_{ij}, which is proportional to $e^{-\Delta E_{ij}/kT}$. When under the application of force, f, these energy barriers decrease by $f\Delta x_{ij}$, *i.e.* $\Delta E_{ij} = \Delta E^0_{ij} - f\Delta x_{ij}$, so the transition rate becomes

$$k_{ij} = k^0_{ij} \mathrm{e}^{f\Delta x_{ij}/kT}, \tag{1.7}$$

where $k^0_{ij} \propto e^{-\Delta E_{ij}/kT}$. The transition distances, Δx_{ij}, are formally defined as $\Delta x_{f\rightarrow u} \equiv -\partial \Delta E_{f\rightarrow u}/\partial f$ and are obtained by fitting to experimental data on single molecule bonds.

The activation distance may be thought of as the "distance" through which the force acts to achieve the critical state.

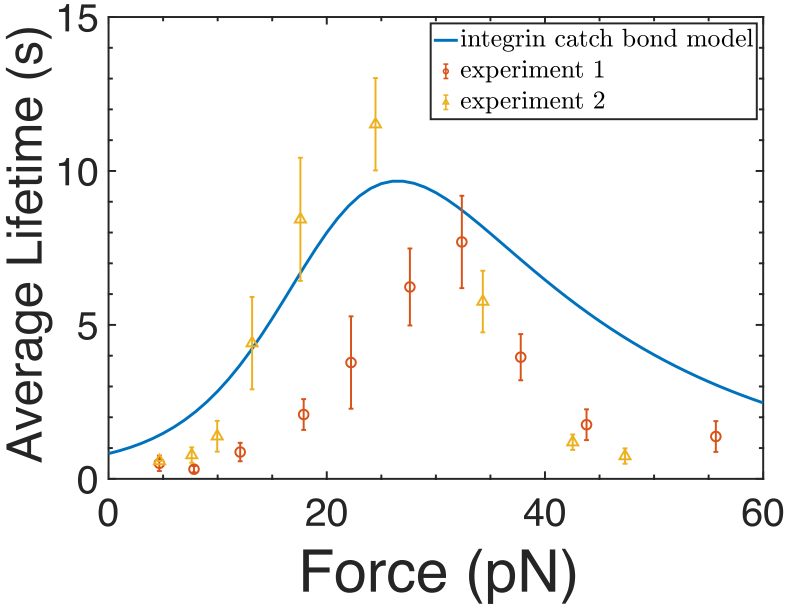

Figure 1.6. (a) Average bond survival time versus an assumed constant force for integrin bonds compared to the experimental measurements of Kong *et al.* [3].

We define $\mathcal{B}_1(t)$ and $\mathcal{B}_2(t)$ as the probability of occupancy of state 1 and state 2, respectively. These probabilities are described be a set of coupled ordinary differential equations are that are parameterized by the transition rates k_{ij} as, *e.g.*

$$\begin{aligned} \frac{d\mathcal{B}_1(t)}{dt} &= k_{21}\mathcal{B}_2(t) - (k_{10} + k_{12})\mathcal{B}_1(t) \\ \frac{d\mathcal{B}_2(t)}{dt} &= k_{12}\mathcal{B}_1(t) - (k_{20} + k_{21})\mathcal{B}_2(t). \end{aligned} \tag{1.8}$$

The probability of a bond surviving in either state is $\mathcal{B}(t) = \mathcal{B}_1(t) + \mathcal{B}_2(t)$. The expectation lifetime of a bond is computed as

$$\langle\tau\rangle = -\int_0^\infty t'(\mathrm{d}\mathcal{B}(t')/\mathrm{d}t')\mathrm{d}t' = \int_0^\infty \mathcal{B}(t')\mathrm{d}t'. \tag{1.9}$$

For integrin-ligand catch bonds, we have fitted the catch bond model as described by Thomas *et al.* [30] to the data of Kong *et al.* [3]. With that data used for calibration, we compute the average bond lifetime for integrin-fibronectin bonds at constant forces and compare it with experimental measurements of Kong *et al.* [3] as shown in Fig. 1.6.

1.5 Summary of points

Among the important points to take away from this brief discussion are, *inter alia*: 1) bonding itself is a stochastic event and is only described by its probability and rate of occurrence; 2) bond survival, *i.e* duration, is typically computed by the integration of coupled ordinary differential equations such as eqs. 1.8; 3) the various probabilities develop over time in a force-history dependent manner. Individual bonds, in fact, come and go during time. 4) The response of key structural elements such as talin is itself stochastic, such as the transitions between folded and unfolded states that mediates talin's strong rate dependence and non-linearity; and 5) the time and rate dependence of the response of nearly all key structural elements is also mediated by the cell's environment, *e.g.* the stiffness and topography of the extracellular matrix (ECM).

Chapter 2

Mechanosensitivity occurs along the adhesome's force train and affects traction stress

2.1 Introduction

Mechanical forces, *i.e.* stimuli, transmitted between the intracellular matrix and its environment, *e.g.* the extracellular matrix (ECM), determine a wide range of cell functions such as motility [31], proliferation [32], differentiation [33], as well as vital processes in cell development [34, 35], tumorgenesis [36, 37], cell growth [38–40] and wound healing [41, 42], *inter alia.* Cells perform these functions and are so regulated *via* the formation of focal adhesions (FA's) [43–46] that anchor the cell either transiently (*i.e.* dynamically) or permanently [47, 48] to, *e.g.* the ECM (the substrate). The focal adhesion complex is formed *via* the assembly of a number of proteins and has the important ability to sense (*via* its *mechanosensitivity*), and react to (*via mechanotransduction*), the nature of the environment, in particular its mechanical stiffness [33, 49–56] as well as surface topography [10, 57–60]. The effect of substrate stiffness, *per se*, has been exemplified by observations of cell migration on substrates with stiffness gradients [53, 54]. Precisely how this happens, however, has yet to be clearly delineated as the interactive, and coordinated, roles of all the various proteins involved have yet to be described in a holistic manner. Hence, no predictive theory or models for traction force development exists as yet. Accordingly, our goal is to provide more insight into the roles played by the various molecular participants in this performance with the aim of providing more background for creating such predictive capability. Our hypothesis was that mechanosensitivity is manifested at each of the key elements that play vital roles in the generation of adhesion force; although an intuitively pleasing concept, but yet not demonstrated, this is what we find and report herein.

The cell's adhesion complex and its protein components, the *adhesome* [9, 61], transmits force generated by retrograde flow of its intracellular actin cytoskeleton (*aka* hereafter "actin") *via* a series of proteins [7–9] that are bound to each other and ultimately to the cell's extracellular matrix. In our case we consider a *model adhesome* that includes the plague proteins talin and vinculin; hence our *force train* consists of actin(myosin)-vinculin-talin-integrin-ligand(ECM/substrate) [7, 8, 19] specifically suited for $\beta 1$ integrins. Although this is a small subset of the full adhesome [9], it accounts for a vital set of force bearing proteins as required for our analysis of traction force and stress; many other adhesome members play important roles in their activation and recruitment. The substrate possesses a clearly defined elastic stiffness and its cell interface has a certain density of receptors bound to ligands to which talin-integrin bonds. There has been considerable progress in delineating protein members of the adhesome and their individual properties and functionality - these are discussed below for our model adhesome as we present, and incorporate them into, a theoretical framework that follows the force pathway from actin-to-ECM. Our goal leads us to several pointed observations of how the system functions, or can function, and to some insights into how certain key correlations come about, such as the observed effects of substrate rigidity, and points specifically to what quantitative knowledge is missing and requires resolution in order that further understanding is possible. Our model system is minimal in that, although it includes major identified "players", at least those known to date, is yet deficient as not the entire cast of characters has been given sufficient quantitative definition; this theoretical recognition makes the specific contribution of crisply pointing to needed experimental inquiry. In summary, we find that mechano-sensitivity-transduction relies on the full array of molecular constituents, at least for optimal performance and cannot be attributed to any single set of model bonds often anonymously referred to as “clutch bonds”.

As it happens, mechanosensing actually begins at the anchorage of the force train *via* integrin-ligand bonds whose density and survivability depend on ECM stiffness, viscoelastic response, topology as well as molecular constituency; how all these factors actually accomplish this is far from clear in a mechanistic sense, yet legions of empirical observations exist that may, at least provide guidance for focused study. These are discussed herein. We begin, however, by providing a holistic, yet brief, conceptual overview of the adhesome considered here that provides a view of the various elements analyzed in our adhesome force-train.

2.1.1 Plan of the presentation

After a brief overview of key force-train elements, we describe a mechanism in Sec. 2.3 that we believe contributes to, and helps explain, features of integrin clustering as described, for example, by Cluzel *et al.* [62] and Changede *et al.* [63,64]. We then pass to a description of force development along talin rods in Sec. 2.4; this analysis assumes talin is bound to integrins and analyzes the stochastic talin-actin bonding and leads to a forecasted expected force *vs.* time response along talin dubbed $\langle f \rangle(t)$. In this we demonstrate a mechanosensing effect not previously described. Individual talin rods are envisioned to be part of ensembles. It is then necessary to probe the stochastic bonding of talin rods to integrins under the $\langle f \rangle(t)$ found in Sec. 2.4 to determine the population of talin rods actually engaged; this is done in Sec. 2.5. Without fidelity in the talin $\langle f \rangle(t)$ response the analysis of talin-integrin-ligand bonding would lack veracity. Net expectation forces and traction stresses are then estimated in Sec. 2.6 and discussion follows; the full dynamics of adhesion sites are not described herein, as that is left for future study.

2.2 Overview of the force-train's key elements

Indeed, it is reported that nascent adhesions involve the clustering of integrins even before they are clearly visualized [62–72] and before traction forces are generated and hence before mechanosensing occurs [63, 64, 70, 71]. The adhesome is then assembled at the nascent adhesion. Nascent adhesions may involve integrin densities of $\mathcal{O}(500-1000/\mu\text{m}^2)$; this may be a factor of at least 1.5 times the ambient integrin density [66] which indicates that clusters form. We realize, however, that other reports cite different numbers, yet this particular numerology appears appropriate for discussion sake. Integrins will be recruited into nascent adhesions as inactive integrins are converted to a talin bound, relatively immobile, specie. The resulting activity gradient of inactive integrins will lead to a diffusive influx. Once formed, diffusion within a mature clustered adhesion becomes occluded and slow [73] as integrins must diffuse through complex cytoskeleton corals [64, 74]. Thus integrins naturally cluster, and are under bonding forces, the adhesome is mobilized, and integrins are coraled within the adhesion. Just below, we describe interactions among integrins that are (modestly) affected by substrate stiffness (and possible time dependent response) that promote clustering.

Nascent adhesion clustering is depicted in Fig. 2.1a that outlines mechanisms and steps described by Cluzel *et al.* [62] and also consistently with [64, 75–77]. Here conformational changes in talin induced by PI(4,5)P_2 activates integrins that bind to essentially immobile ligands. Talin heads, and hence integrins, can associate with other talin-integrin-ligand groups as illustrated. In this Cluzel *et al.* [62] demonstrate a direct correlation between integrin activation and the formation of integrin clusters. They further discuss how "... actin fibers were dispensable for integrin clustering", but that "talin is the cytoskeletal protein first recruited to high-affinity $\beta3$ and $\beta1$ integrins and may play

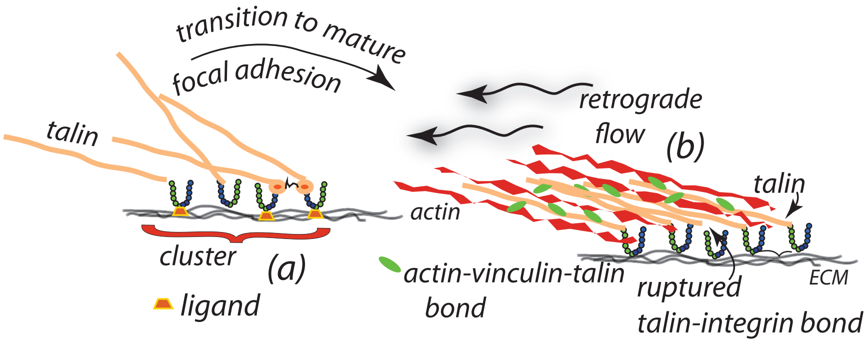

Figure 2.1. (a) Integrin-talin cluster within a nascent adhesion; note the co-clustering of unligated integrins. (b) Depiction of actin in retrograde flow tugging on talin rods bound to integrins that are bound to the ECM (substrate). Note the multiple connections between talin and actin filaments and the on-off bond rupture and reformation of integrins. Note also the depletion of inactive and unbound integrins that induces an influx of integrins into the adhesion.

a role in their clustering". We have incorporated these observations into our Fig. 2.1a. However, once focal adhesions are established and linked to actin-myosin force generation, additional clustering occurs as observed by Ballestram *et al.* [65]. Moreover, an additional driving force for clustering would be the elastic interactions described below.

We now recall that talin binds actin, initially we assume at binding sites dubbed $ABS3$ and later at $ABS2$ and then with vinculin bonds on unfolded $R3$ domains; this is described below in Section 2.4. Vinculin is activated, also *via* stimulation by PI(4,5)P$_2$ [62], and binds actin as assessed above. This is depicted in Fig. 2.1b. The net behavior of the adhesome's force train now depends on integrin bond lifetimes and, of course, on bound integrin density. Hence, the extent of clustering and all the cumulative effects of substrate stiffness are important for the magnitude of force generated and its temporal behavior. The adhesion can then grow by continued integrin influx. As it happens, substrate stiffness promotes this process as discussed below. We now provide more detailed descriptions of the force train elements; we begin, however, with additional comments on initial integrin clustering, *i.e.* nascent clusters.

2.3 Integrin clustering: contributing factors and pre-force

Here we consider contributing factors to initial integrin clustering that are part of determining integrin density and distribution. We establish certain important realizations, including the fact that bound integrins are under "pre-forces" that are not dependent on the forces generated within the force train *via* actin retrograde flow; that is pre-forces form in nascent adhesions. These pre-forces do, however, play a role in bond survival and hence in levels of force and thereby traction stresses that may develop. Indeed, pre-forces have been experimentally demonstrated to exist due, for example, to the need to compress the glycocalyx as indicated in Fig. 2.2; in cases of cancer cells this process may play mediating role [69, 78].

Mechanisms for integrin clustering have been discussed [63, 64]. However, clustering of integrins may be driven by, *inter alia*, the energetics of cell membrane deformation that is induced by the local bending deformations that are, in turn, caused by the force of the integrin bond [69]. This force comes about due to the fact that integrins must "stretch" to "catch-bond" to ligands [3, 79, 80] and induces local membrane and substrate bending as depicted in Fig. 2.2 showing a pair-wise integrin interaction. Here we present a quite simple mechanistic analysis of the pre-force that provides specific relations that allow for quantitative pre-force estimates and naturally reveals the origin of the interaction forces that promote integrin clustering. The dynamic picture we have presented, *i.e.* in Fig. 2.1b, involves talin-integrin bonding and de-bonding from their integrin-ligand attachments within the ECM. We now recognize that these bonds are under a *pre-force* and that they are catch bonds, hence we use catch bond theory [79] to describe their behavior using the data of Kong *et al.* [3] for integrin-ligand (*viz.* $\alpha5\beta1$ - fibronection) bonds as outlined in Appendix B. We compute the probability of bond survival under the actual expectation forces, $\langle f(t)\rangle$, generated along talin assuming they are bound to a ligated integrin. Our

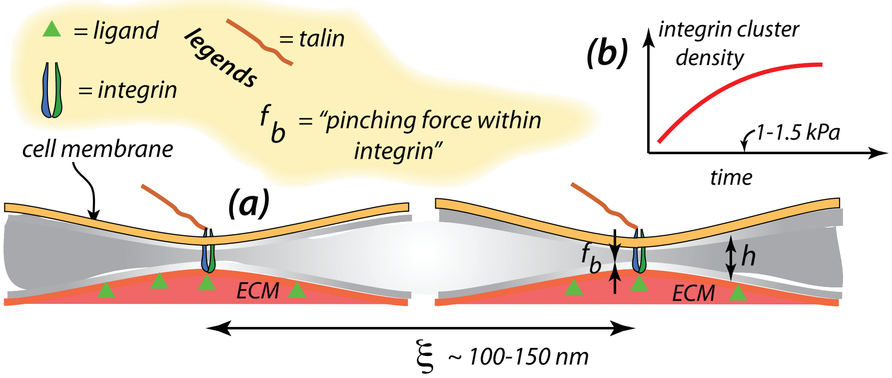

Figure 2.2. (a) Integrins bound to ligands generate an internal force f_b that induces local cell membrane and substrate bending. The interaction *via* the variation of free energy with translation of an integrin, *e.g.* an increase in ξ, the position integrin (1) specifies a force, f_{int}. (b) Expected integrin density *vs.* time as nascent clusters form.

goal is to assess the ability of a typical talin rod to sustain such forces and remain bound.

For a linear elastic system we may write for the free energy, $\mathcal{G}$, [81]

$$\begin{aligned}\mathcal{G} &= \int_V W(\mathbf{e})dV - \int_S Tu\mathrm{d}S \\ &= \frac{1}{2}\{f^{(1)}(\delta^{(1)}+u^{(2)}) + f^{(2)}(\delta^{(2)}+u^{(1)})\} - f^{(1)}(\delta^{(1)}+u^{(2)}) - f^{(2)}(\delta^{(2)}+u^{(1)}) \qquad (2.1) \\ &= -f\delta - fu^{(1)}, \text{ since here the symmetry of Fig. 2.2 suggests } f^{(1)} = f^{(2)} = f.\end{aligned}$$

In eqs. 2.1, $W(\mathbf{e}) = 1/2\sigma_{ij}e_{ij}$ is the strain energy density, T the vertical component of surface traction, $u(x)$ the net displacement field caused by $f^{(1)}$ and $f^{(2)}$ and $\delta^{(i)}$ is the normal displacement caused solely by $f^{(i)}$ at the site of integrin i. The symbols $u^{(1)}$, $u^{(2)}$ are the components of displacement normal to the plane of the substrate evaluated at the points of force $f^{(2)}$ and $f^{(1)}$, respectively; negative $u^{(1,2)}$'s point downward as do $f^{(1)}$ and $f^{(2)}$.

The variation in ξ represents a translation in the displacement field of $f^{(1)}$ and yields, with η being the position of integrin 2 with respect to integrin 1,

$$\delta\mathcal{G} \sim -f\{u(\eta) - \epsilon\frac{\partial u^{(1)}}{\partial x}|_\eta - u(\eta)\} = f^{(2)}\epsilon\frac{\partial u^{(1)}}{\partial x}|_\eta. \qquad (2.2)$$

Hence the result we seek for the interaction force, f_{int}, is simply

$$f_{\text{int}} = \frac{\partial \mathcal{G}}{\partial \xi} = -\frac{\delta \mathcal{G}}{\epsilon} = -f^{(2)} \frac{\partial u^{(1)}}{\partial x}|_{\eta}. \tag{2.3}$$

In the scenario of Fig. 2.2, since $f^{(2)} < 0$ and $(\partial u^{(1)}/\partial x)_{\eta} > 0$, we indeed have $f_{\text{int}} > 0$ which implies the point forces attract. The above analysis provides one mechanism for integrin clustering that we note is limited by several factors including, for example, steric interaction among integrins. What is needed now are specific model scenarios of Fig. 2.2 that allow calculation of the displacement fields and $\delta^{(i)}$ *vs.* $f^{(i)}$ relations; we consider two cases.

Case #1: To estimate magnitudes for this interaction we assume the integrins reside in a plate-like area of radius comparable to observed cluster sizes, say 100nm $\leq R \leq$ 150nm; there are 2 plates representing the cell and substrate with bending stiffness κ_c and κ_s, respectively. These dimensions reflect the reports of [63, 64] who observe nascent adhesions with dimensions corresponding to $R \approx 50 - 75$nm. Again, assuming linearity the relevant results are [82], with r being the radial distance from the point force,

$$\begin{aligned} u(r) &= \frac{f_b}{8\pi\kappa_i}\{1/2(R^2 - r^2) - r^2 \ln R/r\} \\ \partial u/\partial r &= -\frac{f_b}{8\pi\kappa_i} r \ln R/r, \text{ if } r \leq R \\ \delta_i = \frac{f_b R^2}{16\pi\kappa_i} = \frac{f_b}{k_i}, \text{ or } f_b &= \frac{16\pi\kappa_i}{R^2}\delta_i = k_i \delta_i, \, i = c, s. \end{aligned} \tag{2.4}$$

Now we require that a displacement $\delta^{\star} = \delta_c + \delta_s$ be imposed for integrin bonding and hence we have

$$f_b = \frac{\kappa_c \kappa_s}{\kappa_c + \kappa_s} \delta^{\star}. \tag{2.5}$$

For the cell membrane stiffness we take $\kappa_c = 10^{-19}$J. Hence if $R = 100$nm and $\delta^{\star} = 10$nm [5, 83, 84] we find $f_b \approx 3$pN if $\kappa_s \to \infty$. If, on the other hand the cell is bound to a supported lipid bilayer as used in [63, 64] we would have something more like $\kappa_s \sim \kappa_c$ and $f_b \sim 1.5$pN. Hence, there would appear to be a slight mechanosensing to this interaction, yet we emphasize that the effect exists regardless of substrate rigidity. This interaction would clearly promote integrin clustering, yet the effect would tend to dissipate once the reinforcing displacement fields of clustered integrins strongly overlap. Indeed we would realize that the force f_b within an isolated bound integrin would reduce when it's required displacement, $\delta^\star$, is partially provided by the displacement field of a nearby clustered integrin. This mechanism thereby supports a scenario of initial clustering of a number of integrins that saturates; the confinement of plaque protein corals would also tend to stabilize the cluster size; this again would be modestly sensitive to substrate stiffness as described in [62–64]. We note, in addition, that as talin is recruited in the activation of integrins, talin would also associate with unligated integrins. Hence, nascent clusters would contain both ligated and unligated integrins as noted earlier by [85–87] and more recently by [62–64].

The scenario of Fig. 2.2 is readily reinterpreted to suggest that integrin clustering will occur by the preferential activation and ligation of integrins to nearby ligated integrins. Clustering is then not only a natural result but the effect would be self limiting since once a number of integrins so cluster, with each contributing to the required displacement, the cluster would look like a single integrin to the far field of other integrins. Hence, these nascent clusters will form to limiting sizes.

Case #2: We also note that grey regions shown in Fig. 2.2 may indeed represent the cells glycocalyx. Analysis of this would not alter the essential points made here, but now the cell membrane and substrate would be modeled as plates deflecting on a *deformable foundation*. Glycocalyx properties in this context are, however, far from well established, but we refer to O'Callaghan *et al.* [88] and our own theoretical model [89] that accounts for electrostatic repulsion. For standoff distances of say 10nm $\le h \le$ 15nm, reasonable estimates of *apparent stiffness* would be 0.2kPa $\le E_g \le$ 1kPa. Force *vs.* deflection relations would now look like

$$\delta^{(i)} = f_b \frac{\alpha^{(i)}}{3\sqrt{3}E_g^\star}, \; \alpha = \sqrt[3]{\frac{E_g^\star}{\kappa^{(i)}}}, \kappa^{(i)} > 0, \tag{2.6}$$

with $E_g^\star = 1/2E_g/(1-\nu^2)$. As values, or even a precise definition, of Poisson's ratio ν are unavailable we take $\nu = 1/4$ and this leads to $1pN \leq f_b \leq 3pN$. The effect of variable properties such as ν is deemed to be quite small as for most biological materials of this type Poisson's ratio is typically taken in the range $0.3 \leq \nu \leq 0.5$ [90]. We note that in this case the effect of substrate stiffness is reduced somewhat and a larger influence is made by the glycocalyx properties that are, unfortunately, not accurately known.

An effect that arises from integrin pre-forces, especially when the discussion surrounding Fig. 2.2 is recalled; this concerns the type of initial condition used to assess integrin catch bond survivability as outlined in Appendix B. Given that talin-integrin complexes exist, perhaps under pre-stress such as with stiffer substrates, that are then linked to actin-myosin contractility, we expect that the initial conditions are more appropriately of types $II - II'$ as in Appendix B; types $II - II'$ assume an equilibrium between states 1 and 2. In contrast, on compliant substrates we expect initial conditions are more like those described as types $I - II$. This apparently has not been previously considered.

We pass now to the description of talin's force *vs.* time response.

2.4 Force response of talin and its connections to actin

Fig. 2.3a illustrates a schematic representation of talin [7] and its various binding sites [7, 19]. Integrin binding sites are designated as "IBSi" and actin binding sites by "ABSi" [7,19]. Talin has two integrin binding sites, $IBS1$ and $IBS2$ and can dimerise as we shall consider below in Fig. 2.4. Actin binding sites begin at $ABS3$ at the C-terminal [20]; additional actin binding sites are described as cryptic actin-vinculin-talin (VBS's) and are buried within the folded domains $R1 - R3$, $R6 - R8$ and $R10 - R11$. They are exposed upon the progressive force-unfolding of ABS containing domains [1,2,7,19,21,22]. We note that detailed and elegant experiments have been carried out that document the force-induced unfolding and refolding of talin; we have quantitatively described their data with our theoretical unfolding/refolding model [23] originally developed for spectrin. In Fig. 2.3a the cryptic vinculin binding sites on the talin rod are specifically listed [1,2,7,19,22].

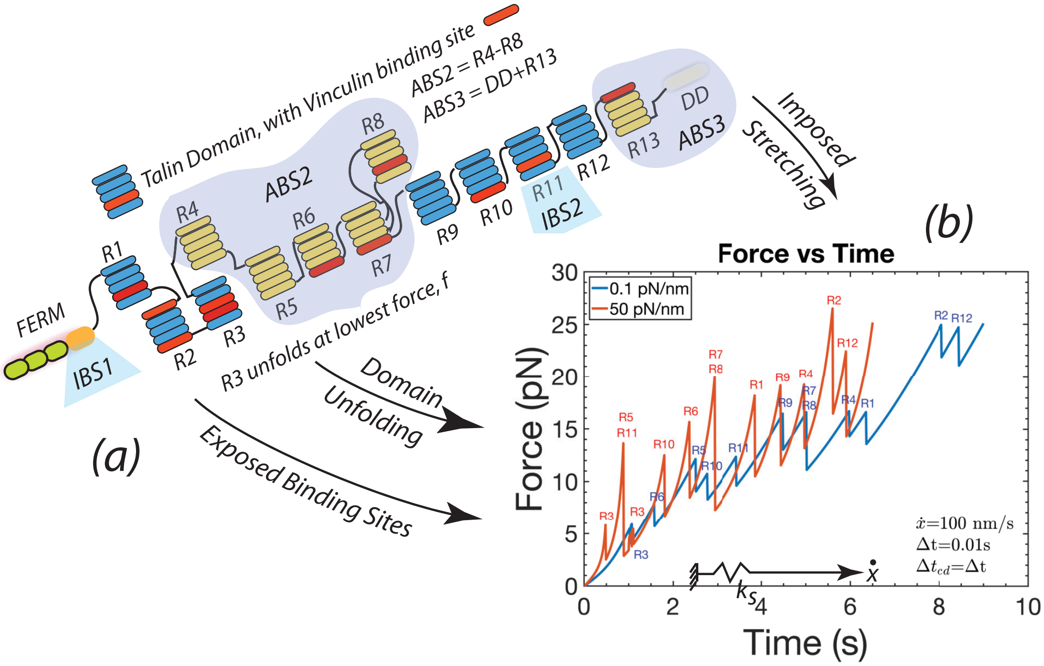

Figure 2.3. (a) Model for a talin monomer. Note actin (ABS's), integrin (IBS's), and actin-vinculin-talin (VBS's) binding sites on talin. VBS's are shown in red in various domains. (b) Force along talin rod *vs.* time at a stretching rate of $\dot{x} = 100\text{nms}^{-1}$. Unfolding events of talin domains are indicated at the associated force peaks.

The calibration of the unfolding model is described in Appendix A and in Fig. 2.3b we show a typical talin force *vs.* time response to the stretching of a full talin rod at a constant rate of $\dot{x} = 100$nm/s; the response at lower rates is considered later. Clearly we assume here that talin is bound at both its ends, presumably to $ABS3$ (actin) and to integrin-substrate at $IBS1$; these prospects are analyzed later. Rearward actin speeds have been reported for various cell types and, depending on location within the cell, are in the range 1-600nm/s [25–29]; here we use fixed rates of order 100nm/s and later variable rates between 40-100nm/s.

In Fig. 2.3b the substrate stiffness is taken as $k_s = 0.1$pN/nm or $k_s = 50$pN/nm; these roughly correspond to elastic moduli of $E \sim 0.4$kPa or ~ 40kPa, respectively as discussed in Appendix A. As expected, and as already observed, it is common for $R3$ to unfold early, *i.e.* at the lowest force levels [1, 2, 19]. The *unfolding forces* (*i.e.* the peak force at unfolding) are modestly dependent on loading rate since the activation lengths for unfolding are generally large (see Appendix A). Note, however, the example of unfolding of $R4$, shown in Fig. 2.3b, that unfolds at a distinctly lower force when talin is stretched against a compliant substrate. Subsequently, we observe unfolding at domains within $ABS2$ (*i.e.* $R4 - R8$) and $R11$ (which is also an integrin binding domain). Other noteworthy features of the unfolding process include the fact that the load drops upon unfolding are larger with a stiffer substrate and consequently that the *unfolded forces* (*i.e.* the forces after unfolding) can be larger on a compliant substrate. Also it is noticed that refolding, at low forces, can and does occur (follow $R3$ at low forces), as long as an unfolded talin domain contains no vinculin bond as discussed below.

At first glance it may appear that the "general talin force *vs.* time" is higher with a stiffer substrate and yet the effect is seen to be modest, due to the strong force buffering effect of the unfolding of talin, and would not seem to explain the generally larger traction forces generated on stiffer substrates. We note that although refolding is observed at low forces, *viz.* less than $\sim 3 - 5$pN, refolding is not expected at higher forces (see Appendix A and [1, 2]).

Moreover, the responses shown in Fig. 2.3b assume that the talin rod is indeed bound, say to actin as well as to integrin-ligand-substrate. Hence there is the question of whether these bonds can support the force *vs.* time response of Fig. 2.3b. Accordingly, we next explore this possibility but now assuming only a talin-integrin connection. We specifically explore the talin-actin and talin-vinculin-actin bonding dynamics.

We take the talin-actin bonds to involve at least three distinct contributions.

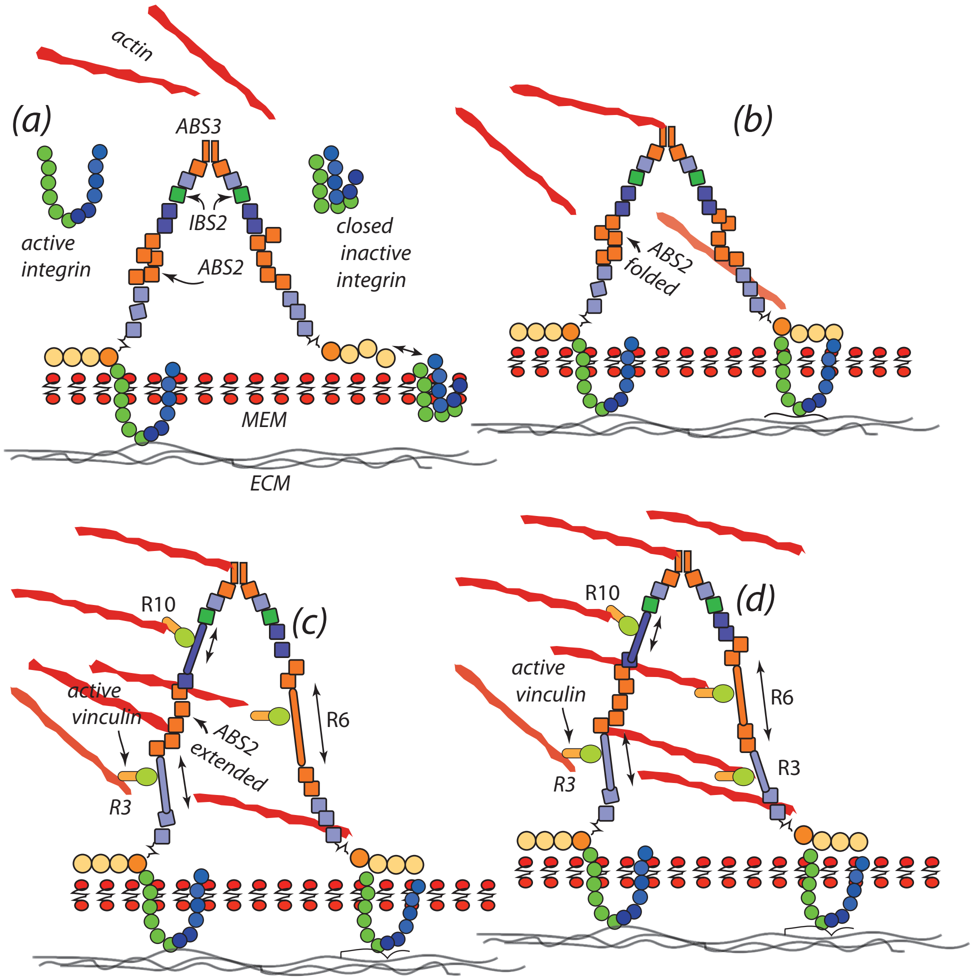

Figure 2.4. A talin dimer shown at various stages of unfolding and bonding, *via* vinculin, to actin.

Following Gingras *et al.* [20] and others [7, 19, 91], we assume an initial connection of talin to actin at $ABS3$; this initiates force on actin. However we do not expect this bond to survive for forces greater than, say 3-5 pN, or for times greater than say 2-3 s. Hence the activation of [19,92], and then the unfolding of, $R3$ is vital as it activates $ABS2$ [7,19,91] and then presents an erstwhile cryptic vinculin bond to talin and then to actin.

Vinculin-actin bonds have been quantified in the elegant experimental and analytical work of Huang *et al.* [6]; in this they document the behavior of vinculin-actin *catch bonds* and provide data that may be used to calibrate the catch bond model as developed by Thomas *et al.* [79]. We have thus calibrated the Thomas model [79] as described in Appendix B. By invoking such an actin-vinculin-talin catch bond, the talin rod is thereby reinforced against the prospect of a failing ABS3-actin initial bond. Moreover, the unfolding of R3 serves to activate ABS2 by allowing its conformational change (global domain, not helix, unfolding) to provide additional talin-actin reinforcement. Hence we now present Fig. 2.4 that depicts a probable sequence of binding patterns.

Figure 2.4 shows our talin dimer scheme patterned after a scenario suggested by Klapholz and Brown [7]. We begin with an integrin bond at the IBS1 of one monomer as in Fig. 2.4a (left side) followed by an ABS3-actin bond as in Fig. 2.4b. This engages and loads the talin rod [7,19]. As force grows and $R3$ unfolds we compute the probability of a vinculin bond from actin-$R3$-talin. We then continue stretching and compute the probability of bond rupture from catch bond theory. The unfolding of $R3$ activates $ABS2$ as shown in Fig. 2.4c; this engages another link to actin. We may assume that the dimer forms another talin-integrin-ligand bond and the process proceeds stochastically on the other monomer as in Fig. 2.4d.

Now catch bonds are “two state” bonds with state 1 stable at lower forces and state 2 at higher forces [30,79,93–96]. We note that, although unfolding forces tend to be higher on stiffer substrates, the unfolded forces are comparable on both compliant and stiffer substrates. This means that if we assume the bonds that form on a newly unfolded talin domain form in equilibrium with the prevailing force they are likely to form in the same state on either stiff or compliant substrates - but what are their survival prospects

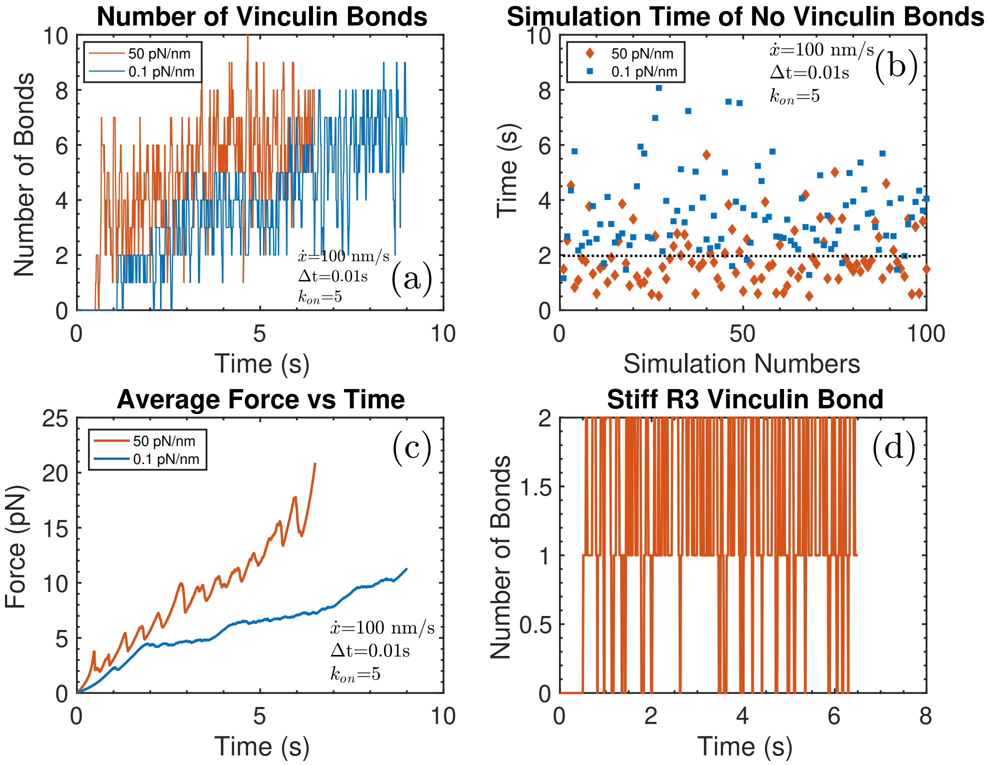

Figure 2.5. (a) Evolution of the number of actin-vinculin-talin bonds following talin unfolding. (b) Results for the time beyond which persistent actin-vinculin-talin bonds exist, t_{p}, following 100 simulations. The dashed line drawn at 2s is used for discussion purposes in the text. (c) The computed average forces *vs.* time, $\langle f \rangle$, taken over a large number of simulations such as in Fig. 2.3b but assigning a null result for those that would be judged not to survive, where $t_{\mathrm{p}} \geq 2$s. Note that $\langle f \rangle$ *vs.* time is seen to continuously rise here due to the fact that talin-vinculin-actin bonds survive for the limited time period shown; eventually they will fail, but only after the time periods shown. (d) The number of bonds formed on $R3$ and that failed, N_f, in a particular simulation with a stiff substrate.

and how does substrate stiffness affect their survival?

We first describe the kinetics of actin-vinculin-talin bond formation. Following Huang *et al.* [6], we take the probability of vinculin bonding to actin to be of the form [97]

$$\mathcal{P}(t) = 1 - e^{-k_{\mathrm{on}}^{v} t}, \tag{2.7}$$

with $k_{\mathrm{on}}^{v} \sim 4 - 5\mathrm{s}^{-1}$ and where t is measured from the time of unfolding or the time that an erstwhile vinculin bond failed, the latter referring to rebinding. Although empirically calibrated by Huang *et al.* [6] for vinculin-actin bonding, the form of eq. 2.7 follows from the more general analysis of Litinov *et al.* [97].

We note in passing that as long as a vinculin bond exists on an unfolded talin domain, no refolding is allowed [1,2]. Once a bond is formed the probabilities of transitions between states $1 \leftrightarrows 2$ are computed as well as for the failures of either state; ultimately the probability $\mathcal{B}(t)$ of a bond of either state is computed (see Appendix B). In this we assume that the full force is supported by all vinculin bonds equally, *i.e.* in parallel. In a simulation, we then poll each bond for failure. Some results are shown in Fig. 2.5a where we show the vinculin bonds that come and go only at exposed VBS's on the unfolded talin rod; to be sure, the actin-talin bonds at $ABS3$ and $ABS2$ without unfolding are not included in the bond count of Fig. 2.5a. We recall that this process is stochastic and hence the result of Fig. 2.5a must be seen as one of many random processes. However, to gain some insight we focus on the result with the stiffer substrate and note that we may suppose that the jump to 2 bonds just after $t \approx 0.5$s is the result of 2 bonds forming on the 2 VBS's on the unfolded $R3$ talin domain. Yet we then observe that these bonds fail thereafter at about $t \approx 1$s; in the interval $0.5\text{s} \leq t \leq 1\text{s}$ we have bond failure and reforming events. At about $t \gtrsim 1$s we have 3 bonds due to the unfolding of $R11$ with one VBS ($R5$ which unfolds at this time has no VBS); yet we observe that at a short time after all 3 bonds have failed. Thereafter we form more bonds that persist for the duration of the simulation. Similar observations can be made regarding the more compliant substrate, but with rather significant differences. Firstly, the number of persistent bonds *vs.* time and the time to establish persistent bonds, t_{p}, are larger with a stiffer substrate. For this particular simulation $t_{\text{p}}(\text{stiff}) \approx 1$s and $t_{\text{p}}(\text{compliant}) \approx 1.5$s. To explore this further we performed large numbers of such simulations (100-2000); for clarity we show the results for t_{p} following 100 such simulations in Fig 2.5b. Such large numbers of simulations are required for obtaining expectation, or average, force *vs.* time response as shown next.

It is indeed noteworthy that we observe distinctly higher values for t_{p} on more compliant substrates. The line drawn in Fig. 2.5b at $t_{\mathrm{p}} = 2$s suggests that, since the initial bonds supporting talin are unlikely to survive for times $t \gtrsim 2$s, a large fraction of talin rods would likely fail. To visualize this we compute the force *vs.* time responses shown in Fig. 2.5c. In Fig. 2.5c we display the average force, $\langle f \rangle$, a large group (> 100) of talin rods would support *vs.* time assuming that only those with $t_{\mathrm{p}} \geq 2$s survive. Hence if, say the original number of talin rods was $\mathcal{N}_t$, then the total force they collectively exert would be $\mathcal{F} = \mathcal{N}_t \langle f \rangle$. In this manner we demonstrate that increased substrate stiffness causes an increased net force.

We note, in passing, that these results demonstrate that without talin unfolding essentially no talin rods would survive longer than, say, 3 seconds and hence quite low or no sensible forces would be developed.

The rationale for making the above assumption is based on the dynamics of actin-talin or actin-vinculin-talin bonds such as exemplified in Fig. 2.5d; this shows the on-off dynamics of actin-vinculin-talin bonds on the unfolding $R3$ domain during the simulation of Fig. 2.3 calibrated as a catch bond using the data of Huang *et al.* [6]. We cannot, at present, confirm the veracity of this correlation but we believe that it is representative enough to establish basic trends of the effect. Errors in time intervals on the order of say $\delta t \sim 0.1 - 0.2$s would be considered quite large and yet would not affect our argument in any measurable way.

Our simulations of the behavior of talin bound to actin and presumably bound to an anchoring integrin have shown a substantial effect of substrate stiffness in terms of talin's ability to transmit force. In particular, the forces are observed to grow faster with stiffer substrates. We note that, due to the strong force buffering effect of talin's unfolding, this effect is not a trivial outcome of talin "pulling on a stiffer spring"; to appreciate this simply observe the comparable force levels in Fig. 2.3b for both stiff and compliant substrates.

We now must complete this force train by specifically considering the effects of the vital link to the integrin-substrate connection - this is another catch bond.

2.5 Net forces generated on the force train

In analyzing the response of talin we had assumed that talin was bound to an integrin-substrate complex. This assumption led to the expected force *vs.* time of Fig. 2.5c. Indeed, it is believed that nascent adhesions involve the clustering of integrins even before they are clearly visualized [62, 65–69]. The adhesome is then assembled at the nascent adhesion. We now must consider the expected survival of such catch bonds. These catch bonds are calibrated in Appendix B using data from Kong *et al.* [3].

Figure 2.10a and Figs. 2.10c,d show three scenario's for catch bond behavior, each for a stiff and compliant substrate. The scenario's are characterized *via* the initial conditions taken for the initial bond types, *i.e.* bond states 1 or 2, that are called conditions I, II, or II′ in Appendix B. We note the above discussion regarding the time dependent recruitment of integrins to the adhesion site and their association with talin and they are under a pre-force suggests that initial conditions II or II' are more appropriate; this condition was also used by Huang *et al.* [6]. The significant differences between the cases using either initial conditions II or II′ and initial condition I are clear from the probability *vs.* time plots. In Fig. 2.6a we explore this further and show the probability $\mathcal{B}(t) = \mathcal{B}_1(t) + \mathcal{B}_2(t)$ *vs.* time for a range of integrin pre-force.

We recall that the average bond lifetime, $\langle\tau\rangle$ is computed from the integral in eq. 2.24 of Appendix B. For that purpose we use the *bond rupture function*, $-\mathrm{d}\mathcal{B}/\mathrm{d}t$, to describe the probability of a bond failing at time t. Note, that from eq. 2.23 we find, indeed, that

$$-\frac{d\mathcal{B}}{dt} = k_{10}\mathcal{B}_1(t) + k_{20}\mathcal{B}_2(t), \tag{2.8}$$

is the probable rate of bond rupture at time t. However, to compute the expected force

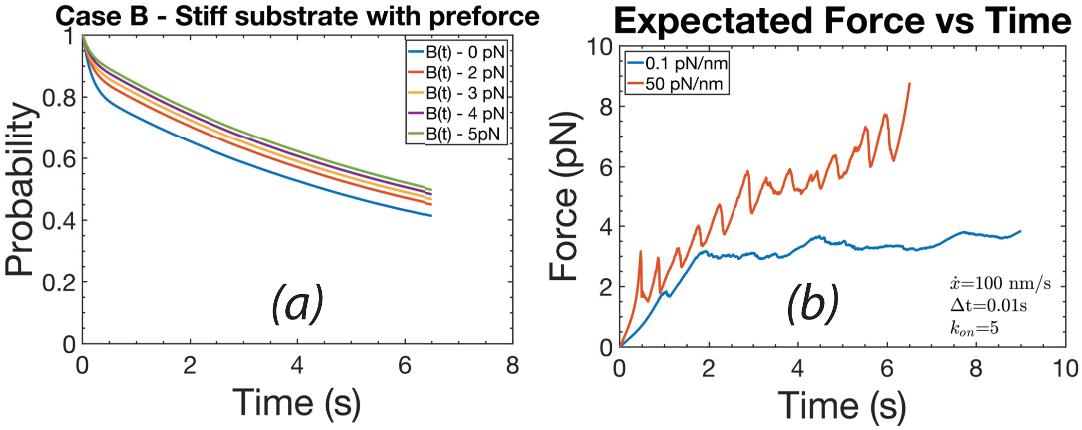

Figure 2.6. (a) Probability $\mathcal{B}(t) = \mathcal{B}_1(t) + \mathcal{B}_2(t)$ *vs.* t using type II and II' initial conditions; pre-forces are indicated. (b) Expectation force *vs.* time with various integrin pre-forces. Note that force *vs.* t for a compliant substrate is also indicated, with type II initial conditions.

surviving along a talin rod we want the bond *survival function*, *viz.* $\mathcal{B}(t)$. Hence we arrive at

$$\langle f \rangle(t) = f(t)\mathcal{B}(t), \text{ with } \lim_{t\to\infty} \langle f \rangle(t) \to 0. \tag{2.9}$$

Clearly, $\langle f \rangle(t)$ vanishes at $t \to \infty$. This is shown, along with $\mathcal{B}(t)$, in Figs. 2.6b and 2.6a, respectively for the case of a fixed $\dot{x} = 100\text{nm/s}$.

2.5.1 Variable actin retrograde flow speed

To account for the effect of the "back force" the force train exerts on the actin myosin-motor system, we impose a force dependent stretching speed as given by the phenomenological form used by Chan and Odde [98] and also by Elosegui-Artola *et al.* [4, 99] and Huang *et al.* [6], *viz.* we set $\dot{x}$ to the form

$$\dot{x}(t) = \dot{x}_0 \left[1 - \left(\frac{\langle f \rangle}{f_{\max}} \right)^n \right], \tag{2.10}$$

where $f_{\max}$ may lie in the range $8\text{pN} \le f_{\max} \le 30\text{pN}$. In what follows, we take $\dot{x}_0 = 100\text{nm/s}$ and $n = 1$. We proceed to compute expectation forces as described above for constant

$\dot{x}$. Two most useful results are shown in Figs. 2.7a,b, for the case of a modest reduction in stretching speed obtained with $f_{\max} = 30$pN. In this case we demonstrate that even a modest forecasted reduction in $\dot{x}$ leads to an noticeably increased difference in expected force *vs.* time between stiff and compliant substrates as shown in Fig. 2.7a. Figures 2.7a,b should be compared to Fig. 2.5b for the times beyond which persistent actin-vinculin-talin bonds exist. As an example, the difference in the forecasted $\langle f \rangle$ at $t = 5$s between the stiff and compliant substrate is approximately a factor of 2 with a fixed speed, but nearly a factor of 8 with the modestly variable speed we imposed. Part of the reason for this can be appreciated by examining and comparing to Fig. 2.5b which indicate a nearly 1s increase in the time beyond which persistent actin-vinculin-talin bonds exist. This is actually a significant difference that accounts for the reduced number of active actin-vinculin-talin members in the net force train. This difference is also reflected in the "plateau-like" behavior of $\langle f \rangle$ *vs.* time in Fig. 2.7a. Simply put, as the force rises less rapidly with decreasing retrograde speed, there is more time for bond failure. We note in passing that,

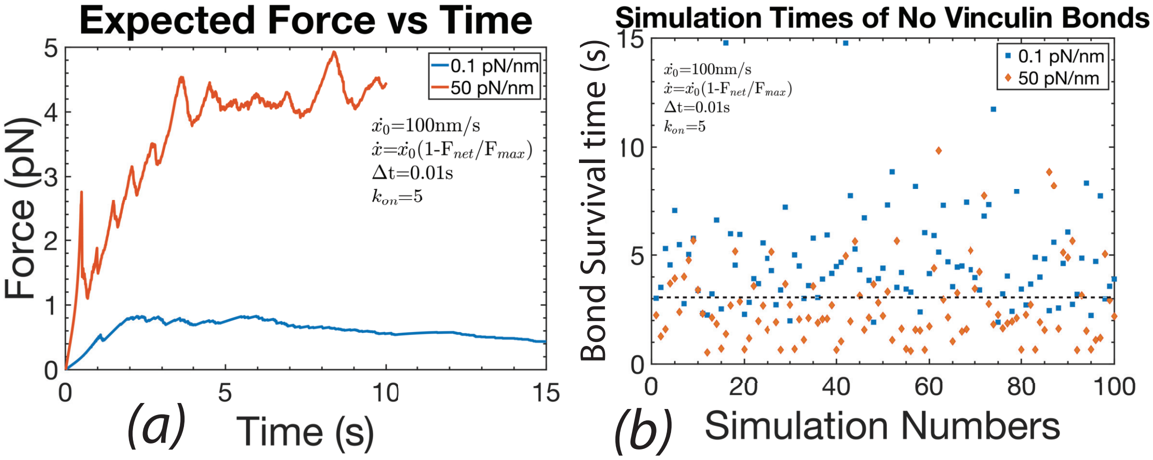

Figure 2.7. (a) Expectation force *vs.* time with an integrin pre-force of 3pN. Note, as in Fig. 2.5c, that $\langle f \rangle$ *vs.* time is seen to continuously rise here due to the fact that talin-vinculin-actin bonds survive for the limited time period shown; eventually they will fail, but only after the time periods shown. (b) Results for the time beyond which persistent actin-vinculin-talin bonds exist, t_{p}, following 100 simulations. The dashed line drawn at 3s is used for discussion purposes in the text.

in principle, forces on talin would eventually fall to zero, or saturate. Reasons for this include the understanding that conformational changes in talin under sufficiently large forces remove vinculin bonding sites (see *e.g.* [1, 2]). The relevant force ranges we consider do not reach such levels.

2.6 Net traction stress and assessments

As noted above, we expect the net traction stress, $\mathcal{T}(t)$, to be determined by $\mathcal{N}(t)$, the dynamic number of bound talin-integrins (per unit area) and the expectation force, $\langle f\rangle(t)$ as, for example

$$\mathcal{T}(t) = \mathcal{N}(t)\,\langle f\rangle(t). \tag{2.11}$$

$\mathcal{T}(t)$ may, indeed, be dynamic and display various forms of temporal and/or spatial patterns of turnover. We have discussed factors that clearly suggest that stiffer resistance to force, say arising from stiffer substrates, tend to enhance $\mathcal{N}(t)$ and, of course $\langle f\rangle(t)$. If, for instance, $\mathcal{N} \sim \mathcal{O}(400 - 600\mu\text{m}^{-2})$ we would forecast $\mathcal{T} \sim \mathcal{O}(2 - 3\text{kPa})$ providing talin rods are expected to survive $\sim 10s$.

To compare the above forecasts with other modeling efforts we observe the following. To essentially reproduce the results of Elosegui-Artola *et al.* [4, 99] we would assign to $\mathcal{N}$ a bonded integrin density patterned after their reported measured densities that display a rather sharp rise at a critical substrate stiffness; this would suffice to explain the observed traction *vs.* substrate stiffness. Elosegui-Artola *et al.* [4, 99] used this empirically observed behavior to accurately "fit" their data.

The "clutch bond" model of Chan and Odde [98] is more difficult to fit within the present framework. The model does essentially provide a picture for increasing traction stresses with increasing "substrate stiffness"; this is due the increasing forcing rate with actin retrograde flow. The force train is, however, not described except to connect it to a parallel array of "clutch bonds"of unspecified character.

Still other recent models are discussed in Section 2.7.3 in relation to the analysis presented herein.

2.6.1 Steady state traction stresses

We conclude this section with estimating steady state traction stress magnitudes in a stable FA complex. As noted above, integrins, once activated, bind talin and tend to cluster as depicted in Fig. 2.1. Clustering may depend on substrate stiffness as discussed by *e.g.* [4,99] but to date no explanation of this exists; we first estimate this *via* a particular integrin interaction mechanism. Next we use this to estimate expected traction stresses.

Initial estimates of the *mean expectation steady state traction stresses*

The expected force *vs.* time curves along a given actin-vinculin-talin-integrin connection, shown in Fig. 2.6b and 2.7a, provide forecasted forces that would be expected along the force train as a function of the time that they may be active, *i.e.* actually connected all along the force train. However, these connections undergo continuous stochastic turnover - that is, they come and they go! To assess this we assume that, at steady state, their numbers remain stationary in that they last their average lifetimes, $\langle \tau \rangle$, as given by eq. 2.24; these average lifetimes are listed for various cases in Table 2.1.

Table 2.1. Integrin bond expected lifetimes as computed from eq. 2.24 using the force *vs.* time responses for the cases of Figs. 2.6a,b and 2.7a. Recall, for these cases the fixed stretching rate was $\dot{x} = 100\text{nm/s}$ and for the variable, force dependent, rate $\dot{x}_0 = 100\text{nm/s}$ with $\dot{x}(t)$ given by eq. 2.10 with $f_{\max} = 30\text{pN}$.

Substrate	Stretching rate (nm/s)	$\langle \tau \rangle$ (s)
compliant	$\dot{x}$ fixed	4.67
stiff II	$\dot{x}$ fixed	3.84
stiff II'	$\dot{x}$ fixed	4.26
compliant	$\dot{x}$ variable	5.85
stiff II	$\dot{x}$ variable	5.01
stiff II'	$\dot{x}$ variable	5.60

Now, as these connections continuously turnover, and if we assume this occurs in a regular smooth pattern, the average force they contribute to an ensemble of such connections is $\langle f\rangle(t=1/2\langle\tau\rangle)$. We use the case of variable stretching rate and thus we extract expected forces from Fig. 2.7a. This leads to the following values, *viz.*

$$\langle f\rangle(t=1/2\langle\tau\rangle)=\begin{cases}0.6\text{pN compliant substrate}\\ \\ 3.1\text{pN stiff substrate, II'.}\end{cases} \tag{2.12}$$

We use the measured integrin densities reported by Elosegui-Artola *et al.* [4,99] of $d_{\text{int}}=500\mu\text{m}^{-2}$ as may exist on compliant substrates and $d_{\text{int}}=1000\mu\text{m}^{-2}$ as may exist on stiffer substrates due to the clustering tendencies we described above. This, however, does not yet fully specify $\mathcal{N}$ of eq. 2.11; for our steady state scenario, we may call this $\mathcal{N}_{\text{ss}}$.

To estimate $\mathcal{N}_{\text{ss}}$ we require the probability, $\mathcal{P}_{\text{b}}$, of integrin binding to substrate ligands, and recalling they are catch bonds, in either states 1 or 2. We use the experimental results and accompanying kinetic analysis of Litvinov *et al.* [97] for αIIbβ3-fibrinogen bonds enhanced with Mn^{++}. In this they [97] find, with time scales that exceed say 0.5s, $\mathcal{P}_{\text{b}}\to 0.175$ approximately. As this is within our time scales of, say $\langle\tau\rangle$ we use this as an appropriate estimate and thereby obtain

$$\mathcal{N}_{\text{ss}}=d_{\text{int}}\mathcal{P}_{\text{b}}=\begin{cases}88\mu\text{m}^{-2}\text{ compliant substrate}\\ \\ 176\mu\text{m}^{-2}\text{ stiff substrate, II'.}\end{cases} \tag{2.13}$$

In this manner we arrive at the following estimates for the expectation steady state traction stresses, *viz.*

$$\langle \mathcal{T}_{\text{ss}} \rangle = \mathcal{N}_{\text{ss}} \times \langle f \rangle (t = 1/2\langle \tau \rangle) = \begin{cases} 52Pa \text{ compliant substrate} \\ \\ 543Pa \text{ stiff substrate, II'.} \end{cases} \tag{2.14}$$

The traction stresses obtained this way are certainly consistent with those measured by Elosegui-Artola *et al.* [4, 99] who, incidently used the data and analysis of Litvinov *et al.* [97]. These traction stress levels are also consistent with those reported by Gardel *et al.* [25] for PtK1 epithelial cells supported on acrylamide gel substrates with elastic moduli in the 3-5 kPa range. We note, however, that they [25] also report actin flow rates in the 10-30nm/s range, *i.e.* considerably lower than used herein. Traction stresses in our above range < 300Pa are, however, much lower than reported by, *e.g.*, [44, 45, 65, 100] where traction stresses are in the 1-10kPa range. This is discussed below.

Specific estimates of the *mean expectation steady state traction stresses*

Elosegui-Artola *et al.* [4] provide a case study in which they measured traction stresses with variable substrate rigidity and in which they documented actin flow speed. The system they studied involved breast myoepithelial cells bound to fibronectin through either $\alpha5\beta1$ (expressed constitutively) or $\alpha\text{v}\beta6$ integrins (selectively expressed in cancer development). Figures 2.8a,b show selected data for measurements performed on cells expressing one or both integrin types. Specifically, their data from their Figs. 4j,k, along with our simulated results are shown in Fig. 2.8a for both types of integrins, whereas their data from their Figs. 4 d,e involving only $\alpha5\beta1$ integrins, along with our forecasted results, are shown in Fig. 2.8b.

We note that we were able to match their actin flow speeds reasonably well by simply using the variable speed relation given in eq. 2.10 with $\dot{x}_0 = 100\text{nm s}^{-1}$ and with an exponent of $n = 0.8$, and our forecasted $\langle f \rangle$(t). We also note that the *expected actin*

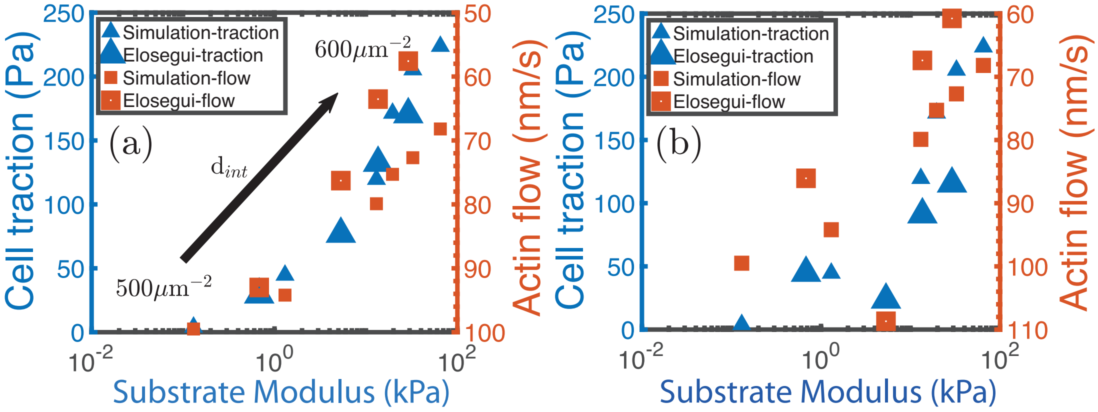

Figure 2.8. Traction stress *vs.* substrate stiffness; comparison between experiments [4] and simulation. Note that the left-side *expected actin flow rate* axis has been inverted to facilitate correlation with the traction stress axis.

flow rate is not $\dot{x}(t)$ as computed from eq. 2.10 as that rate depends on talin being actually engaged and under force; rather the *expected actin flow rate* should be computed using the bonding survival function, $-\mathrm{d}\mathcal{B}/dt$, as

$$\langle v_f \rangle = -\int_0^\infty \dot{x}(t)\,\frac{\mathrm{d}\mathcal{B}}{\mathrm{d}t}\,dt, \tag{2.15}$$

where $\mathcal{B}(t)$ is computed using the actual forecasted forces along talin (see Appendix B). The measured, *i.e.* observed, actin flow rate depends on an ensemble of talin rods bound to the actin skeleton and to integrins on the ECM. In the ensemble, individual talin rods that are engaged come and go, of course. We used initial integrin densities *vs.* substrate stiffness in accord with those reported in [4] as listed in Figs. 2.8; in particular, we use integrin densities in the range $500\mu\mathrm{m}^{-2} \leq d_{\mathrm{int}} \leq 600\mu\mathrm{m}^{-2}$ as indicated in Fig. 2.8a. To estimate $\mathcal{P}_b$ we again use the kinetic analysis of Litvinov *et al.* [97], whereby we estimate that for the two catch bond states, $i = 1, 2$,

$$\mathcal{P}_b^{(i)} = \frac{1}{1 + K_D^{(i)}/d_{int}}, \quad i = 1, 2 \tag{2.16}$$

where $K_D^{(i)} = k_{\text{off}}^{(i)}/k_{\text{on}}^{(i)}$. As we lack sufficiently complete kinetic data for either $\alpha5\beta1$ or $\alpha v\beta6$ integrins we use data for $\alpha IIb\beta3$ integrins [97] who report 2D dissociation constants $K_D^{1,2} = 1.7 \times 10^4, 2.6 \times 10^3 \mu\text{m}^{-2}$. From these and eq. 2.16 we estimate $\mathcal{P}_b = \mathcal{P}_b^{(1)} + \mathcal{P}_b^{(2)} \sim 0.175$ as above. The expected steady state traction stresses so determined are plotted *vs.* those reported by Elosegui-Artola *et al.* [4].

Although the agreement shown in Figs. 2.8a,b is encouraging, we note that although we use, *i.e.* in Fig. 2.8b, the measured catch bond parameters for $\alpha5\beta1$ integrins [3] to estimate bond survival (see also Appendix B), we use the same parameters for the combination of $\alpha5\beta1$ and $\alpha\text{v}\beta6$ integrins for the case of Fig. 2.8a. This we have done due to a lack of independently measured catch-bond properties for $\alpha\text{v}\beta6$ integrin - fibronectin bonds. Moreover, although we have adequate catch bond data for estimating $\alpha5\beta1$ bond survival we lack reliable kinetic data to estimate $\mathcal{P}_b$ and hence used such data for $\alpha IIb\beta3$ from [97]. We note, however, that Elosegui-Artola *et al.* [4] measured simple rate constants k_{on} and k_{off} and found $k_{\text{on}}^{\alpha\text{v}\beta6}/k_{on}^{\alpha5\beta1} \approx 0.5$ and $k_{\text{off}}^{\alpha\text{v}\beta6}/k_{\text{off}}^{\alpha5\beta1} \approx 30$! This they “compensated for” by also noting that, when observed on the substrate surface, $d_{\text{int}}^{\alpha\text{v}\beta6}/d_{\text{int}}^{\alpha5\beta1} \approx 5$. This *ad-hoc* compensation is far from exact but may help explain the roughly similar behavior shown in Figs. 2.8a and 2.8b. They reported $d_{\text{int}}^{\alpha5\beta1} \approx 500\mu\text{m}^{-2}$ as indicated in Fig. 2.8a. Aside from that just mentioned, however, we make little other *ad-hoc* “fitting”. Below, in the discussion we point out additional concerns and requirements for improved theoretical understanding and forecasting of cell adhesion and mechanotransduction.

2.7 Discussion

2.7.1 General discussion & required parameters

The analysis presented above revealed a number of notable features of force transmission along the adhedsome. Among these are that the effects of mechanosensitivity appear all along what we have dubbed the *force-train.* Indeed, these effects are directly related to the time rate of force development as seen in the behavior of both talin, and integrin, bonding. Hence, it would seem to be improper to simply relate force development to one particular set of “clutch bonds” that are envisioned to operate at one, or another, location along the actin-vinculin-talin-integrin-ligand-ECM train. We now discuss the various parameters and elements of our model that play important roles in the development of traction force and stress.

As an example, the response of talin *vis-à-vis* the actin-vinculin-talin reinforcement is intriguing, especially as it pertains to the early stage of talin force loading. The response of talin also illustrates the point made just above that focusing attention on just generic set of clutch bonds is misleading and renders the force train system ill-described. Specifically, in Section 2.4 we discussed the presumption that talin is initially “loaded” by actin bonding to $ABS3$ and then *via* the activation of $ABS2$ upon a conformational change of talin under modest forces (*i.e.* before talin domains unfold). The precise behavior of such bonding, however, is not yet quantitatively understood and hence is a topic of needed future study. Hence, not a simple parameter per se, the early engagement of talin to the actin skeleton requires more quantification in terms of bond strength, character, and survivability. We, in lieu of this quantitative information, made the assumption that actin-talin bonding had to survive for periods of time in the range of 2-3 seconds so that forces sufficient to induce talin unfolding (at, say, domain $R3$) and thereby vinculin reinforcement can be generated. Recently, Atherton *et al.* [92] have, however, shed additional light on this phase of the loading process, as briefly discussed next.

Consistent with our view in Fig. 2.1, Atherton *et al.* [92] propose that talin is recruited to the RAP/RIAM complex [101] at nascent adhesions where it binds integrins. Interaction with integrin renders $R3$ accessible for vinculin activation and binding and this leads to unmasking $ABS2$. At this point (before talin domain unfolding at, say $R3$) the focal adhesion is ready to engage the actomyosin engine. We assume that this process “buys some time” for eventual talin unfolding that then allows for additional talin-vinculin bond reinforcement. We assume (see Figs. 2.5b and 2.7b) that this takes 2-3 critical seconds; this depends on loading rate and thereby on substrate stiffness. Those talin rods that do not survive such critical seconds are released from the ensemble of talin rods. Clearly, this phase of the force process requires additional quantitative study as does the development of integrin density and distribution as discussed next. Indeed, Atherton *et al.* [19] have shown that fibroblast cells containing talin $ABS2$ mutants displayed traction stresses that were 45-50% less than TalFl. Hence without a full account of the talin force *vs.* time response quite misleading results on any assessments would be in error.

Our model analysis makes use of the catch bond theoretical framework of Thomas *et al.* [56] and the specific data of, *inter alia*, Huang *et al.* [6], Kong *et al.* [3], and Litinov *et al.* [97]. We note, however, that although adequate characterizations of catch bond survivability are obtainable by the methods described in such work, kinetic parameters for bond formation are not always readily available, especially since bond formation and re-formation may occur under non-equilibrium conditions. The work of Litinov *et al.* [97] is of specific interest here and hence we used there results as an example, as have others, *e.g.* [4, 99].

2.7.2 Integrin density and clustering

Estimations of traction stresses as attempted in Sections 2.6.1 and 2.6.1 illustrate the vital need for quantitative perspective on integrin density, integrin-ligand bond survival and, as we believe, on integrin distribution. This will be vital to continue our analysis to describe the full time evolution of adhesion sites. We comment on several of these aspects below.

Elosegui-Artola *et al.* [4, 99] have provided experimental data that showed a significant dependence of integrin density (d_{int}) on substrate stiffness. By using this correlation as input to their simple “clutch bond” model they were able to rationalize their observations of increasing traction stress - that we call $\mathcal{T}_{\text{ss}}$ - with increasing substrate stiffness.

Both the analysis of Sections 2.6.1 and 2.6.1 and our mechanistic reasoning, however, clearly suggest that this aspect of the adhesion process requires a great deal more attention. This requires accounting for not only integrin type, but also cell type and cell membrane/glycocalyx structure, and substrate morpholgy/topology. We note just below that substrate viscoelasticity *vs.* elasticity needs also to be considered.

Extracellular matrices, *e.g.* those composed of crosslinked polyacrylamide hydrogels for one, display essentially elastic behavior characterized by time independent linear force (stress) *vs.* displacement(strain) response. Yet reconstructured cell matrices exhibit a time dependent viscoelastic response, *i.e.* force (or stress) relaxation when held at a sustained displacement(or strain) or a relaxed rate of force(or stress) increases at a fixed rate of stretching (or straining). Indeed, effects of increased cell spreading, proliferation, and differentiation have been described for mesenchymal(MSC) cells on substrates displaying increased viscoelastic stress reduction behavior [72, 102]. The effects were attributed to increased integrin density and clustering although no rationale was provided for why, or how, viscoelastic response contributes to integrin clustering [72, 102]. However, such an effect may be consistent with our model scenario for integrin clustering as shown in Fig. 2.2. The bonding of integrins to ECM ligands invokes an initially nearly elastic response of the cell's membrane/substrate as we envisioned. This leads to enhanced clustering on stiffer substrates. Yet once clustered, and under force f_b, the relaxation of the substrate will lead to a further reduction in energy and thereby stabilization of the clusters. We expect this process will reduce the internal force in the integrins, but stabilize their positions.

On the latter point, we note that it now appears clear that ligand/integrin patterning as well as substrate morphology and topology must be explicitly accounted for. The effects of topology and patterning are distinct from density *per se.* The results of Maheshwari *et al.* [103] are most relevant here in that they demonstrated how fibroblast cell adhesion depended quite sensitively on ligand cluster patterns as well as on overall ligand density. But to put an even finer point on this, we note the reported evidence of the effects of surface (nanoscale topology) on adhesion. Examples include, *inter alia*, the effect of patterns of nanoscale silica beads [10, 57] and the nanoscale protrusions that exist on the surfaces of nanostructured metals and alloys [10, 59].

Herein we have not considered the full time evolution of integrin clustering and density *per se*, but computed what we called *steady state expectation* traction stresses; these were based on observed integrin densities as used to obtain for example the results of Fig. 2.8. Indeed although much has been reported on the formation of nascent adhesion clusters, see *e.g.* [63, 64], there does not exist as yet a fully predictive theoretical framework for such cluster development. A number of compelling ideas exist, however, which should eventually emerge into such a framework; examples include the role of membrane and glycocalyx distortions (see *e.g.* [69, 78, 104] and the ideas presented herein). Herein we present a remarkably simple analysis that captures much of the effects and that leads to a simple pathway to computing integrin interaction forces that are readily incorporated into simulation models that would, in fact, reveal clustering. But that may not be nearly enough. Consider, for example, the reports of Cheresh and co-workers, *e.g.* [105–107], who uncover important effects on cancer cells of Galectin-3 and, indeed, the localization of gangliosides such as GD_2 and GD_3 on integrin aggregation and clustering. These observations, along with the reported diverse effects of substrate topography [10], cell glycocalyx [69, 78], membrane distortions [104], just to mention a few factors, suggest that far more study is required to even define a credible pathway for such predictive models. Such models may be quite system specific as general rules and principles have yet to emerge, even for say the effects of substrate topography [10].

2.7.3 Concluding discussion

The current study has attempted to follow a minimal, yet detailed, account of the force-train along a realistic model adhesome. In doing so, the analysis revealed that mechanosensitivity is manifest at each step, and even sub-step, along the force pathway. This, itself, makes the analysis unique and useful in that it illustrates where vital quantitative perspective is missing and how it would enable more definitive understanding of how a given system works.

A most vital issue would appear to be the question of integrin/ligand density and patterning on a given substrate and how these affect integrin bond kinetics. Given the far reaching implications of how cells sense, adapt, and develop based on their environments [56] this may well represent a prime focus for future study. We have modeled integrin bonding using available data, *e.g.* that of Kong *et al.* [3], and this would benefit from a more detailed assessment by looking individually at both the talin-integrin and integrin-ligand bonding as data becomes available. However, it is critical to understand that this will require a range of data and information typically unavailable in most published studies. Such detailed information will include, *inter alia*, substrate elasticity [33,58](viscoelasticity) [102]; substrate morphology, topography and nanoscale roughness (in both detailed qualitative and quantitative character) [10]; ligand type, density and patterning [103]; integrin type and (initial) density [4,99]; cytoskeleton kinetics [6]; and the presence of plaque proteins as we have described [7,19,92]. Indeed, as we have cited, there are many puzzle pieces of this grand puzzle to be found in the literature, but these pieces are incomplete and are often not necessarily from the same puzzle. Hence we support the research suggestion of Lord *et al.* [10], *viz.* the “set up of very well-defined, much reduced model systems that can be thoroughly analyzed and large scale screening of cellular response to ...”. We add to this that a single such system will not suffice to navigate through the particularities of any given system and hence parallel systems are required. Hence a coordinated multi-group effort may be needed. The framework we have presented herein is indeed adaptable, and readily expandable, to provide quantitative verification of model concepts.

We conclude by noting that other models exist that consider a model adhesome such as ours and address questions such as adhesion growth and mechanosensitivity, but they analyze the adhesome’s elements in fundamentally different ways; an interesting case in point are the models of Cao *et al.* [108,109]. For example, their model elements [108] are modeled as rate independent, loading (or stretching) history independent, linear elastic, elements. In contrast, our model explicitly treats each element as a thoroughly non-linear, stochastic, hence rate and history dependent molecular based element; moreover, we use a wide range of experimental biophysical data to calibrate each element, including the stochastic bonding of each element to each other. Hence the two models have an entirely different composition. Moreover, our results demonstrate quite clearly that simply replacing linear elastic elements with an "effective non-linear element" derived, for example, from our model may not produce similar outcomes; for example, and as just one example, the analysis of just the $\langle f \rangle$ *vs.* time results obtained assuming a constant stretching *versus* a moderately variable rate of Figs. 5a and 7a illustrate that point clearly. Yet, what may be possible is to enhance our model adhesome by including a nucleus, as in the Cao *et al.* model [108], and pose questions as posed by them. Their framework would seem naturally suited to our molecular based, stochastic, approach. Likewise, models that describe either the growth or the survivability of FAs, *e.g.* [110,111], may be incorporated into a framework such as ours for a more complete description of the development of traction stress.

Acknowledgement

The authors would like to thank Drs. Christoph Ballestrem, Univ. of Manchester, Wendy Thomas, Univ. of Wasington, and Michael Sheetz, Columbia Univ. for valuable discussions related to this work.

Chapter 2, in full, is a reprint of the material as it appears in *Biophysical journal* 117.9 (2019): 1599-1614. Asaro, Robert; Lin, Kuan-Po; Zhu, Qian, 2019. The dissertation author was the primary investigator and author of this paper.

Appendix A. Talin unfolding

We use the framework of Zhu and Asaro [23] to describe the time-force evolution of folding and unfolding of talin; the parameters are listed in Table 2.2. We consider the transitions between two states $f \leftrightarrows u$, folded (f) and unfolded (u) separated by energy barriers $\Delta E_{f\to u}$ and $\Delta E_{u\to f}$. The energy barriers are affected by force and hence, *e.g.* for unfolding

$$\begin{aligned}\Delta E_{f\to u} &\approx \Delta E^0_{f\to u} + \frac{\partial \Delta E_{f\to u}}{\partial f} f + ...\\ \Delta E_{f\to u} &\approx \Delta E^0_{f\to u} - f\Delta x_{f\to u} + ...,\end{aligned} \tag{2.17}$$

which formally and operationally defines an unfolding *activation distance* as $\Delta x_{f\to u} \equiv -\partial \Delta E_{f\to u}/\partial f$. For the unfolding rate we thus have

$$k_{f\to u} = \vec{k} k^0_{f\to u} \mathrm{e}^{f\Delta x_{f\to u}/kT}. \tag{2.18}$$

A similar analysis leads to the refolding rate

$$k_{u\to f} = \overset{\leftarrow}{k} k^0_{u\to f} \mathrm{e}^{f\Delta x_{u\to f}/kT}, \tag{2.19}$$

where we note that the transition distance for refolding is such that $\Delta x_{u\to f} < 0$. The model continues by defining the end-to-end distance, x, as

$$\frac{x}{NL_f} = (1-\phi_u)\frac{x_f}{L_f} + \phi_u \frac{x_u}{L_u}\left(\frac{L_u}{L_f}\right), \tag{2.20}$$

with L_f and L_u being the contour lengths of the folded and unfolded domains, respectively and x_f and x_u being the projections extensions, in the direction of f of folded and unfolded domains, respectively; N is the total number of foldable plus unfoldable domains.

A freely jointed chain model [24] was then used which led to the relation

$$\frac{x}{NL_f} = (1-\phi_u)\mathcal{L}\Big(\frac{2fp_f}{kT}\Big) + \phi_u\mathcal{L}\Big(\frac{2fp_u}{kT}\Big)\Big(\frac{L_u}{L_f}\Big), \tag{2.21}$$

where $\mathcal{L}(\zeta) = \coth\zeta - 1/\zeta$, and p_i is the persistence length of an folded or unfolded domain, *i.e.* $i = f, u$.

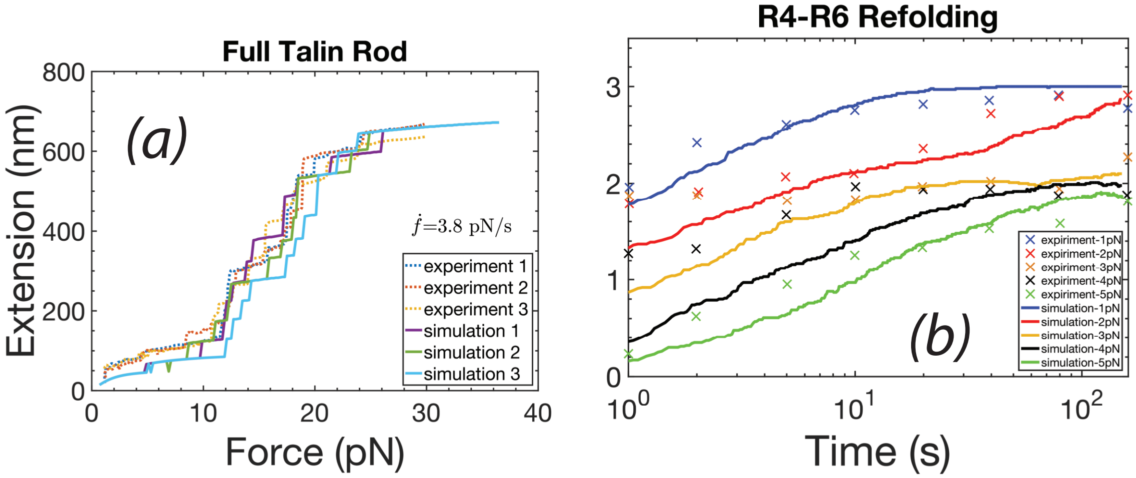

Figure 2.9. (a) Unfolding of a full talin rod compared to the experimental measurements of Yao *et al.* [1, 2]; unfolding as observed under imposed force rate. (b) Talin domain refolding.

The times steps used were $\Delta t = 0.01$s.

Appendix B. Catch bonds

The model allosteric protein we envision has two minimum energy conformations separated by an energy barrier; the barrier height above state 1 is ΔE_{12} and above state 2 is ΔE_{21}. The transition rates between these states in the absence of force are k^0_{12} and k^0_{21} where these are in turn proportional to $\mathrm{e}^{-\Delta E_{ij}/kT}$. Since the protein can bind the ligand from either state, we assume it can unbind from either state with unbinding energies ΔE_{10} and ΔE_{20}; this leads to unbinding rates k_{10} and k_{20}.

Upon the application of force, f, these energy barriers decrease by $f\Delta x_{ij}$ so that

Table 2.2. Parameters used to describe the unfolding and refolding of the talin rod domains $R1 - R12$. Parameter fits were based on the data of Yao *et al.* [1,2].

Talin domain	1	2	3	4	5	6	7-8	9	10	11	12
folded size (nm)	5	5	5	5	5	5	5	5	5	5	5
unfolded size (nm)	69.2	52.4	49.6	52.4	64	60.4	118.4	66.8	63.2	66.4	62.8
$k_{f \to u} \, (s^{-1})$	4.2e-6	1.7e-8	0.018	4.2e-6	2.5e-5	2.5e-5	4.2e-6	4.2e-6	2.5e-5	2.5e-5	1.7e-8
$\Delta x_{f \to u}$ (nm)	3.1	3.4	5.7	3.1	4.1	4.1	3.1	3.1	4.1	4.1	3.4
$k_{u \to f} \, (s^{-1})$	1.606	0.1318	1e6	22.387	2.57	2.57	22.387	123	123	123	123
$-\Delta x_{u \to f}$ (nm)	4.28	4.14	9.86	4.04	11.5	11.5	13.6	10.35	10.35	10.35	10.35

Table 2.3. Kinetic rate constants for vinculin-actin catch bonds taken from Huang *et al.* [6]

Transition	Rate constant (1/s)	transition distance (Å)
$1 \to 0$	$k_{10}^0 = 5.3$	$\Delta x_{10} = 0$
$2 \to 0$	$k_{20}^0 = 5.5 \times 10^{-3}$	$\Delta x_{20} = 1.2$
$1 \to 2$	$k_{12}^0 = 6.1$	$\Delta x_{12} = 0.4$
$2 \to 1$	$k_{21}^0 = 43$	$\Delta x_{21} = -3.4$

the transition rates become

$$k_{ij} = k_{ij}^0 \mathrm{e}^{f\Delta x_{ij}/kT}. \tag{2.22}$$

To compute bond lifetimes we define $\mathcal{B}_1(t)$ and $\mathcal{B}_2(t)$ as the probability of occupancy of state 1 or state 2, respectively. Hence these evolve from the coupled ODE's

$$\begin{aligned} \frac{d\mathcal{B}_1(t)}{dt} &= k_{21}\mathcal{B}_2(t) - (k_{10}+k_{12})\mathcal{B}_1(t) \\ \frac{d\mathcal{B}_2(t)}{dt} &= k_{12}\mathcal{B}_1(t) - (k_{20}+k_{21})\mathcal{B}_2(t). \end{aligned} \tag{2.23}$$

The probability of a bond in either state be occupied is $\mathcal{B}(t) = \mathcal{B}_1(t) + \mathcal{B}_2(t)$. Hence eqs. 2.23 must be integrated through a given force *vs.* time history, subject to initial conditions.

We note that the expectation lifetime of a bond may be computed from the negative derivative of the survival function, *viz.* $-(\mathrm{d}\mathcal{B}(t)/dt)\mathrm{d}t$ as

$$\langle\tau\rangle = -\int_0^\infty t'(\mathrm{d}\mathcal{B}(t')/\mathrm{d}t')\mathrm{d}t' = \int_0^\infty \mathcal{B}(t')\mathrm{d}t', \tag{2.24}$$

where the second equality follows *via* integration by parts provided $\lim_{t'\to\infty}\{t'\mathcal{B}(t')\} = 0$. For actin-vinculin bonds we have fitted the catch bond model as described by Thomas *et al.* [79] to the data of Huang *et al.* [6]. Results are listed in Table 2.3.

Table 2.4. Kinetic rate constants for integrin catch bonds taken from Kong *et al.* [3]

Transition	Rate constant (1/s)	transition distance (Å)
$1 \to 0$	$k_{10}^0 = 6.01$	$\Delta x_{10} = 1.37$
$2 \to 0$	$k_{20}^0 = 0.021$	$\Delta x_{20} = 2.112$
$1 \to 2$	$k_{12}^0 = 0.42$	$\Delta x_{12} = 0.58$
$2 \to 1$	$k_{21}^0 = 0.105$	$\Delta x_{21} = -0.42$

B.1 Integrin-fibronectin (ligand) bonds

For integrin catch bonds we used the data of Kong *et al.* [3] for integrin-ligand bonds and determined *vis-à-vis* the catch bond model described by Thomas *et al.* [79] the parameters shown below in Table 2.4.

With the calibrations given in Tables 2.3 and 2.4, we compute the average bond lifetimes at constant forces as shown in Fig. 2.6b for both the actin-vinculin [6] and integrin-fibronectin bonds [3]. In Fig. 2.10b we plot the probability *vs.* time curves computed from the integration of eqs. 2.23 using the force *vs.* time response of Fig. 2.5c for an average talin rod of an integrin-ligand bond using the data of Table 2.4. In Fig. 2.10 we plot the probability *vs.* time curves, again for an integrin-ligand bond using initial conditions that differ from those used to compute Fig. 2.10b.

The initial condition $\mathcal{B}_1^0/\mathcal{B}_2^0 = k_{21}/k_{12}$ assumes that bond states 1 and 2 equilibrate as we discuss in the text and has been assumed elsewhere [95]. The survival *vs.* time behavior, as we see, is quite sensitive to the initial conditions $\mathcal{B}_1^0$ and $\mathcal{B}_2^0$ for the initial probabilities of finding a bond in the low force state 1 and high force state 2. In Figs. 2.10c,d it is assumed that the bond state transitions $1 \leftrightarrows 2$ equilibrate so that $\mathcal{B}_1^0/\mathcal{B}_2^0 = k_{21}/k_{12}$; we call these initial conditions II and II' designating that the initial force on the bond is $f_b^0 = 0$ or $f_b^0 > 0$, respectively. For the case of Fig. 2.10d we used $f_b^0 = 3$pN. However, Thomas *et al.* [56] point out that "the initial conditions depend on experimental conditions"

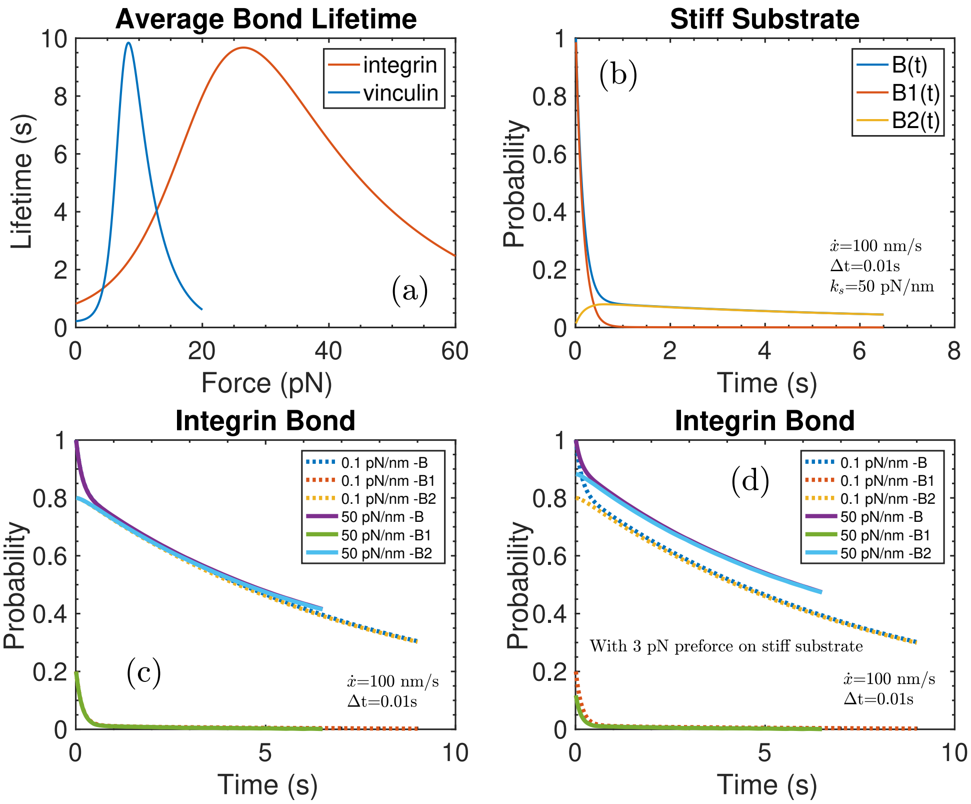

Figure 2.10. (a) Average bond survival times *vs.* an assumed constant force for both vinculin and integrin catch bonds. (b) Probability of integrin bond survival *vs.* time using the force *vs.* time responses shown in Fig. 2.5c using initial conditions based on the law of mass action, *i.e.* eq. 2.25 [56]. (c) Probability of integrin bond survival *vs.* time using the force *vs.* time responses shown in Fig. 2.5c but using for initial conditions of bonds in states 1 or 2 the criterion $\mathcal{B}_1^0/\mathcal{B}_2^0 = k_{21}/k_{12}$, and at zero initial force. (d) Same as (c) but here it is assumed that a pre-force of 3pN exists when integrin bonds are formed.

and for their conditions they used a principle of "detailed balance" to estimate that, *e.g.*

$$\mathcal{B}_1^0 = \frac{J_1}{J_1 + J_2} = \frac{k_{12}^0 \cdot k_{10}^0}{k_{21}^0 \cdot k_{10}^0 + k_{12}^0 \cdot k_{20}^0}. \tag{2.25}$$

This initial condition, dubbed I, was used for Fig. 2.10b.

Here again, the time steps used were $\Delta t = 0.01$s.

Chapter 3

Nascent cluster

3.1 Introduction

Cells do not live alone (*non solus*), but instead vigorously interact with the environment which contains other cells as well as extracellular matrices (ECMs), the properties of which they sense by adhering and react to. For example, cells sense the mechanical response of their environment, *e.g.* stiffness [31,33,49,55,56,58] and even topography [10,15,57,103], as they proliferate [32], differentiate [33], migrate [31], as well as engage in the vital processes of cell development [34, 35], including, *inter alia*, tumorgenesis [36, 37], cell growth [38–40] and wound healing [41, 42], *inter alia.* Cells perform these functions and are so regulated *via* the formation of focal adhesions (*FA*'s) [43–46] that anchor the cell either transiently (*i.e.* dynamically) or permanently [47, 48] to, *e.g.* the ECM (*aka* the substrate); the precursor to FA's are nascent adhesion clusters as sketched in Fig. 3.1a, that we analyze herein.

The cell's adhesion complex and its protein components, the *adhesome* [9, 61], transmits force generated by force dependent retrograde flow of its intracellular actin cytoskeleton (*aka* hereafter "actin") *via* a series of proteins [7–9] that are bound to each other and ultimately to the cell's extracellular matrix. In our case we consider the adhesome to utilize the plague proteins talin and vinculin; hence our *force train* consists of actin(myosin)-vinculin-talin-integrin-ligand(ECM/substrate) [7, 8, 19]. This is sketched in Figs. 3.1b-c. It is, however, the initial formation of these adhesion complexes that we focus on here, *viz.* the formation of *nascent adhesion clusters*; these are described next, followed by our plan of study. A basic feature of these is the formation of well defined integrin clusters of, what appear to be, well regulated sized clusters containing controlled numbers of integrins of $\mathcal{O}(\sim 20-60)$ [63, 64]. How, and why, they form and what controls their size, of $\mathcal{O}(100-150\text{nm})$ in diameter [63, 64], and integrin numbers is a main object of our study.

3.2 Nascent adhesion clusters: background

Nascent adhesion clusters form in a step wise manner on substrates of all rigidities and do so within time scales of $\mathcal{O}(\sim 1-2\text{min})$ [63, 64, 71]; they appear, however, to be less persistent on rigid substrates [63]. They generally attain sizes in the range of $\sim 100 \pm 30\text{nm}$ and contain a number of integrins of $\mathcal{O}(\sim 20-60)$ [63, 64] as a general rule. It is noted that clustering does not require myosin driven actin contractility as described most recently for example by Sun *et al.* [112], nor generally is such involved in early cluster formation [62–64] as indicated in Fig. 3.1a. Integrin activation and ligation, *via* substrate ligands, is part of the process, yet clusters are observed to contain unligated integrins [63, 64] and this requires a mechanistic explanation. It is noteworthy that clusters appear to require a minimum ligand spacing of $\mathcal{O}(\sim 60\text{nm})$ to initiate [113, 114] which implies that ligated integrin interaction occurs at a distance, as in a field that decays with their separation; this interaction is, however, not short range as it appears to occur over distances of $\mathcal{O}(\gtrsim 60\text{nm})$, although only weakly so at larger distances. Since the integrin footprint is of $\mathcal{O}(\sim 42\text{nm}^2)$, we envision that the range of interaction is clearly of $\mathcal{O}(r_i \geq 2\sqrt{42/\pi} \approx 8-10\text{nm})$, where r_i is the effective radius of an activated integrin. Hence, once clusters initiate, additional integrins generally join within increasing their number density.

It is interesting that Changede and Sheetz [64] hypothesize, but do not prove, that "...

integrins will cluster even in the absence of bound ligands through activation by cytoplasmic proteins (*e.g. talin*) *or* Mn^{++}". The earlier findings of Cluzel *et al.* [62] put an overarching and finer point on the above. They reported, for $\alpha v\beta 3$ integrins on mouse melanoma cells and hamster CS-melanoma cells, that, *inter alia*, "Mn^{2+} *activation resulted in the formation of integrin clusters in cellular regions devoid of F-actin*"; their *de nova* clusters formed after integrin activation with Mn^{2+} even after treatment with cytochalasin D (cD), *i.e.* after "... *destruction of the actin cytoskeleton with cD*". Now, immunofluorescence staining for talin, however, "... *revealed an overlap with all clustered EGFP integrins in* Mn^{2+}*-treated cells*"; EGTP cells, expressing $\alpha v\beta 3$ integrins are described by Ballestrem *et al.* [65] who studied adhesion in similar cell lines. Consistent with absence of F-actin in *de novo* clusters, Cluzel *et al.* [62] found "... *the focal adhesion adaptor proteins vinculin, paxillin, and FAK, as well as antiphosphotyrosine antibodies, did not associate with the de novo-formed clusters of activated integrins*".

So far, the above observations may suggest a scenario as depicted in Fig. 3.1a where a preliminary view is shown that is to be enhanced below. Here activated integrins, that are associated with at least talin and kindlins, tend to cluster. We assume for now that they are recruited *via* their lateral mobility, *i.e.* by diffusion [115], to cluster from a certain initial distribution within the cell's membrane; we take this distribution to be of various types in what follows and assess the expected trends *via* a model simulation to be described. Figure 3.1b illustrates the later adhesion step where engagement with the actin cytoskeleton occurs and where force is applied *via* retrograde flow of the cytoskeleton; Fig. 3.1c illustrates where manotransduction occurs *via* the nuclear influence felt of the adhesion's actin-vinculin-talin-integrin-substrate *force train* [116–118]. Before we present the first of our cluster simulation models, we add, or at least emphasize, a few finer points on nascent integrin clusters.

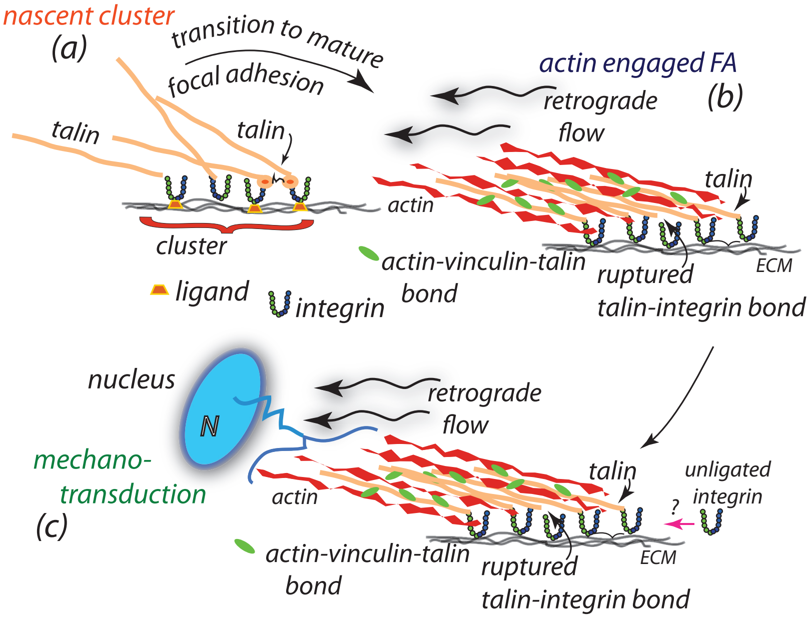

Figure 3.1. A rough possible scenario for the temporal pattern of imposed *driving force* "a" and venous slit caliber "c" *vs.* time. Note various time scales discussed in the text.

3.2.1 Finer points regarding the background on nascent clusters

Integrin activation has been studied extensively [5, 76, 83, 87, 119–125], most particularly with respect to the role of activating adaptor proteins, such as talin, kindlins and paxillin [87, 122, 126] and also with regard to the potential role of integrin clustering [87]. We refer to Fig. 3.2 for a brief discussion, and we specifically use data and observations for $\alpha_{III}b\beta3$ and $\alpha v\beta1$ integrins.

The three integrin conformational states depicted are known to possess distinctly different affinity states for binding ligands [5, 87, 119, 122] where the *extended open* (EO) state affinity is some 5000 fold times greater than that of the *bent closed* (BC) state [5]. Extension presents a significant barrier to activation requiring, for example, ~ 16kJ/mol for $\alpha v\beta1$ integrins [5]. Hence, in this context, we may refer to the extended states, EC and EO, as being *activated* [87, 122]; roughly speaking the physical extension undergone from the BC to EO state is of $\mathcal{O}(\sim 10\text{nm})$ [87]. Ye *et al.* [87] demonstrated that the association

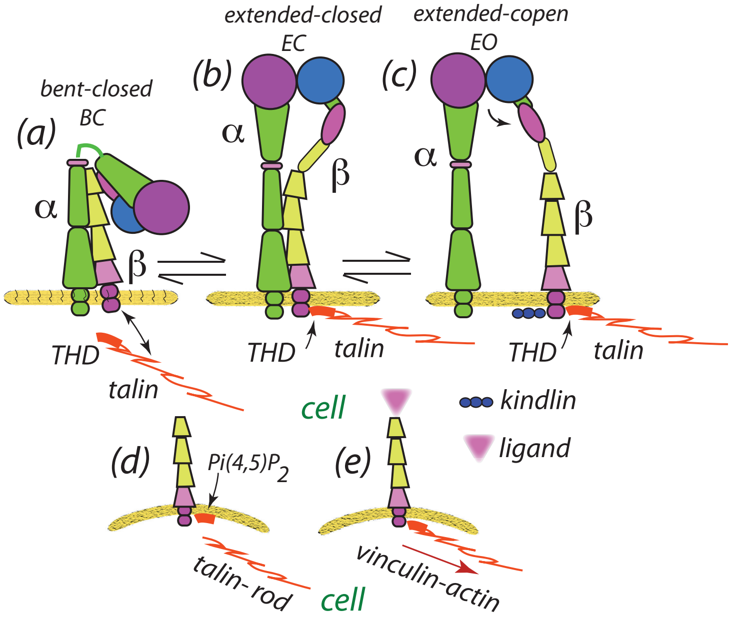

Figure 3.2. Three conformational states of $\alpha_{III}b\beta_3$ integrins: (a) *bent closed* (*BC*); (b) *extended closed* (*EC*); and (c) *extended open* (*EO*).In the *BC* abd *EC* states the α transmembrane domains (TM) are orthogonal to the membrane while in the *EO* is opened [5]. Note the association (binding) of the F2 residues in the THD to acidic membrane phospholipids [127] and the association of kindlinds with the THD that supports integrin activation. (d,e) Binding of THD at the integrin β tail, especially when the TR is re-associated with the THD, is deformed so as to develop curvature.

of the *talin head domain* (THD) with the β tail of integrin is sufficient - providing integrins are embedded in a lipid bilayer and with a talin membrane binding site - to induce integrin activation; this is indicated in Figs. 3.2b-e as explained below. Saltel *et al.* [127] have found that the THD binds to acidic lipids, *viz.* PI(4,5)P_2, which is part of the activation process; the participation of kindlins is discussed below. In fact, this process is facilitated by a dissociation with the talin rod (TR) which may re-associate upon its connection to actin *via* vinculin; this is depicted in Figs. 3.2d-e. Saltel *et al.* [127] provide interesting perspective on this. For example, they point out that one of the consequences of the THD, *sine* TR, binding to the intergrin β tail "... *is the absence of vinculin recruitment and uncoupling* (*i.e.* uncoupling) *from the F-actin network*". They appear to argue that the membrane binding of a dissociated THD, *via* PI(4,5)P_2 promotes clustering and then a re-association with the TR and the actin cytoskeleton. We hypothesize that may occur *via* the schema of Figs. 3.2d-e. The THD binding will induce a membrane distortion as shown in Figs. 3.2d-e; this is reminiscent of the protein membrane distortions simulated by, for example, Reynar *et al.* [128,129] and van der Wel *et al.* [130] who simulated protein clustering within lipid membranes. As described below, this provides a mechanism for integrin clustering.

Binding of the THD to the β tail in integrins has been described early on by Calderwood *et al.* [120] and Garcia-Alvarez *et el.* [121] and, although the applicability of what has been reviewed here to most integrins is unsettled as yet, we note that Calderwood *et al.* [120] had noted that "... *there is general agreement that the activity of leukocyte and platelet integrins are regulated by talin, and talin-mediated activation of integrins containing* $\beta 1, \beta 2$ *and* $\beta 3$ *units has been reported in a range of cell types*". We thereby will take this as a sensible basis for a basic model formulation as detailed below. At this point we turn to a brief discussion of the important role of kindlins.

The potential role of kindlin association, in collaboration with talin, must be emphasized as noted by Kammerer *et al.* [131] and Theodosiou *et al.* [126] following Calderwood *et al.* [122] and Bachir *et al.* [70]. This is discussed using Fig. 3.3 as a guide as well as Fig. 3.2. Kindlins co-locate with the THD at the integrin β tail as sketched in these figures and have been implicated in integrin clustering [126,131]. Theodosiou *et al.* [126] have reported on a most interesting study which provides additional perspective on the role of kindlins, acting in cooperation with talin, in developing both nascent clusters and mature focal adhesions. Importantly, their study concerns $\alpha v \beta 1$ integrin expressed within mice kidney fibroblasts, demonstrating a parallel with what has been described for $\alpha_{III} b \beta 3$ integrins. Theodosiou *et al.* [126] use their observations to pose the hypothesis that "... *not all integrin molecules have to be occupied by talin and therefore low levels suffice, particularly in NAs* (nascent adhesions) ...". As will be seen below, our model approach is consistent with this idea and we provide a mechanistic perspective for this observation and

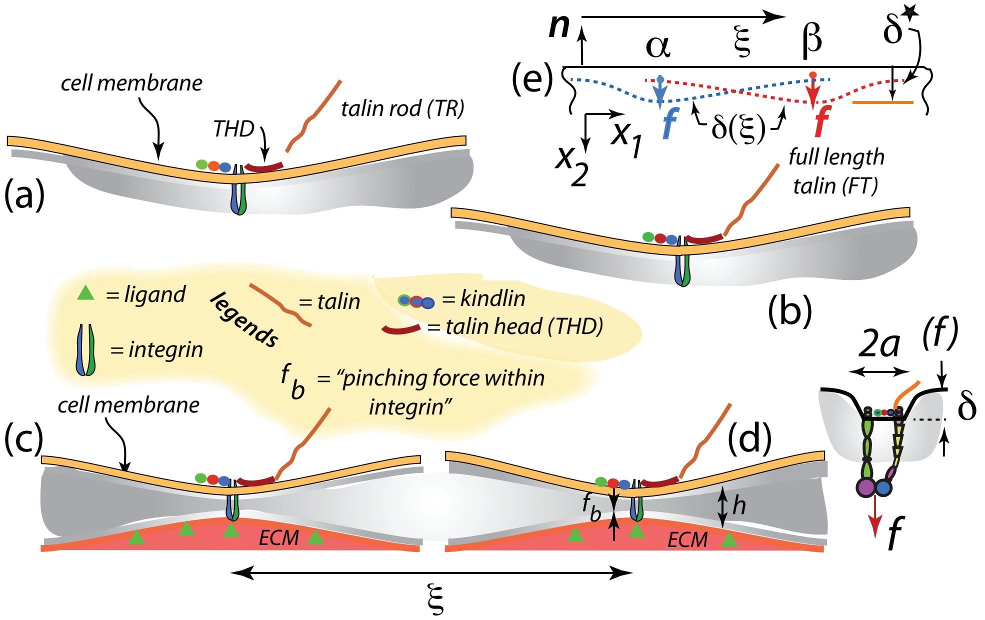

Figure 3.3. (a) THD and kindlins associate with the integrin β tail causing membrane distortion. (b) TR re-associates with THD and connects to actin cytoskeleton *via* vinculin (shown in Fig. 3.2c-d). (c,d) Two nearby and activated integrins, ligated or not, that interact via the deformation fields created by membrane distortion. (e) Integrins viewed as point forces, f, causing distortions; the distortions caused by each alone are sketched by the respective colored dashed lines. Note the displacement downward, $u_2(\xi)$ is called $\delta(\xi;\delta_0)$ where δ_0 is the maximum displacement beneath each point force. For a system modeled as linear elastic $\delta_0 = 1/kf$, k being a specific model dependent constant, and the total displacement is the linear sum of each dashed line. (f) A circular patch uniformly depressed, with a net force f_b, where $f_b = k\delta_0$ if this patch is not affected by other integrins.

interpretation. Theodosiou *et al.* [126] do state, however, "... *our study demonstrates that integrin* (*viz.* $\alpha v\beta 3$) *affinity regulation (activation) is essential for fibroblast adhesion and depends on both talin and kindlin-2*"; this supports the view of a more common function of talin and kindlins in integrin activation.

With respect to integrin activation, we note that Bachir *et al.* [70] have reported that whereas kindlin is recruited into nascent adhesions during their formation, talin follows in sequence just after, at least for $\alpha 5\beta 3$ integrins in migrating CHO cells; the generality of this finding to other systems was unspecified. Whether this corresponds to the talin rod (TR) or talin head domain (THD) is unclear. Such a sequence, proposed for

$\alpha5\beta3$ integrins for this particular system, does not alter our basic scenario. Changede and Sheetz [63, 64] have shown that integrin ligation, although not necessarily involving all or even most integrins within a nascent cluster, is required for nascent cluster formation and that may be accomplished by the THD or kindlin as discussed above.

Still additional insight was provided by in the most interesting studies of Ye *et al.* [87] who studied $\alpha_{III}b\beta3$ integrins embedded in liposome membranes and lipid nanodiscs bearing single or multiple embedded integrins with varying orientations protruding the nanodisc membranes. In this way they could include cases with and without the presence of ligands and thereby cases where there were no apparent cause for significant internal forces generated within the integrins. Ye *et al.*'s [87] observations using liposomes also demonstrated that, without ligands, "*... there was no gross integrin clustering when THD activated* $\alpha_{III}b\beta3$ *...*". Although clustering *per se* may not have been a focus of these studies, their observations would appear to support the view that ligand binding was required to induce clustering. However these observations, taken together with the observations of Theodosiou *et al.* [126], lead us to hypothesize that although clusters may require ligated integrins to form not all integrins attracted to, and incorporated within, formed clusters are ligated. We indeed suggest a reason why, and how, this may be so.

3.3 Clustering model: outline

We seek an essential model, with sufficient mechanistic detail, yet with optimal flexibility in that detail to readily allow for a wide range of specific model scenarios. A basis is the following, explained *via* the pairwise interaction of two integrins. As integrins activate, and extend, and bind to ECM ligands, they induce a deformation of the cell membrane and glycocalyx as well as possibly the ECM, if the latter should possess adequate compliance. Such deformation creates an internal force within the integrin and an elastic deformation field as sketched in Fig. 3.3e by the colored dashed lines; the magnitude of the deformations and force depends on whether the integrin is either ligated or merely activated. Now consider the integrins in Fig. 3.3e to be modeled as "point forces", f, or as internal body forces, f_b, as in Fig. 3.3c acting on, or within, the cell membrane at some distance, lying at a distance $\xi = |\xi_\alpha - \xi_\beta|$ apart. The distortions sketched are thereby $\delta(\xi; \delta_{0,\alpha})$ where δ_0 can be considered the displacement caused beneath a point body force acting of integrin α alone. Hence at the left, and right, side integrins

$$\begin{aligned} \delta_\alpha(\xi; f_\alpha) &= \delta_{0,\alpha} + \delta_\beta(\xi; f_\beta), \\ \delta_\beta(\xi; f_\beta) &= \delta_{0,\beta} + \delta_\alpha(\xi; f_\alpha), \end{aligned} \tag{3.1}$$

where δ_i, $i = \alpha, \beta$ are functions of the spacing ξ and $\delta_{0,i} = f_i/k$ where k is a linear stiffness factor that is specified by the particular model used as explained below *via* example; f_i is the force acting within the integrin which will depend on the pinching amount required to achieve the fixed amount of distortion. Equations 3.1 simply say *that the net displacement beneath force $i = \alpha, \beta$ is the sum of what is produced by the prevailing force on integrin i, f_i, and what is contributed at the site of i by the field of the other integrin.*

Now, we assume that for an integrin, say α, to be ligated it must create a total displacement of $\delta^\star$ and in that case $\delta_\alpha(\xi; f_\alpha) = \delta^\star$. To be sure, when an integrin, say α, is nearby another, say β, the internal force within it must induce an additional displacement $\delta_{0,\alpha} = \delta^\star_\alpha - \delta_\beta(\xi; f_\beta)$; the required force in α is then $f_\alpha = k(\delta^\star - \delta_\beta(\xi; f_\beta))$; the force f_α is mitigated by the displacement $\delta_\beta(\xi; f_\beta)$ contributed by integrin β at the site of α. It follows that as more integrins cluster about integrin α, $\delta_{0,\alpha}$ is reduced and may indeed tend to nearly vanish; hence the internal force $f_\alpha = k\delta_{0,\alpha}$ reduces which provides the translational force causing integrins to cluster; in fact, if two ligated integrins were to hypothetically merge, neglecting steric constraints that would bar this, they would appear as a single point body force in terms of their elastic field.

On the other hand, to ligate an integrin must acquire energy which tends to reduce the rate, *i.e.* probability, of ligating; this means that integrins tend to ligate with greater rate near already ligated integrins, and in particular near clusters. We find, however, that this may be insufficient to produce well defined and sustained clusters as will be explained below.

Now considering Fig. 3.3a-b, *i.e.* un-ligated integrins, we note that a similar story holds true. But un-ligated integrins should be considered mobile and hence a translational force that would bias their otherwise random diffusive motion is required. In fact, such integins would interact with each other and with ligated integrins for the reasons outlined above. This means that, given our scenario of Figs. 3.3a-b, un-ligated integrins may be attracted to ligated clusters as hypothesized by Changede and Sheetz [64].

The effective force that attracts integrins may be uncovered by a variation in the appropriate free energy upon translation of an integrin, *i.e.* upon a variation in ξ, or more precisely in $|\xi_\alpha - \xi_\beta|$, in Fig. 3.3e. In this, we view the forces as embedded body forces as sketched in Fig. 3.3e. We further note that we envision that the field is determined by the fixed amount of displacement imposed at the sites of the point forces, *viz.* $\delta^\star_\alpha$ and $\delta^\star_\beta$. There is no surface traction involved and hence the scenario is one of fixed imposed displacement; hence the free energy is the Hemholtz free energy, *viz.*

$$\mathcal{H} = \int_v w \, \mathrm{d}v, \text{ with } w = 1/2\sigma_{ij}e_{ij} \tag{3.2}$$

being the strain energy density. We designate $\mathbf{x}$ to be a general spatial position vector. With $\mathbf{u}(\mathbf{x})$ being the displacement, $e_{ij} = 1/2(u_{i,j} + u_{j,i})$; further, the the equations of equilibrium read may be written as $\sigma_{ij,j} = -b_i$, with $\mathbf{b}$ being the body force density. Given the symmetry in the Cauchy stress, $\boldsymbol{\sigma}$, we may further write that $1/2\,\sigma_{ij}e_{ij} = 1/2\,\sigma_{ij}u_{i,j} = 1/2\,(\sigma_{ij}u_i)_{,j} + 1/2\,b_i$, the last equality holding due to the equilibrium equations. Hence $\mathcal{H}$

of eq. 3.2 becomes

$$\mathcal{H} = \int_v \{1/2\,(\sigma_{ij}u_i)_{,j} + 1/2\,b_i\}\,\mathrm{d}v = \int_s 1/2\,\sigma_{ij}n_j u_i\,ds + \int_v 1/2\,b_i u_i\,\mathrm{d}v, \tag{3.3}$$

with s being the bounding surface to v, the volume; $\mathbf{n}$ is the outward pointing normal on s to v. As there is no traction on s, the first integral vanishes and

$$\mathcal{H} = 1/2 \int_v b_i u_i\,\mathrm{d}v. \tag{3.4}$$

If $\xi_{\alpha,\beta}$ are the positions of integrin α, β, then we may compute the force between them as

$$f = -\frac{\partial \mathcal{H}}{\partial|\xi_\alpha - \xi_\beta|} = -\frac{\partial}{\partial|\xi_\alpha - \xi_\beta|}\int_v b_i u_i\,\mathrm{d}v \text{ where } i = \alpha, \beta. \tag{3.5}$$

Note that, as this reads, f would be the force tending to separate them, *i.e.* if $f > 0$ a repulsive force. Now, by stipulation the integrins are localized "point forces" and hence we take

$$b_{\alpha,\beta} = f_{\alpha,\beta} = k\Big\{\delta^\star_{\alpha,\beta} - \delta_{\beta,\alpha}(|\xi_\alpha - \xi_\beta|)\Big\}\,\delta(x - \xi_{\alpha,\beta}), \tag{3.6}$$

where the Dirac functions, $\delta(x - \xi_{\alpha,\beta})$, localize the point forces at positions $\xi_{\alpha,\beta}$. Next, eq. 3.6 is substituted into eq. 3.5 where we note that the integration over volume v is over the variable $\mathbf{x}$, to obtain

$$f_{\alpha\leftrightarrows\beta} = f = \frac{1}{2}\Big\{f^\star_\alpha \frac{\partial \delta_\beta}{\partial|\xi_\alpha - \xi_\beta|}\Big|_\alpha + f^\star_\beta \frac{\partial \delta_\alpha}{\partial|\xi_\alpha - \xi_\beta|}\Big|_\beta\Big\}, \tag{3.7}$$

where $f^\star_{\alpha,\beta} = k\delta^\star_{\alpha,\beta}$. To be sure, a term such as $\partial\delta_\beta/\partial|\xi_\alpha - \xi_\beta|\Big|_\alpha$ represents the rate of change of displacement caused by the β integrin at the site of the α integrin with respect to the absolute magnitude of their distance, $|\xi_\alpha - \xi_\beta|$; as this is negative, the force tending to separate the integrins is negative, since $f^\star_\alpha > 0$. This means, in turn, that the integrins attract.

For an integrin that is ligated, or attempting to do so, its internal force would be computed from eq. 3.6, neglecting the Dirac functions of course. Ligated integrins are assumed to have limited mobility, yet for un-ligated integrins the interaction force is important in that it biases diffusion in favor or clustering. Un-ligated integrins are biased toward ligated integrins where the internal force required for ligation is reduced and hence the rate, *i.e.* the probability, of ligation is enhanced.

3.3.1 Specific integrin elastic model

We propose a simple model for an integrin as sketched in Fig. 3.3f where the uniform indentation of $\delta^\star$ is induced within a circular patch of radius $r = a$. The pressure under such an uniform indentation is $p(r) = p_0/(1-(r/a)^2)^{1/2}$; the net force, as pictured as f in Fig. 3.3e, is $f = 2\pi a^2 p_0$ [132]. The solution for the displacement field outside of the patch is given by Johnson [132] as

$$\begin{aligned} \delta(\xi) &= \frac{2(1-\nu^2)p_0 a}{E} \sin^{-1}\{a/\xi\}, \text{ for } a/\xi \geq 1, \text{ or} \\ \delta(\xi) &\approx \frac{(1-\nu^2)f}{\pi E} \frac{1}{\xi} \text{ for } a/\xi \geq 2 \\ f^\star_{\alpha,\beta} &= \frac{\pi a E}{1-\nu^2} \delta^\star_{\alpha,\beta} \rightsquigarrow k = \frac{\pi a E}{1-\nu^2}. \end{aligned} \tag{3.8}$$

These relations are used in eq. 3.7 to compute the interaction force and define the stiffness factor, also of eq. 3.7. In what follows we take $a = 3$nm to account for the integrin footprint of 42nm^2 [64] and the co-location of kindlin and the THD. As an estimate for integrin stretching, *i.e.* $\delta^\star$, we will generally take $\delta^\star \sim 10$nm When considering ligation, $\delta^\star$ will include the need to deform the cell membrane and glycocalyx and will be larger; in those cases $\delta^\star_{\alpha,\beta} = \delta^\star_\ell$, where subscript "$\ell$" signifies ligation. To gain perspective on this numerology, we estimate the magnitude of f from eq. 3.8; we set $a/\xi = 1$ and with various values of E, and with $\nu = 1/2$, we obtain

$$f = \begin{cases} 0.625\,\mathrm{pN}, & E = \ \ 5\mathrm{kPa} \\ 1.25\,\mathrm{pN}, & E = 10\mathrm{kPa} \\ 2.50\,\mathrm{pN}, & E = 20\mathrm{kPa} \end{cases} \tag{3.9}$$

With $E = 5\mathrm{kPa}$ and $a = 3\mathrm{nm}$, for example, we obtain $k = 6.28 \times 10^{-5}\,\mathrm{Nm}^{-1} = 6.28 \times 10^{-2}\,\mathrm{pNnm}^{-1}$. These numbers provide only a quite general, hopefully better than order of magnitude, perspective on the level of force generated within integrins.

3.3.2 Simulation model: general set up

The basic simulation model can be outlined using Fig. 3.4 where integrins in their three states are indicated. Note that here we assume a certain initial population of integrins and not that integrins are introduced in *pre-clusters*, say for example, from deposition from released integrin carrying vesicles [133, 134]. Un-activated and activated yet un-ligated integrins are considered mobile and freely diffuse within the membrane. Activated integrins,

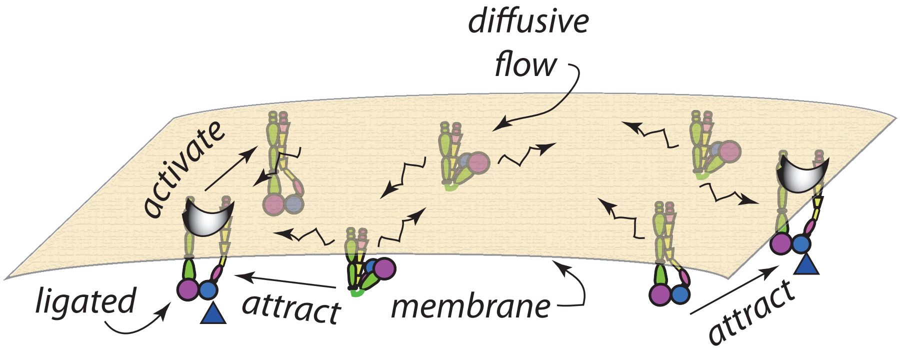

Figure 3.4. General set up for a diffusion based integrin clustering based on interactive integrins. Ligated integrins are relatively immobile, possessing very small diffusivity, whereas active yet unligated integrins are mobile, with finite diffusivity. Inactive integrins are mobile but do not interact with either ligated or unligated active integrins. The broken arrows indicate finite diffusiveness whereas the solid arrow indicates attractive interaction.

associated with kindlins and the THD, however interact with ligated integrins that are considered either immobile or of significantly reduced mobility. The attraction force is computed by eq. 3.7. Ligation of activated integrins occurs with a probability, that translates to a rate, that depends on the energy associated with achieving an indentation of $\delta^{\star}_{\alpha,\beta}$; we take this, as noted above, to be such that $\delta^{\star}_{\alpha,\beta} \approx 10$nm. But if ligation is to occur near an already ligated integrin, say integrin α, the additional indentation is reduced to $\delta^{\star}_{\ell} - \sum_{\{\eta\}} \delta_{\beta}(|\xi_{\alpha} - \xi_{\beta}|)$ where $\{\eta\}$ is the set of all activated integrins not including α; thus ligation is favored near an existing ligated integrin and clusters of ligated integrins. Note that the above schema does promote the incorporation of un-ligated, and particularly activated, integrins into clusters as suggested by Changede and Sheetz [64].

Let the set of all ligated integrins be called $\{\eta_{\ell}\}$, the set of activated but un-ligated integrins be $\{\eta_{u\ell}\}$, and the union be $\{\eta\} = \{\eta_{\ell}\} + \{\eta_{u\ell}\}$. The embedded body forces within integrins are determined as follows:

$$\begin{gathered}
\delta_{0,\alpha}(f_{\alpha}) + \sum_{\beta=\{\eta\}} \delta(|\xi_{\alpha} - \xi_{\beta}|, f_{\beta}) = \delta^{\star},\ \delta_{0,\alpha} \geq 0;\ \alpha \in \{\eta_{\ell}\} \\
\delta(0,\alpha) = \delta^{\star}_{u\ell},\ \alpha \in \{\eta_{u\ell}\} \text{ and then} \\
f_{\alpha} = k\delta_{0,\alpha},\ \alpha \in \{\eta_{\ell}\} + \{\eta_{u\ell}\}.
\end{gathered} \tag{3.10}$$

We note, for clarity, that for unligated integrins what is specified is a fixed $\delta^{\star}_{u\ell}$ and hence for an unligated integrin $f^{ul}_{\alpha} = k\delta^{\star}_{u\ell}$ regardless of the displacement fields of other integrins; *i.e.* unligated integrins simply cause a fixed indentation.

3.3.3 Simulation model: force mediated diffusion

For diffusive motion we take the mean square particle distance traveled, in time t, to be $\langle r^2 \rangle = 4Dt^{\gamma}$, where D defines a diffusion coefficient and, for free diffusion, $\gamma = 1$ [135]. For viscous motion, with velocity v, under an applied force we take a linear relation

$v = 1/\zeta\, f$; the Stokes-Einstein relation [135] provides the link, as

$$1/\zeta = D/kT. \tag{3.11}$$

We apply a general scheme to simulate particle diffusive-ballistic motion patterned after Brànka and Heyes [136]; here x_i, $i = 1,2$ are the 2D coordinates of particle, *i.e.* integrin, i.

To simulate 2D diffusion *per se*, we write that

$$\frac{dx_i}{dt} = \dot{x}_i = D^{1/2}\phi_i,\, i = 1,2 \text{ and with expectation } \langle \phi_i \rangle = 0. \tag{3.12}$$

Here ϕ_i is a random force that contains kT and $D^{1/2}$ as scaling factors, explained below. When eq. 3.12 is integrated over a short time (step) Δt we obtain

$$x_i = D^{1/2}\phi_i\,\Delta t,\, i = 1,2, \text{ with again } \langle \phi_i \rangle = 0. \tag{3.13}$$

Hence, we may take $x_i = W_i$, with $\langle W_i \rangle = 0$. But given that $\langle r^2 \rangle = \langle x_1^2 + x_2^2 \rangle = 4Dt$, we find

$$\langle W_i^2 \rangle = 2Dt,\ i = 1,2. \tag{3.14}$$

Now the general equations of motion read

$$\dot{x}_i = \frac{1}{\zeta} f^{(i)} + D^{1/2}\phi_i \tag{3.15}$$

and hence, using a Runge-Kutta order 2 integrator, we arrive at the explicit iteration

$$x_{i,n+1}^{(\alpha)} = x_{i,n}^{(\alpha)} + \frac{1}{2}\left\{\tilde{f}_i^{(\alpha)}(t_n, \mathrm{x}_n) + \tilde{f}_i^{(\alpha)}(t_{n+1}, \mathrm{x}_{n+1}^{\alpha,E})\right\} + W_i,\, i = 1,2,\, \alpha = \{\eta_a\}, \tag{3.16}$$

where $\tilde{f}_i^{(\alpha)} = 1/\zeta\, f_i^{(\alpha)}$ is the normalized i^{th} component for interaction force computed from eq. 3.7, when summed over all integrins that produce an elastic field and

$$\mathrm{x}_{i,n+1}^{\alpha,E} = \tilde{f}_{i,n}^{(\alpha)} \Delta t + W_i,\ i = 1,2 \tag{3.17}$$

is the "Euler" estimate of x_i at time $t_{n+1} = t_n + \Delta t$.

3.3.4 Ligation *vs.* bond rupture kinetics

We adopt a simple approach to describe the rate of ligation and ligation bond rupture, *viz.* we write that

$$k_{\text{on}} = k_{\text{on}}^0 e^{-\phi}, \tag{3.18}$$

where

$$\phi = \begin{cases} f\{\delta^\star - \bar{\delta}_\beta\}/kT, & \bar{\delta}_\beta \le \delta^\star \\ 0, & \bar{\delta}_\beta > \delta^\star, \end{cases} \quad \text{and} \tag{3.19}$$

f is the force that would develop within the integrin as it ligates; ligation involves 2 length scales, *viz.* $\delta^\star$ and $\bar{\delta}_\beta$. $\bar{\delta}_\beta$ is used here to denote the net displacement at the ligating integrin caused by the displacement fields of all other integrins - *i.e.* all that have such fields - and $\delta^\star$ is the total displacement required for ligation; $\bar{\delta}_\beta$ is given as

$$\bar{\delta}_\beta = \sum_{\beta = \{\eta\}_{\bar{\alpha}}} \delta_\beta, \text{ where} \tag{3.20}$$

$\{\eta\}_{\bar{\alpha}} = \{\eta_\ell\} + \{\eta_{ul}\} - \alpha$. To be sure, we have

$$f = k\{\delta^\star - \sum_{\beta = \{\eta\}_{\bar{\alpha}}} \delta_\beta\}. \tag{3.21}$$

This approach is equivalent to that adopted by, *e.g.* Sun *et al.* [112, 137] that followed the observations of Erdmann and Schwarz [138] who analyzed the effects of integrin-ligand separation on cluster formation and and stability. Both approaches leaned heavily on the *ad hoc* formalism of Bell [80,139]. Effectively, the approach assumes that the rate of ligation is mediated by an activation energy, $\Delta\mathcal{G}^{\ell}_{\text{act}}$, that depends on f, an internal force on the integrin that opposes integrin extension. This may be written as $\Delta\mathcal{G}^{\ell}_{\text{act}} = \Delta\mathcal{G}^{0,\ell}_{\text{act}} + \Delta\mathcal{G}^{\ell}_{\text{ext}}$, where $\Delta\mathcal{G}^{\ell}_{\text{ext}} \sim$ *work of extending the integrin, including deforming the cell membrane-glycocalyx-ECM system*; the latter is related to f and $\delta^{\star}$ as $\Delta\mathcal{G}^{\ell}_{\text{ext}} \sim \gamma f \delta^{\star}$, γ being determined by the particular model used to relate f to $\delta^{\star}$. Hence we arrive at eq. 3.18 with eq. 3.19. In this, $k^{0}_{on} = \mathcal{K}^{\circ}\exp\{-\mathcal{G}^{0,\ell}_{act}/kT\}$, and $\mathcal{G}^{0,\ell}_{ext}$ represents the additional work of extension involving the system stiffness; $\mathcal{K}^{\circ}$ is a kinetic pre-factor.

To rigorously describe the kinetics of bond rupture, *i.e.* unligation, we should account for the *catch-bond* nature of integrin-ligand bonding *via* computing bond survival times [140]; a particularly clear and implementable theory for this has been presented by Thomas *et al.* [79,141] and has been implemented for adhesion by Asaro *et al.* [142]. However, in simulations such as the ones we pursue here such an implementation would distract us from the salient points to be made in employing a matrix of parameter studies and would require detailed knowledge of data on catch-bond properties that are rarely available. Hence we take an alternate route to approximate this by drawing from the somewhat *ad hoc* formalism developed by Bell and co-workers [80,139]. Bell's formalism has, indeed been used in this context by others, *e.g.* [69,78,137,143]. Toward this end we write

$$k_{\text{off}} = k^{0}_{\text{off}} e^{\varphi}, \tag{3.22}$$

where

$$\varphi = \begin{cases} 3f/f_{\text{max}}, & \delta^{\star} - \delta \geq 0 \\ 0, & \delta^{\star} - \delta < 0 \end{cases} \tag{3.23}$$

and where $f_{\text{max}} = k\delta^{\star}$. This is often said to be a simple *slip-bond* whose rupture rate is monotonically increased by a force like f.

Integrin-ligand bonds are generally described using a two-state energy landscape as suggested by the two extended states for activated integrins sketched in Fig.3.2; specifically they are described as *catch-bonds* [79,140,141]. As noted above, we use a simpler description in the current case due to the quite limited range of force level imposed on the integrin-ligand bonds. Data for such kinetics, *e.g.* for k_{on}^0 and k_{off}^0 however, remains both elusive and disparate, since parameter values have been determined for various systems without the context of the present cell adhesion. We have chosen values that are reported, and used in analysis, by a range of studies [69, 78, 137, 138, 143–145] and tended to use median values that are listed with our case studies. Variations of these have been utilized to establish sensitivity.

3.3.5 Scaffolding proteins affect clustering: talin

Scaffolding proteins such as talin bind to integrins and promote activation and ligation as described *via* Figs. 3.1 and 3.2. In fact, Changede and Sheetz [63, 64] in their overview reports have proposed that [64] "*... the (talin) rod domain contains an integrin binding site 2(IBS2) required for clustering, which directly binds the activated β subunit of the integrin domain ...*" as sketched in Fig. 3.2e-d. We have included this into our modeling by specifying a probability of binding of talin rod (TR) to ligated integrins and, in turn, the binding of unligated integrins to integrin-talin complexes; such unligated integrins, with reduced mobility, are referred to as "unligated+tailin" in our subsequent example simulation figures. We take a simple approach to describing these effects of talin by noting first that binding of talin to an integrin, say an unligated integrin *via* a vinculin *catch-bond* [142] would most likely unjustified and hence a simpler approach is required to capture the main effects of restricted mobility due to both bonding and corralling effects of the scaffolding network. Hence we take the view that an unlighted integrin that migrates within a certain distance, r_{talin}, of a ligated integrin experiences a reduced mobility ascribed by $D_{\text{unligated-talin}}$; these reduced diffusion coefficients are listed in our case studies to follow, where r_{talin} is typically taken in the range $15\text{nm} \leq r_{\text{talin}} \leq 25\text{nm}$.

Hence in our simulations we allow such restricted integrins to move by diffusion and viscous drag albeit with reduced mobility; the effect is they are "encouraged to cluster", yet can move out and become free again, or they may ligate with enhanced probability due to the proximity of nearby ligated, and perhaps clustered, integrins. Our case studies illustrate ample examples of such choices.

3.4 Results

3.4.1 Effects of parameters

We begin with a few pointed observations concerning the anticipated effects of key parameters on potential clustering. Specifically, we comment on expected effects of integrin ligation distance, $\delta^{\star}_{\alpha,\beta}$, diffusion coefficient, D, and cell membrane-substrate stiffness, E. For $\delta^{\star}_{\alpha,\beta}$, hereafter simply referred to as $\delta^{\star}_{\ell}$, we first recall that the extensional distance of an activated integrin is of $\mathcal{O}(10-12\text{nm})$, hence $\delta^{\star} \geq 10\text{nm}$. On the other hand, integrins must extend beyond the cell's gycocalyx whose thickness is of $\mathcal{O}(10-60nm)$, or thicker [146–149]; hence in our simulations we explore the range $10\text{nm} \leq \delta^{\star}_{\ell} \leq 60\text{nm}$. For diffusion coefficients, we note that integrin diffusive mobility has been studied in a number of contexts related to adhesion, including those specifically related to clustering, *e.g.* [73, 150–152]; based on these reports, we may assume $10^{-15}\text{m}^2\text{s}^{-1} \leq D \leq 5 \times 10^{-13}\text{m}^2\text{s}^{-1}$; in our case studies, however, we take $D \leq 2 \times 10^{-14}\text{m}^2\text{s}^{-1}$. In a most interesting study of integrin mobility within FAs, Rossier *et al.* [152] reported variable diffusion coefficients for $\alpha_v\beta 3$ and $\alpha 5\beta 1$ integrins that depended on the state of confinement within the adhesion; integrins were defined as being "free" when they were outside FAs and unligated and "immobilized" when they were ligated and bound to actin binding proteins (ABSs) such as talin. For ligated and ABS bound integrins we generally take $D = D_{\ell\text{ig}} = 10^{-18}\text{m}^2\text{s}^{-1} - 10^{-16}\text{m}^2\text{s}^{-1}$ to make our model adaptable; with this low value, however, we confirmed that there were no perceptible differences than when simply assigning $D_{\ell\text{ig}} = 0$. For free integrins

Rossier *et al.* [152] report that $D_{\text{free}} \sim 7 \times 10^{-14} \text{m}^2\text{s}^{-1}$; we generally chose values between $D = 10^{-15}\text{m}^2\text{s}^{-1} - 2 \times 10^{-4}\text{m}^2\text{s}^{-1}$ to be more consistent with with a range of reports as already cited [73, 150–152]. In an exploratory simulation, presented in Section 3.4.2, we take $D = 10^{-17}\text{m}^2\text{s}^{-1}$ to consider a case of cells supported on supported lipid bilayers (SBLs) with mobile ligands that allowed for ligated integrin diffusion [63]. With this we anticipate and explore the following, *inter alia*, effects.

1. Ligation distance, $\delta^\star_{\alpha,\beta} \overset{generically}{\underset{called}{\rightsquigarrow}} \delta^\star_\ell$: As the force, f, within an integrin depends on $\delta^\star$, as does the integrin's displacement field, we expect this parameter to have a first order effect on integrin migration and ligation binding lifetime. These effects are, however, complex due to the cooperative nature of integrin interaction as well as the stochastic nature of integrin migration and ligation and un-ligation behavior. We further note that the interaction forces are related to combinations of terms such as $f\,\partial\delta/\partial\xi$ as in eq. 3.7, and as $f \sim E\,\delta^\star_\ell$ and $\partial\delta/\partial\xi \sim 1/E\,\delta^\star_\ell$, the interaction force between integrins may be expected to dominated by $\{\delta^\star_\ell\}^2$. However, as the internal force, f, depends on E, the rate of un-ligation will depend directly on stiffness E. Hence the effects of E, per se, are not easily anticipated *a priori*. For example, due to the attractive forces among the integrins we expect that increased mobilities will tend to reduce time scales for cluster formation and perhaps affect cluster size.

2. Integrin diffusion coefficient, D: Both the rate of diffusion and viscous motion depend on the magnitude of D since the viscous mobility, $1/\zeta$, and D are related as $1/\zeta = D/kT$. Hence we expect that D will have a first order effect in promoting clustering.

3. Cell membrane-substrate stiffness, E: The effect of stiffness has already been noted and we expect that its main effect will be in determining whether clusters are stable or not; this is expected due to the effect of large integrin internal forces on the rate of un-ligation, *i.e.* k_{off}. In terms of interaction force, the effect of E becomes more

difficult to anticipate in such a stochastic process as diffusion-interaction driven clustering. Hence, we might say "*we'll see what happens and try to rationalize after*".

For additional perspective on the meaning and value of the results to be discussed, we note that they will show the influence of specific system parameters that are not typically reported, or perhaps even known for a given cellular system where clusters have been observed. Hence, the value of models of this type is to point to those physical parameters that require documentation if analysis of clustering events is to be possible.

3.4.2 Simulation results

To begin, we recall the observations of Ye *et al.* [87] who reported that no "gross clustering" of integrins was observed in the absence of binding to ligands, this lack of ligation they achieved by incorporating $\alpha IIb\beta 3$ into liposomes with activation with the THD. To explore this, as mentioned in Section 3.2, we performed simulations that mimicked this case by simply precluding ligation, as if ligands were absent; Figure 3.5 displays some results in which we explore two levels of $\delta_{u\ell}$ and integrin mobility, *i.e.* D. Cases #1 and #3 of Fig. 3.5 specify $\delta^{\star}_{ul} = 1.6$nm and 3.2nm, respectively; this, in turn, sets $f^b_0 = 0.1pN$ and $0.2pN$, respectively. There is, evidently, little or no tendency towards forming clear distinct clusters despite the mutual pairwise attraction of these active but unligated integrins as described by eq. 3.7. We also increased D from $D = 10^{-15}\text{m}^2\text{s}^{-1}$ to $D = 2 \times 10^{-14}\text{m}^2\text{s}^{-1}$ to test the sensitivity to mobility and observed no discernable differences. Given the physical origins of the pre-force, f^b_0, and its relation to its "driver", $\delta^{\star}_{u\ell}$, we do not believe that larger values are physically relevant. Hence, these results appear to be consistent with both the observations of Ye *et al.* [87] and Changede and Sheetz [63, 64] regarding the need for, at least some, integrins to be ligated to form distinct nascent clusters.

The underlying reason for this trend lies simply in the relative balance of random "thermal forces" *vs.* the relatively weak attractive forces due to type of interaction. Close

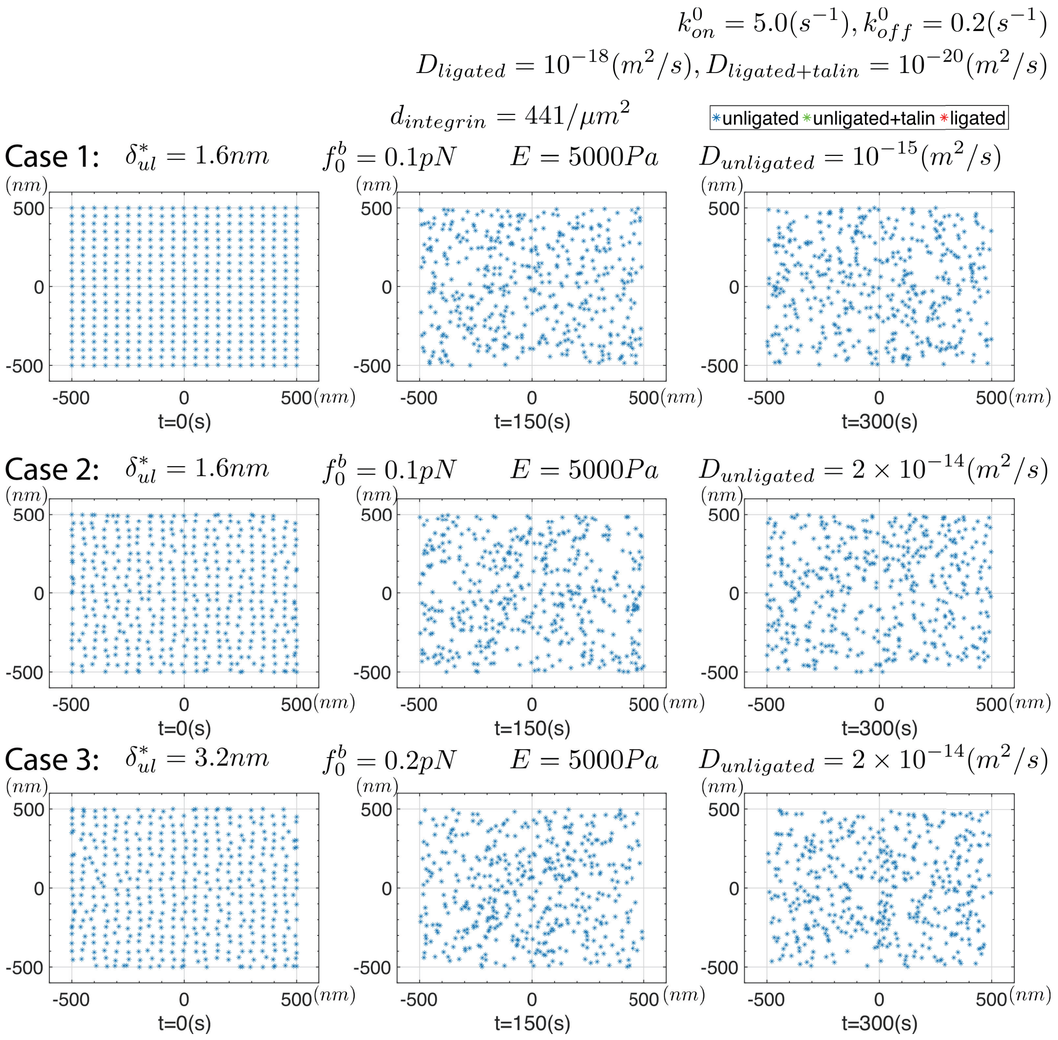

Figure 3.5. Results for a series of simulations where $\delta_{ul}^{\star} = 1.6$nm and 3.2nm for unligated integrins and in which ligation was precluded. Two levels of integrin mobility were used with $D = 10^{-15}\mathrm{m}^2\mathrm{s}^{-1}$ and $D = 2 \times 10^{-14}\mathrm{m}^2\mathrm{s}^{-1}$.

examination of the integrin distributions at longer times, however, reveals occasional loose, but transient, aggregations. These aggregates may be accentuated with increased $\delta_{\ell}^{\star}$, but as noted this would seem to suggest the need for additional experimental justification to motivate and justify even larger values of $\delta_{ul}^{\star}$; we recall from eq. 3.8 that, if $f_0^b = 0.1$pN, $\delta_{ul}^{\star} = f_0^b/k \sim 1.6$nm and so on with increasing values of f_0^b. For further perspective on this we again refer to the most interesting simulation studies of Reynwar *et al.* [128] who simulated large lipid membrane distortions caused by binding of protein capsids of various size and curvature.

Figure 3.6 summarizes results from a series of simulations in which we assume that unligated integrins do not create an elastic field, *i.e.* where $\delta_{ul}^{\star} = 0$; this means unligated integrins do not interact with the elastic fields of ligated integrins, *i.e.* they simply undergo random diffusion wherein they may ligate with enhanced rate if near a ligated integrin or cluster. All parameters are listed in the figure. Since the diffusion coefficient of ligated integrins is some 3 orders of magnitude less than that of active but un-ligated integrins, we expect that the only effect promoting clustering is the enhanced ligation rate, *i.e.* k_{on} of eq. 3.18. In all these simulations the initial distribution of integrins was taken as uniform with a density of $d_{\text{int}} = 441\mu\text{m}^2$.

Of the key parameters involved, we observe the influences of $\delta_{\ell}^{\star}, E$, and D. For example, for $E = 5000$Pa we observe that clusters do indeed form over times of $\mathcal{O}(1-2\text{min})$ and tend to remain stable as long as $\delta^{\star} < 30$nm; for $\delta^{\star} > 30$nm stable clusters do not survive. This was the case with $D = 10^{-15}\text{m}^2\text{s}^{-1}$. Yet, and again with $\delta_{\ell}^{\star} = 40$nm and $D = 10^{-15}\text{m}^2\text{s}^{-1}$, but with $E = 1500$Pa, we once again find observe stable clustering. We note, however, that the clusters tend to be rather small and contain but a few integrins; typically we observe on order of 5-7 integrins in all of the clusters shown in Fig. 3.6 with the initial density of $d_{\text{int}} = 441\mu\text{m}^2$. Hence clusters do form on substrates of all rigidity as Changede and Sheetz report [63, 64], at least within the range of E, D, and $\delta_{\ell}^{\star}$ we use here; clusters do tend, however, to be less stable on more rigid substrates. Changede *et al.* [63]

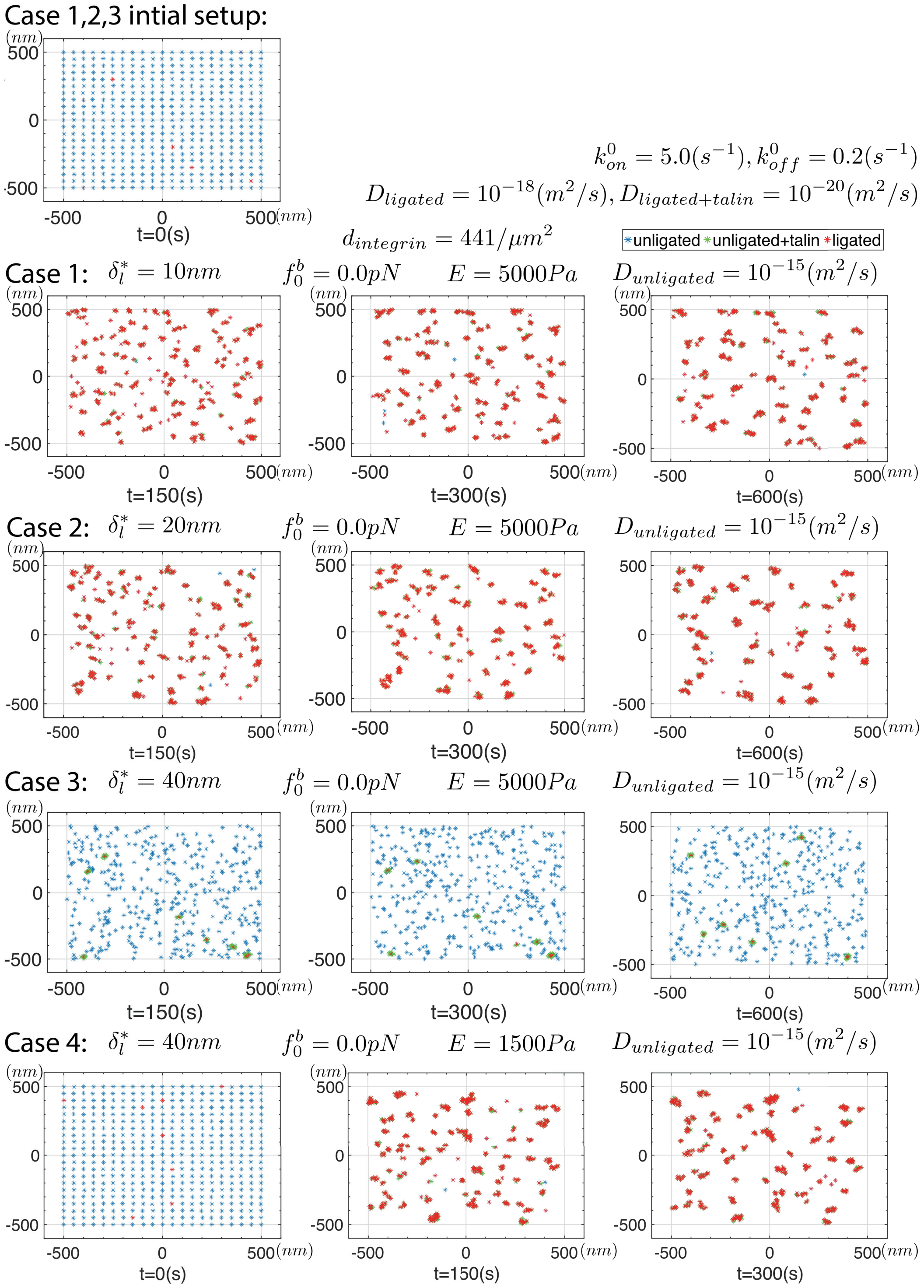

Figure 3.6. Results for a series of simulations where $\delta_{ul} = 0$ for unligated integrins; the frames are snapshots of a continuous simulation for greater that 600s. All parameters are listed for the 4 cases considered. The initial integrin distribution is is shown in the upper left.

noted that nascent clusters tended to be less persistent on stiff, *viz.* glass, substrates than on less rigid, *viz.* supported lipid bilayer (SLB), substrates, an observation consistent with the observations of Choi *et al.* [71]. Our observations of the effect of stiffness may provide the beginnings of an understanding of how that transient process unfolds. Changede *et al.* [63] suggest, though, that "... *the turnover of the adhesions was a second step that was stimulated by extracellular traction force*", a step we do yet include in our simulations. Choi *et al.* [71] discuss that nascent adhesion turnover is "... independent of myosin II", and hence this process will require further study. The clusters so far discussed in our simulations do tend to be smaller than they report and that requires further inquiry as we look to next.

Figure 3.7 shows results for a compatible set of cases as Fig. 3.6 where a pre-force is assumed as described above. As it happens, the differences are not great except for the observation that the clusters are sightly larger and tend to contain slightly more integrins on order of 6-8. One observation relevant to reported observations, is that there are now more unligated integrins found within the clusters; this is in addition to the also consistent increased size and cluster integrin density. Although the pre-forces, f_0^b, are of quite modest magnitude we find they do have noticeable effects such as increased cluster size and integrin number density within clusters. Since the displacement fields of an unligated integrin does contribute to the net required displacement beneath a ligated integrin, we expect their proximity to ligated integrins reduces the internal force and helps stabilize the ligation bond; recall that bond is considered a "slip-bond", not a "catch-bond". This effects is, however, quite modest and at the rather modest level of the internal forces of $\mathcal{O}(\sim 1\text{pN})$, or less, the bond type difference is itself modest. We note in passing, though, that the difference in bond type would be important when the actin-myosin cytoskeleton forces are applied as in mature FAs [79, 142]. Regarding stable clusters, here again we observe that when $\delta_\ell^\star > 30$nm stable clusters are not observed. A quite different picture is obtained, however, if the the integrin mobility is somewhat larger; we turn attention to the effect of mobility next in Fig. 3.8.

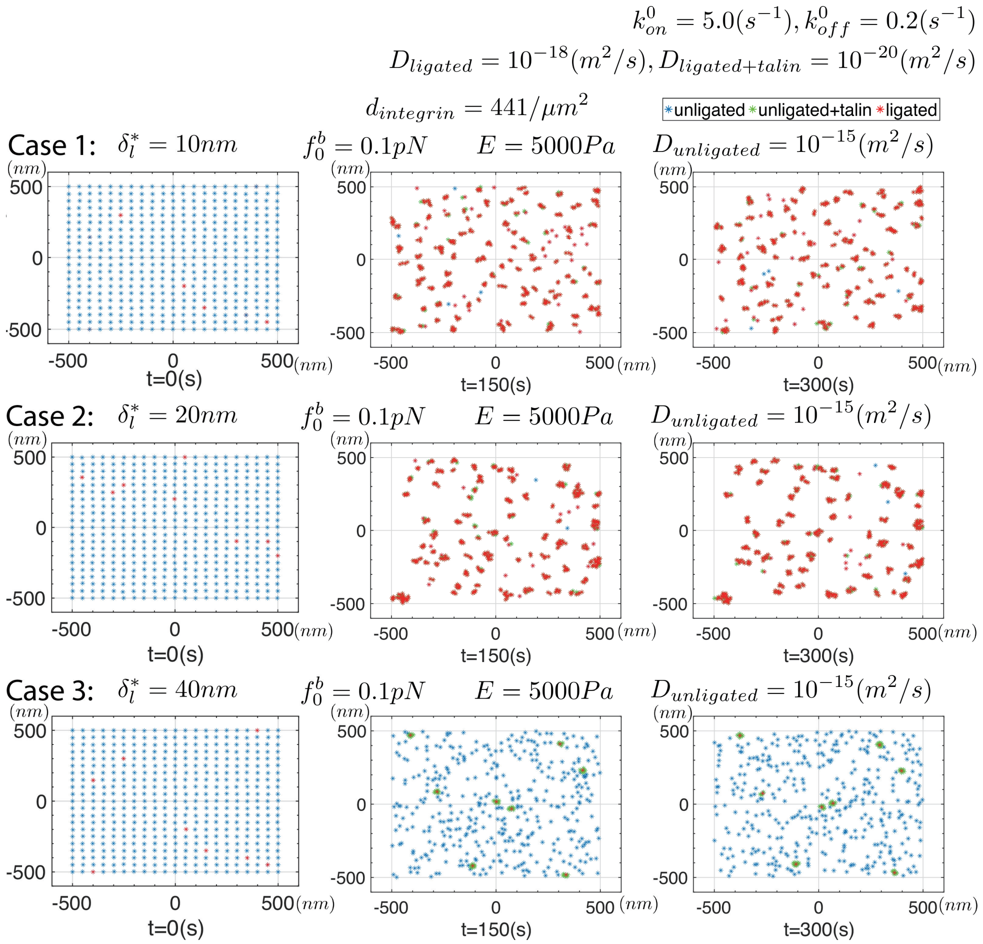

Figure 3.7. Snapshots taken from simulations in which a pre-force, f_0^b, is imposed on unligated integrins. All parameters are listed for each of the 3 cases considered. The initial integrin distribution is as shown in Fig. 3.6.

In Fig. 3.8 we explore the effects of a larger integrin mobility and, as it happens, increased integrin mobility appears to have substantial effects with respect to both the time scales for initial clustering and longer time clustering. With $D = 2 \times 10^{-14}\mathrm{m}^2\mathrm{s}^{-1}$, for instance, we note that aggregation of integrins appear only after times ~ 10s as opposed to ~ 300s when $D = 10^{-15}\mathrm{m}^2\mathrm{s}^{-1}$. It is important to recall that this acceleration is not merely the effect of diffusion *per se*, but of an increase in viscous mobility, $1/\zeta = D/kT$. Cluster size is also increased, with the number of clusters decreased and the number of integrins found within clusters increased.

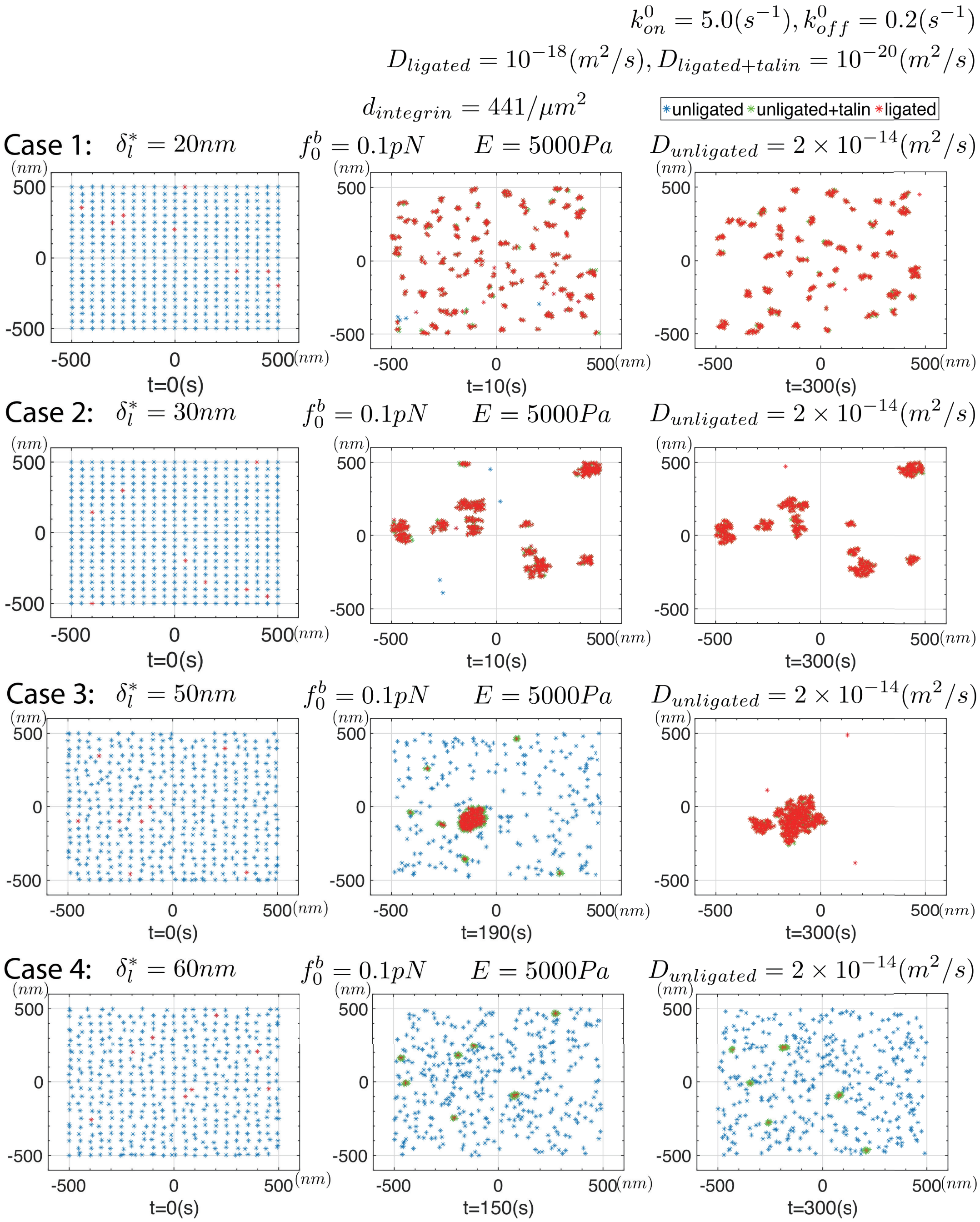

Figure 3.8. Snapshots of simulations for 4 cases in which the integrin mobility is increased to $D = 2 \times 10^{-14} \mathrm{m}^2\mathrm{s}^{-1}$. Note the significant effect increased mobility has on increasing cluster size while maintaining cluster stability.

Cases #2 and #3 of Fig. 3.8 are particularly interesting in that they display a reduced number of clusters whose sizes are significantly larger than appears in the simulations shown above. This effect with enhanced integrin mobility has its roots in one of the basic features of our model. Essentially, an explanation would go something like this. Once initial integrins ligate, they more quickly attract unligated integrins and also provide significantly higher probability of ligation in their vicinity, that is in the vicinity of a *de novo* nascent cluster. Hence, the *de novo* cluster develops rapidly. Its stability is assured due to the cooperation among displacement fields of the integrins such that only quite modest internal forces develop in each integrin within the cluster, *i.e.* k_{off} is maintained at a low level. When $\delta_\ell^\star$ is high enough, *e.g.* when $\delta_\ell^\star = 80$nm in this case, this is no longer the case.

Taken together, the above results demonstrate that the proposed mechanisms do naturally lead to integrin clustering with time scales consistent with reported observations. However, the details such as cluster size, and the number of integrins found within each typical cluster, depend on factors such as internal force levels within integrins, integrin mobility, and to a lesser extent system stiffness *per se.* These insights certainly suggest that further quantitative detail is required regarding integrin mobility as well as an assessment of *system stiffness*, *e.g.* what is taken as E herein. System stiffness, moreover, needs to be viewed in a more holistic manner, e.g. to include at least some assessment of the potential contributions of the cell's glycocalyx [78, 142]. To gain additional insight we refer to Fig. 3.9 that shows cluster results for systems of nominally higher integrin density, *viz.* $d_{\text{int}} = 841\mu m^{-2}$.

Figure 3.9 shows results for two cases, both with $d_{\text{int}} = 841\mu m^{-2}$, $\delta_\ell^\star = 20nm$, and $E = 5000Pa$, but with $D = 10^{-15}\text{m}^2\text{s}^{-1}$ and $D = 2 \times 10^{-14}\text{m}^2\text{s}^{-1}$. The most obvious, and perhaps expected, result is a general increase in the size and expected number density of integrins per cluster; cluster size is of $\mathcal{O}(100\text{nm})$, most particulary with $D = 2 \times 10^{-14}\text{m}^2\text{s}^{-1}$, *i.e.* higher integrin mobility. The number density of integrins is in the range of 30-50 integrins per cluster. We note that to approach such cluster sizes with lower d_{int}, larger $\delta_\ell^\star$ was required as in cases #1 and #2 of Fig. 3.8 showed. The general trends in cluster formation were not altered with increases in d_{int} but clusters appeared at earlier times

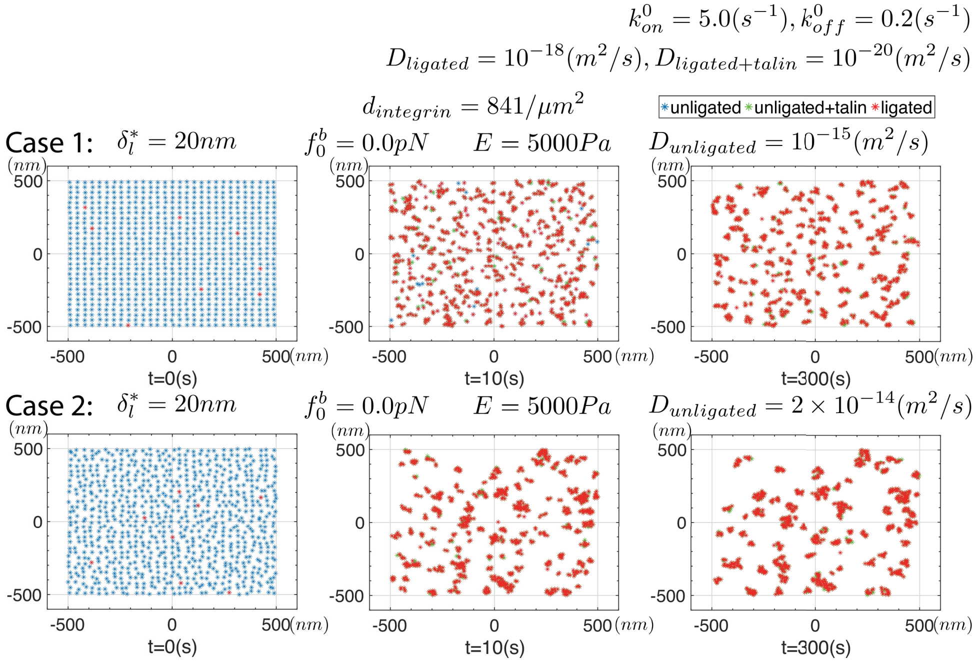

Figure 3.9. Simulations involving higher initial integrin density and modest integrin mobility (Case #1) and increased mobility (Case #2). Note the increase in cluster size and average integrin numbers within clusters with enhance mobility.

which, of course, would be expected. A most notable effects of $\delta^\star_\ell$ was to increase the eventual stable cluster size, which formed after ~ 100s, and that appears in the range $d_{\text{cl}} = 100 \pm 20$nm, as determined from range of 20 such simulations.

Cluster-cluster interaction

As a final example we address the question of cluster-cluster interactions; for this we refer to Fig. 3.10. Here we assume that ligated integrins may possess higher mobility, this motivated by Changede and Sheetz's [63] report that clusters on supported lipid bilayers (SLBs) tend to aggregate. How ligated integrins on an ECM diffuse, however, is unclear yet on the SBLs they used ligands were reported to be mobile. The effect of increasing D_ℓ, and in fact the effect of allowing mobility of ligated integrins at all, is sigificant indeed. In Case # 1 of Fig. 3.10, with $\delta^\star_\ell = 30$nm, we observe very early clusters that take on sizes $\sim 100 - 200$nm and rapidly recruit unligated integrins that ligate with enhanced rate. We do recall however that, since the internal forces within "would be" ligated integrins are modestly reduced, the effect of large clusters is to increase k_{on} toward the value k^0_{on} in eq. 3.18. The clusters are quite dynamic in that ligated integrins tend to unligate and re-ligate, unless they should diffuse away unligated; in this particular simulation if an integrin unligates we reset $D_{ul} = 2 \times 10^{-14}\text{m}^2\text{s}^{-1}$ and indeed we observe such occasional motions as described just below. Rossier *et al's.* [152] findings on integrin mobility might suggest a refinement of this by noting that if an integrin unligates while within a cluster's interior it may find itself "corralled" and hence less mobile; such refinements are readily accommodated, yet were not here.

The dynamics of the clusters is such that they tend to drift toward each other as noted by Changede and Sheetz [63], at least for those clusters whose integrins are bound by talin rod (TR). This drifting motion, however, occurs not by a discrete motion of clusters *per se*. Motion occurs by the slow ligation at those regions on the periphery of clusters juxtaposing nearby clusters. The simple scenario of this simulation evolves into a single cluster.

We then reduced $D_\ell = 10^{-17}\text{m}^2\text{s}^{-1}$ and observed a similar yet temporally different evolution of clusters that first formed and then drifted toward each other; this is shown in Fig. 3.10 as Case #2. Note that after 300s the clusters have "grown" by merging to sizes of $\mathcal{O}(200-300\text{nm})$. These clusters drift, typically toward each other, as described below.

To obtain a more detailed look at such cluster dynamics we performed additional simulations with the same parameters of Case #2 of Fig. 3.10 and extracted snapshots at time intervals of $\delta t = 0.1$s; an example is shown with Case # 2 of Fig. 3.10. This cluster, that contains at various moments within the $3\delta t$ time interval shown approximately 35-37 integrins, is drifting *dextra* (toward the right) in this scenario. The mechanism of motion can be seen by the movement of integrin "i", *sinister* (to the left) to the cluster where it becomes bound to the cluster *via* talin (see figure legends); integrin "i" is expected to then ligate, at least with a higher probability. In addition, we observe at least two examples of transitions in state of integrins "j" and "k" between the time $3\delta t$ between $t = 21.7$s

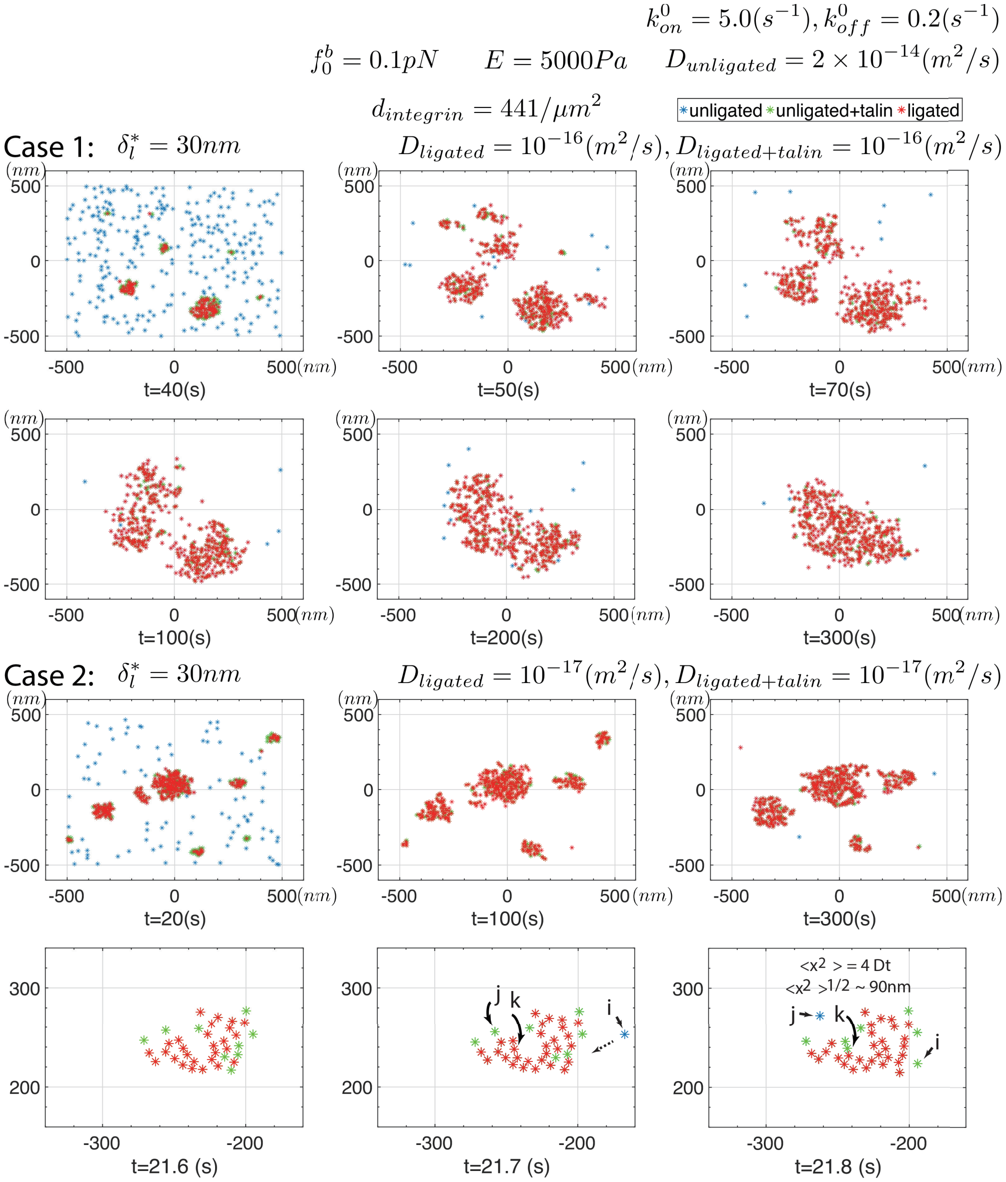

Figure 3.10. Simulation of nascent cluster interaction visualized by prescribing an enhance mobility to ligated integrins. All parameters are listed. Clusters tend to attack due similar force fields as described for individual ligated and activated integrins. Case #2 details cluster drifting and the dynamics of cluster motion and integrin turnover within a cluster.

and $t = 21.8$s. Integrin “j” has transitioned from being bound to a ligated integrin *via* talin to a ligated integrin on the left edge of the cluster to being unligated (*i.e.* free); this is part of the cluster’s drifting *dextra*. In the meantime integrin “k”, that is within the cluster, transitions from being ligated and unligated. It is indeed possible to turnover large fractions of ligated integrins within a cluster in this manner. Such visualizations also make it clear how further refinements in specifying character or parameters changes of integrins may be readily accommodated.

With regard to cluster drifting, however, we note that Changede and Sheetz [63] have reported that in cells expressing either talin head domain (THD) or the talin rod (TR) the motility is different; mechanisms for such differences remain to be explained. What also remains to be described is how nascent clusters de-stabilize, disassemble, and disappear.

3.5 Discussion

We have presented a framework, and a specific model, for the formation of nascent adhesions based on reported phenomenology, as cited, and a rather simple physical description of integrin bonding, *via* ligation, to substrates. Substrates, in our view, do not necessarily mean stiff media such as extracellular matrices or organic slides, but may indeed be soft matter such as supported lipid bilayers (SLBs) as described and used by Changede and Sheetz [63, 64]; the cell's membrane itself has finite bending stiffness. The idea behind our approach is also to be found in in the molecular dynamics simulation studies of, for example, Reynar *et al.* [128, 129] who demonstrated that capsid-like protein "particles", bound to lipid membranes, cause local membrane deformations that drive clustering, more intense deformations, and that may even lead to vesicle formation. The fundamental driving forces here are similar, namely the reduction in total free energy upon clustering of those entities, *viz.* protein capsids in Reynar *et al.* [128, 129], and integrins herein, that are the so-called *sources of deformation.* We note that the simulations of Reynar *et al.* [128, 129] of interacting proteins were preformed on free membranes that tended to take on large curvatures; in fact our mechanisms and formalisms is quite applicable to such curvatures. The cell-substrate interactions modeled in this study, however, occur on interfaces of quite modest curvature as affected by the protein distortions we model.

Our model also specifically calls attention to the role of the cell's glycocalyx, a feature that has been discussed by Paszek *et al.* [69, 78] with regard to cancer cells; this important, and ubiquitous, cell component is, unfortunately, to often neglected in such studies of cell adhesion. Hence, the discussion of Paszek *et al.* [69, 78] should receive more attention and has been, *e.g.* in the considerations of Asaro *et al.* [142] in describing the formation of traction force in FAs.

The framework of our model allows, by design, wide flexibility with regard to including additional features such as, *inter alia*: 1) patterned ligand distributions; 2) variable integrin mobility; 3) kinetic descriptions of ligation and unligating; and 4) the influence of "applied forces" as may arise due to actin-myosin contractility; by simply extending the model to include actin-myosin forces, the evolution of mature may be explored. Of course, this will entail a holistic treatment of the stochastic nature of the adhesome's force train as considered by Asaro *et al.* [142]; in that analysis they showed how mechanosensitivity occurred all along the adhesome and hence attempts to attribute such to a simple anonymous set of "clutch bonds" is inappropriate and unrealistic.

Our analysis has revealed several noteworthy features of the clustering process, yet there are many unknowns, as expected. These findings include, *inter alia:*

1. We have demonstrated that nascent clusters should form on substrates of all rigidities, a claim made in the title of Changede and Sheetz [63, 64]. This basis for their finding becomes clear upon the realization that a driving force for clustering stems from the energy reductions that follow clustering as illustrated by attractive pairwise force between integrins given in, *e.g.* eq. 3.7. As noted earlier, this force scales directly with terms such as $f^\star_\alpha \partial\delta/\partial\xi$ where $f^\star_\alpha$ and $\partial\delta/\partial\xi$, respectively, scale as E and $1/E$, E being the system rigidity (stiffness). Hence, the this force does not depend strongly on system rigidity; the internal force within an integrin, however, does depend on

system rigidity and that will affect ligation bond survival time. Of course, this basis may also be appreciated by the simulations of Reynar *et al.* [128, 129] noted above; in those cases there was no substrate, but only the free energy of the deformed membrane.

2. Our simulations reveal important quantitative and qualitative effects of integrin mobility, on clustering as illustrated in Fig. 3.10, and by comparing Figs. 3.10 with Fig. 3.9, as examples. First, we observe that clusters tend to be larger when the mobility of unligated integrins is increased; in the specific case studies clusters were in the size range ~ 100nm (in Fig. 3.9) and with a factor of 5 increase in $D_{\text{unligated}}$ were more in the range of ~ 200nm (in Fig. 3.10) in diameter. Moreover, if ligated integrins were ascribed a somewhat increased mobility, clusters were observed to “drift” so that they aggregated. To visualize why this may happen, we noted that clusters that stand apart by some distance from each other appear as “large point forces” and hence attract with a force similar in kind to that described by eq. 3.7 for single integrin pairs; this is the thermodynamic force driving the drifting motion. The actual mechanism for this drifting involves integrin unligation and ligation at the juxtaposed peripheries of merging clusters as illustrated in the simulation frames shown for Case #2 of Fig. 3.10. But the question arises: what accounts for this enhanced mobility of ligated integrins? In the cases studied by Changede and Sheetz [63], involving cells on supported bilipid layers (SBLs), they reported that the ligands on SBLs were mobile. For cells adhered to an ECM or an organic substrate this would remain an open question. Nonetheless, if clusters are observed to aggregate, this offers a potential mechanism. Clearly, this sort of observation, among others, suggests that integrin mobility is an important determinant for deciphering cluster dynamics and hence experimental studies of clustering will be deficient without such information.

3. On the question of integrin mobility we note the study of Rossier *et al.* [152] as a noteworthy example. Their study was particularly concerned with understanding the role of, in particular β_1 and β_3 containing, integrins dynamics on FAs in fibroblasts on fibronectin substrates. We have used these studies to motivate our variations in diffusion coefficient as explained in our case studies above. Accordingly, we "immobilize" integrins upon ligation where we have assumed that the integrins bind talin, and possibly kindlins as well; this is done by assigning a nearly vanishingly small value of $D_{\text{ligated}} \sim 10^{-18}\text{m}^2\text{s}^{-1}$. Rossier *et al.* [152] defined integrin confinement within FAs in terms of a radius, r_{conf}, and with that specified diffusion coefficients accordingly. This sort of detail may be incorporated into a model such as ours for further refinement.

4. Finally we add that our model helps explain the patterns of integrin clustering observed in the experiments we have cited, *e.g.* [63, 64, 71], that are some of the most comprehensive conducted to date. In particular, we find that the numbers of integrins that appear in clusters appears to lie in the range of 30-50 which is again typical to what is observed experimentally [63, 64]; this in itself is a noteworthy and not obvious trend. However we also note that depending on factors such as the initial density of integrins and the magnitude of diffusion coefficients numbers outside this range are indeed possible. For this reason we have made special note that future studies of nascent clustering should document the mobility of integrins as well as their expressed numbers.

Further progress may be made by combining the sort of detailed observations of nascent cluster formation as reported by Changede and Sheetz [63, 64] with a more holistic study of integrin mobility as performed by Rossier *et al.* [152]; this would provide a better documented case study to explore the veracity of models of the type we have presented herein. Cellular details pertaining to cell glycocalyx as well as integrin activation kinetics for the identified adhesion integrin-ligand system would, of course, be invaluable. Without such a quantitative basis, models can only render trends and potentialities, not true forecasts or explanations. In fact, the immediate value of models such as presented here is to better define what is needed and why it is needed.

Finally, we suggest that a particularly important feature (mystery?) of nascent cluster adhesions is their disassembly, *i.e.* if they fail to mature into FAs. This process may lie at the heart of our eventual understanding of cell adhesion, mechanosensitivity, and mechanotransduction. Once the disassembly process has been better understood in a mechanistic sense, other critical details such as the stochastic, force rate, and time dependent traction forces that develop due to cytoskeleton contractility may also be better understood in a modeling sense, *e.g.* [137,138,142,143]. The same is true for vital processes such as cell migration which involves both adhesion formation and disassembly.

Acknowledgement

Chapter 3, in part is currently being prepared for submission for publication of the material. Lin, Kuan-Po; Asaro, Robert. The dissertation author was the primary investigator and author of this material.

Chapter 4

Diffusion-advection within dynamic biological gaps driven by structural motion

4.1 Introuduction

Examples are legion of biological systems in which an exchange of solute and/or solvent across or along the walls of channels or thin gaps, through which fluid solution flows, occurs. This, of course, suggests that advection coupled to diffusion may play an important role in the overall transport. Indeed, this underlies a basis of Starling's hypothesis [153], of over a century ago, that fluid is filtered at the arterial end of a vessel such as a lymphatic vessel, and reabsorbed at the venous end through fluid flow. Advection influences have been assessed within the framework of the *standard gradient* model for water transport, *inter alia* [154,155]. Other examples are found within the Golgi complex, within channels of epithelial cells, and in the thin gaps between cells during their adhesion. Advective flow of potentially toxic metabolic by-products within the brain has been recently discussed [156]; the concepts proposed there are similar in part to Starling's idea. In the brain, this is thought to occur *via* the interstitial space and fluid and although detailed models for this and the energetic sources that drive the process may be yet unknown, evidence for advection *vs.* diffusion is compelling [156]. Combined diffusion and advection occurring within the interstitial space of tissue has been experimentally explored since at least 1989. For example, Chary and Jain [157] measured the transport of bovine serum albumin within chambers implanted in the ears of rabbits. In such cases of larger molecules, experimentally measured diffusion coefficients of order $D \sim 10^{-11}\text{m}^2\text{s}^{-1}$ indeed showed that advection contributed a vital role in the overall transport. For later reference, we note that Chary and Jain [157] reported measured fluid velocities in the range $v \sim 0.5 - 0.6\mu\text{m s}^{-1}$; such velocity range will be referred to below and quite favorably compared to our model's forecasted ranges, say $v \sim 0.5 - 1.0\mu\text{ms}^{-1}$ (see Section 4.3.3, eq. 4.34 and then Section 4.3.1, eq. 4.13).

These combinations of diffusion coefficient and fluid velocity values demonstrate a definite contribution of advection. To explore this we consider the example of possible advection coupled to diffusion in the transport of neurotransporters within a synaptic cleft-like geometry (aka gap) of nerve dendrites [158, 159]. Advection within the synaptic cleft might not be thought as a major contribution to molecular transport due to its restricted transport distances $200\text{nm} \lesssim R \lesssim 1000\text{nm}$, yet it provides a quite clear geometry (Fig. 4.1) to explain the effects of structural motion that reveals an inverse effect of length scale on transport. For example, with $D \sim 10^{-11}\text{m}^2\text{s}^{-1}, R \sim 1\mu\text{m}$, and $v \sim 5\mu\text{ms}^{-1}$ we find a Peclet number $\mathcal{P}_e \sim Ru/D \sim 0.5$ which about brings advection about competitive with diffusion. We explore, however, a vital link between length scale with $\mathcal{P}_e$ within our models *via* predicted fluid-solid interaction; this links length scale with v in an inverse relation. In fact, we introduce a number, $\mathcal{A}^D$, that compares time scales for advection *vs.* diffusion and find $\mathcal{A}^D \sim 1/R^2$. This unexpected result for the effect of diffusion distance is due to the strong R^4 dependence of hydrodynamic resistance of our model rigid disc.

Of course, the fluid flow considered herein does not compare with that found in *cytoplasmic streaming* in plants discovered over 240 yrs ago [160, 161]. Recent reviews [162, 163] discuss fluid velocities well in the range of $v \sim 1 - 10\mu\text{ms}^{-1}$, and even as high as $40 - 60\mu\text{ms}^{-1}$ [164, 165]. The flow is driven by the motion of myosin motor proteins along actin filaments that carry "cargo" consisting, *inter alia*, of vesicles, organelles, and molecular complexes. This, in turn, provides a velocity boundary condition that sets fluid flow patterns throughout the bulk of the cytosol and vacuoles of the plant cell. As Pickard [161] pointed out, however, it may not be the advection of fluid fluid flow *per se* that is responsible for the more critical transport but the "towing" *via* the myosin carriers of vital entities. Two aspects of cytoplasmic streaming in plants are worth noting here, however. First, the ranges of fluid velocities involved suggest a clear potential for significant contributions of advection *vis-à-vis* diffusion for molecular transport, especially over distances $L \geq 1\mu$; indeed this has provided perspective on the limits to animal cell size, as opposed to larger plant cell sizes, if it is assumed that diffusion *per se* is the most viable mode of ion and molecular transport in animal cells [162]. Secondly, is the role of ATP hydrolysis that powers cytoplasmic streaming [162, 163]. We will likewise assume that ATP hydrolysis is necessary to achieve sufficient hydrodynamic flow to render advection significant.

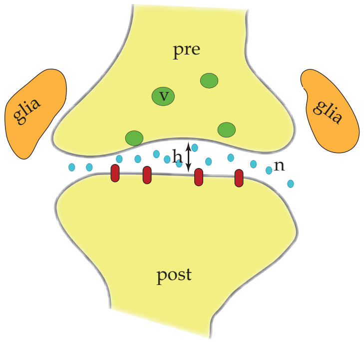

Figure 4.1. Schematic of pre- and post-synapses separated by a synaptic cleft (aka "gap") of width h. Also indicated are synaptic vesciles that release glutamate into the cleft. Note that the synapse has a glial cell sheath that is not explicitly included in our model.

As it happens, in biological systems fluid flow is often described as random flow since it is driven by thermal fluctuations; hence the advection flow of solutes within the fluid solutions is a stochastic process. Advection-diffusion precesses have been the subject of various studies in a general context and it has been shown that under certain circumstances advection can indeed have a significant role as compared to diffusion *per se* [166, 167]. Recent experimental evidence has, in fact, been analyzed and reported for stochastic advective transport lysomes in motile neutrophil-like cells coupled to diffusion [168]. In this interesting case the contributions of diffusion *vs.* stochastically driven advection were separately identified *via* the characteristically different time dependence of particle trajectories. Advection due to the stochastic fluid motion driven by the shape changes that occurred during the cell's crawling motion was indeed notable with fitted diffusion coefficients of the order of $D \sim 10^{-14}\mathrm{m}^2\mathrm{s}^{-1}$. This result is consistent with our forecasted results as noted at the end in Section 4.5. We indeed explore the advection-diffusion coupling during random flow within the basic structure of the synapse cleft. This is to serve as a prototypical case study whose insights should pertain to a wide range of scenarios.

Transport has been analyzed within the synaptic gap [159]- [169]; such studies have focused on events such as *spillover* [170, 171]. For a complete description of the transient distribution of neurotransmitters after release within a geometry such as the synaptic gap account must be taken of the glial cell coverage around the synapse that may impede extracellular diffusion. Such refinement is not included here where we use a simple boundary condition at the synapse perimeter. Direct observation of the transient transmitter concentration profile has proved elusive and hence reliance on theoretical modeling has been used for forecasts. To date modeling has been concerned with analyzing diffusion as the only transport mechanism - clearly this is reasonable since published values for the diffusion coefficients [158, 169] would argue for such diffusion general dominance. However, the influence of advection coupled to diffusion has yet to be explored.

The aim here is to formulate a simple, credible, model for the advection-diffusion process of transport of glutamate or other molecules within the synaptic cleft, or a cleft-like geometry, wherein the various physical features, and individual sub-processes, are well defined and such that each displays a clear role in controlling the overall process. As it happens, there are parameters linked to particular features that control the time scales of advection *vs.* diffusion, and on the other hand parameters that determine the potential magnitude of the advection contribution. The latter parameter is dependent on the energetics driving synaptic motion that causes fluid motion either due to thermal fluctuations and possible metabolic energy sources, *e.g.* ATP hydrolysis. This is discussed in some detail in Section 4.4.1. Thus a main purpose of the model analysis presented herein is to provide a clear model scenario for what determines the role of advection driven by structural motion.

4.2 Problem description

The essential geometry of the model, and the boundary value problem, is illustrated in Fig. 4.2. A neuron(nu) is located above a dendrite(den) at the instantaneous height $h(t)$. The neuron is modeled as a rigid disc of radius R and of mass m. The neuron is in thermal motion, in the z direction, relative to the dendrite as modeled in the next section. The motion is random, composed of white noise *via* thermal fluctuations and possible additional metabolic energy input. However, for comparison we shall also consider deterministic motions including harmonic motion. So much for the geometry. We will assume, as detailed below, that the geometry in which $h/R \ll 1$ allows for a thin film approximation so that concentrations as well as fluid flow can be thought of as $z-$ averaged, or resultant quantities.

At time $t = 0$, a flood of neurotransmitters is ejected into the synapse gap creating an initial concentration, $c(r,0) = c_0$; the concentration of neurotransmitters outside the gap is zero. One simple boundary condition to account for this is to set $c(R,t) = 0$. For the synapse such a boundary condition may arise *via* the absorption of neurotransmitters by the glial cells located at the periphery of the cleft (Fig. 4.1 and [170]). This sort of model does require further discussion, however, as given below.

To model the motion of the disc above its substrate, we couple it *via* a linear spring

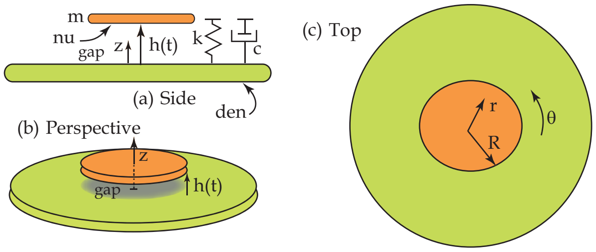

Figure 4.2. The synapse is modeled as a disc (nu) oscillating above a fixed half-plane (den) and restrained by a linear spring (k) and subject to a linear viscous drag (c). See also Fig. 4.3 and its associated discussion for additional detail. Figure 4.5 shows an alternative model involving two opposing discs; the associated discussion explains that these two models are essentially equivalent.

representing a harmonic potential and a damper that is meant to account for viscous frictional resistance of the surrounding fluid. This is depicted in Fig. 4.2a, the side view of the system.

The idea is this: the motion of the disc induces a Stokes fluid flow field whose through thickness average radial component takes the form,

$$\bar{v}_r = -\frac{1}{2h}\frac{\mathrm{d}h}{\mathrm{d}t}r. \tag{4.1}$$

As $\mathrm{d}h/\mathrm{d}t$ oscillates in sign, fluid flows out of and into the gap carrying solute *via* both diffusion and advection. When fluid flows out of the gap, which is at higher concentration, the concentration outside is increased, whereas when fluid flows into the gap its concentration is lower than c_0. One may expect that the net effect is to reduce the gap concentration *via* advection. Of course, diffusion will also have the effect of reducing the gap concentration as well. The effect of advection may then be an enhancement of solute transport. However, this will be dependent on the temporal pattern of the fluid flow as created by the disc's motion. For example, recall that the assumed well ordered Stoke's flow is *reversible* (*e.g.* [172–174]). Hence, if the disc's motion is, say harmonic, then the advection effects will vanish since the same volume elements of fluid with their solute will be reversibly transferred into and out of the gap over a period of motion. In such cases mixing of solute occurs only *via* diffusion. Indeed, this is similar to a simple particle random walk or to Brownian particle motion whereby unbiased random jumps lead to a time average distance, r, traveled $\langle r \rangle = 0$ (hereby $\langle . \rangle$ refers to average in time) yet to a mean square distance $\langle r^2 \rangle \propto t$. As shown in Sections 4.3.2 and 4.3.3 if $h(t) = h_0 + \eta(t)$ where $\eta(t)$ is a random motion about a mean gap width h_0, the time average $\langle d\eta^2/dt \rangle$ controls the time average of advective flow. Hence our case of a stochastically driven flow field is not a case of a smooth reversible flow. As particles in a stochastic Brownian motion are subject to randomly imposed forces, solute particles here are subject to a randomly imposed fluid flow field that results in net diffusive-like transport [175] (see especially Ch VIII, Sec. 3).

The above considerations suggest that to observe an advection effect the motion must somehow be biased and irregular. In fact, the motion of biological membranes is commonly driven by thermal fluctuations and hence is random. We explore this using a familiar mechanical model for such motion. We also confirm our comments concerning regular motion by setting

$$h(t) = h_0 + a \sin \omega t, \text{ with } h_0 > 0, |a| < h_0. \tag{4.2}$$

We note that a similar model has been proposed by Pannuzzo *et al.* [176] and here we carry such analysis further. Our mathematical development is, however, quite different, as are our conclusions.

4.3 Mathematical formulations

4.3.1 Fluid flow field

The relevant equations for Stokes flow are

$$0 = -\nabla p + \mu \nabla^2 \mathbf{v} \text{ with } \nabla \cdot \mathbf{v} = 0, \tag{4.3}$$

with $\mathbf{v}$ being the fluid velocity and μ the fluid viscosity. Geometry suggests that $\mathbf{v}$ is of the form

$$\mathbf{v} = v_r\mathbf{e}_r + v_z\mathbf{e}_z, \tag{4.4}$$

with $\mathbf{e}_r$ and $\mathbf{e}_z$ unit base vectors, and $v_\theta = \partial(.)/\partial\theta = 0$ by radial symmetry. Dimensional analysis, noting that $h/R \ll 1$, leads to the typical *thin film* approximation [172] of eq. 4.3, *viz.*

$$\frac{\partial p}{\partial r} = \mu\frac{\partial^2 v_r}{\partial z^2}. \tag{4.5}$$

Integrating eq. 4.5 yields

$$v_r = \frac{1}{2\mu}\frac{\partial p}{\partial r}z(z-h), \tag{4.6}$$

since no-slip conditions demand, even within the thin film approximation, that $v_r = 0$ for $z = 0, h$ [172, 174, 177]. Now use $\nabla\cdot\mathbf{v} = 0$ in cylindrical coordinates to obtain

$$\frac{1}{r}\frac{\partial}{\partial r}(rv_r) + \frac{\partial v_z}{\partial z} = 0, \tag{4.7}$$

and then

$$v_z = -\frac{1}{2\mu r}\frac{\partial}{\partial r}(r\frac{\partial p}{\partial r})\left\{\frac{z^3}{3} - \frac{z^2}{2}\right\}. \tag{4.8}$$

Since $v_z(z = h) = \mathrm{d}h/\mathrm{d}t$, we find from eq. 4.7

$$\frac{\partial}{\partial r}(r\frac{\partial p}{\partial r}) = \frac{12\mu r}{h^3}\frac{\mathrm{d}h}{\mathrm{d}t}, \tag{4.9}$$

which when substituted back into eq. 4.8 yields

$$v_z = -6\frac{\mathrm{d}h}{\mathrm{d}t}\left\{\frac{1}{3}(\frac{z}{h})^3 - \frac{1}{2}(\frac{z}{h})^2\right\}. \tag{4.10}$$

Now from eq. 4.9 we find, upon integration

$$\frac{\partial p}{\partial r} = \frac{6\mu r}{h^3}\frac{\mathrm{d}h}{\mathrm{d}t} + \frac{y(t)}{r}. \tag{4.11}$$

whence, using eq. 4.6,

$$v_r = -3\frac{1}{h}\frac{\mathrm{d}h}{\mathrm{d}t} r\Big\{(\frac{z}{h}) - (\frac{z}{h})^2\Big\}. \tag{4.12}$$

In eq. 4.11, $y(t) = 0$ since no singularity is allowed.

At this point we again appeal to a thin film approximation [172, 174] and define a through thickness average radial velocity component

$$\bar{v}_r = \frac{1}{h}\int_0^h v_r \mathrm{d}z = -\frac{1}{2h}\frac{\mathrm{d}h}{\mathrm{d}t} r. \tag{4.13}$$

We also note from eqs. 4.10 and 4.12 that v_r/v_z scales as Rh^{-1} and thus the thin film approximation would justify ignoring v_z as compared to v_r [172, 174].

Incidently, the synapse can be alternatively modeled as two opposing identical disks. Details about the fluid dynamics of this system are included in Appendix 4.5.

For later reference, we also compute the pressure within the gap by integrating eq. 4.11 to obtain

$$p = \frac{3\mu}{h^3}\frac{\mathrm{d}h}{\mathrm{d}t} r^2 + f(t), \tag{4.14}$$

whereupon we note that at $r = R$, $p = p_0$, the outside pressure. Hence

$$p(r) = p_0 + \frac{3\mu}{h^3}\frac{\mathrm{d}h}{\mathrm{d}t}(r^2 - R^2). \tag{4.15}$$

Then form the area integrated pressure difference $p - p_0$, *i.e.*

$$f = \int_0^{2\pi}\int_0^R \{p(r) - p_0\}\, r\mathrm{d}r\mathrm{d}\theta = -\frac{3\pi\mu}{2}\frac{R^4}{h^3}\frac{\mathrm{d}h}{\mathrm{d}t} = -\xi\frac{\mathrm{d}h}{\mathrm{d}t}. \tag{4.16}$$

The force f is a resistive force, or adhesive force, resisting disc motion. For later use we note that

$$\xi = \frac{3\pi\mu}{2}\frac{R^4}{h^3} \tag{4.17}$$

serves as a *friction coefficient.* We note that this result for the drag coefficient may be extracted from Davis' analysis [178] of sedimentation of disc-like particles approaching a rigid plane in the limit where $h/R \ll 1$. The fluid velocity field is not readily extracted as hence is developed here.

4.3.2 Random vibration of the membrane disc

As described in Fig. 4.2a, our model for the disc is the all too familiar damped oscillator attached to a linear spring, k, and damper, c. We dub $\omega_0^2 = k/m$ and $\gamma = c/m$, where m is the disc's mass. We assume, as our numerics for the physical parameters later describes, that $\gamma^2/4 \gg \omega_0^2$, *i.e.* an overdamped regime. We let $h(t) = h_0 + \eta(t)$, where h_0 is the average and rest elevation of the disc. Let the disc be driven by a random force, $\mathcal{F}(t)$, caused by thermal fluctuations. This random force can be quantified by coupling the disc system to a heat bath. Hence one model for $\mathcal{F}(t)$, or $\eta(t)$, is as a Gaussian white noise variable with a delta correlation satisfying $\langle \mathcal{F}(t_1)\mathcal{F}(t_2)\rangle = \Gamma\delta(t_2 - t_1)$ with Γ the strength of the force.

However, we note that the mechanical model for our structural system shown in Fig. 4.2 presents constraints on $h(t)$. For example, we require $|\eta(t)| < h_0$, as clearly $h(t) > 0$. To handle such constraints we may postulate that $\mathcal{F}(t)$, and later $\eta(t)$, be described as *random telegraph noise* [179] where, for example, $\eta(t)$ transitions between $\eta = -s \,\text{to}\, s$ and $\eta = s \,\text{to}\, -s$, $0 \le s < h_0$, with rates ν_1 and ν_2, respectively. This means that the fractions of time spent in gap compression and opening modes are $\nu_2/(\nu_1 + \nu_2)$ and $\nu_1/(\nu_1 + \nu_2)$, respectively. The telegraph noise fluctuations of $\eta(t)$ are correlated as

$$\langle \eta(t_1)\eta(t_2)\rangle = \frac{4s^2\nu_1\nu_2}{\nu^2}\mathrm{e}^{-\nu|t_1-t_2|}, \tag{4.18}$$

with $\nu = \nu_1 + \nu_2$, a smoother transition than the delta correlation of Gaussian white noise. For straightforward connection of our system to a thermal heat bath, as we do below, we will take $\Delta\nu = \nu_2 - \nu_1 = 0$ which yields

$$\langle \eta(t_1)\eta(t_2)\rangle = s^2\mathrm{e}^{-\nu|t_1-t_2|} \rightsquigarrow \langle \eta^2(t)\rangle = s^2. \tag{4.19}$$

We also note that, as with Gaussian white noise, we will have with $\Delta\nu = 0$

$$\langle \eta(t)\rangle = -s\frac{\Delta\nu}{\nu} = 0. \tag{4.20}$$

For future reference, and study, we observe that with nonzero $\Delta\nu$, say $\Delta\nu > 0$, we would be describing scenario's where the gap spends more time in compression than in an opening mode; the opposite will be true if $\Delta\nu < 0$. For now, we emphasize that with the view just presented above we will have $|\eta(t)| < h_0$ and hence $h(t) > 0$. This is important for the development of Section 4.3.3 to follow.

With either view for the stochastic description, the equation of motion is

$$\frac{\mathrm{d}^2\eta}{\mathrm{d}t^2} + \gamma\frac{\mathrm{d}\eta}{\mathrm{d}t} + \omega_0^2\eta = \frac{\mathcal{F}(t)}{m}. \tag{4.21}$$

Recall, that γ is from the previous section, *i.e.* eq. 4.17,

$$\gamma = \frac{\xi}{m} = \frac{3\pi\mu}{2m}\frac{R^4}{h^3} \rightsquigarrow \gamma \approx \frac{3\pi}{2m}\frac{R^4}{h_0^3}\mu. \tag{4.22}$$

The 2$^{\text{nd}}$ of eq. 4.22 aims to linearize eq. 4.21 in the range where $|\eta| \ll h_0$. As $\eta(t)$ is a random motion, driven by $\mathcal{F}(t)$, its average is $\langle\eta(t)\rangle = 0$.

The resolution of eq. 4.21 follows standard lines as in brownian motion [180], *e.g.* begin by multiplying through by η to obtain

$$\eta\frac{\mathrm{d}^2\eta}{\mathrm{d}t^2} + \gamma\eta\frac{\mathrm{d}\eta}{\mathrm{d}t} + \omega_0^2\eta^2 = \eta\frac{\mathcal{F}(t)}{m}, \tag{4.23}$$

and note that

$$\begin{aligned}&\eta\mathrm{d}\eta/\mathrm{d}t = 1/2\,\mathrm{d}\eta^2/\mathrm{d}t, \text{ and}\\ &\eta\mathrm{d}^2\eta/\mathrm{d}t = 1/2\,\mathrm{d}^2\eta^2/\mathrm{d}t^2 - (\mathrm{d}\eta/\mathrm{d}t)^2.\end{aligned} \tag{4.24}$$

This leads to

$$\frac{\mathrm{d}^2\eta^2}{\mathrm{d}t^2} + \gamma\frac{\mathrm{d}\eta^2}{\mathrm{d}t} + \omega_0^2\eta^2 = 2\left(\frac{\mathrm{d}\eta}{\mathrm{d}t}\right)^2 + \eta\frac{\mathcal{F}(t)}{m}. \tag{4.25}$$

Now take time average values across eq. 4.25 to obtain

$$\begin{aligned}\frac{\mathrm{d}^2\langle\eta^2\rangle}{\mathrm{d}t^2} + \gamma\frac{\mathrm{d}\langle\eta^2\rangle}{\mathrm{d}t} + \omega_0^2\langle\eta^2\rangle &=\\ 2\,\langle\left(\frac{\mathrm{d}\eta}{\mathrm{d}t}\right)^2\rangle + \langle\eta\frac{\mathcal{F}(t)}{m}\rangle&.\end{aligned} \tag{4.26}$$

Note that as η and $\mathcal{F}$ are uncorrelated, the last term is zero since $\langle\eta\rangle = 0$. To connect our disc to a heat bath invoke the equipartition theorem [180, 181] to obtain

$$\frac{\mathrm{d}^2\langle\eta^2\rangle}{\mathrm{d}t^2} + \gamma\frac{\mathrm{d}\langle\eta^2\rangle}{\mathrm{d}t} + \omega_0^2\langle\eta^2\rangle = 2\,\frac{kT}{m}. \tag{4.27}$$

The next step is make a change of variables and set $\langle\eta^2\rangle = q(t)\,\mathrm{e}^{-\gamma t/2}$, which leads to

$$\frac{d^2q}{dt^2} + (\omega_0^2 - \gamma^2/4)q = \frac{2kT}{m}\mathrm{e}^{\gamma t/2}. \tag{4.28}$$

We choose a simple and convenient set of initial conditions that ensure that $q > 0$, *viz.*

$\langle \eta^2(0) \rangle = 2kT/\omega_0^2$ and $\mathrm{d}\langle \eta(0) \rangle\ \mathrm{d}t = 0$. The solution is

$$\begin{aligned}\langle \eta^2 \rangle(t) =& \frac{2kT}{m\omega_0^2}\Big\{\cosh(\zeta t) + \frac{\gamma}{2\zeta}\sinh(\zeta t)\Big\}\mathrm{e}^{-\gamma t/2} \\ &+ \frac{2kT}{m\omega_0^2},\end{aligned} \tag{4.29}$$

with $\zeta = (\gamma^2/4 - \omega_0^2)^{1/2}$.

The trailing constant in eq. 4.29 is a long time, *i.e.* stationary, solution in that if, as we assume, $\gamma^2/4 \gg \omega_0^2$

$$\langle \eta^2 \rangle(t \to \infty) \to \frac{2kT}{m\omega_0^2}. \tag{4.30}$$

To obtain this required analytic solution, we have not constrained the amplitudes of motion of our mechanical model of Fig. 4.2. We nonetheless note that within the entire range of values for physical parameters described later in Section we indeed find that $\langle |\eta^2(t)| \rangle < h_0^2$.

4.3.3 The random flow field

For the flow field of eq. 4.13, we need the following quantity and we note that

$$\frac{1}{h}\frac{\mathrm{d}h}{\mathrm{d}t} = \frac{1}{2h^2}\frac{\mathrm{d}h^2}{\mathrm{d}t} = \frac{1}{h}\frac{\mathrm{d}\eta}{\mathrm{d}t}. \tag{4.31}$$

On the other hand we also note that $h^2 = h_0^2 + 2h_0\eta + \eta^2$ leads to

$$\begin{aligned}&\frac{\mathrm{d}h^2}{\mathrm{d}t} = 2h_0\frac{\mathrm{d}\eta}{\mathrm{d}t} + \frac{\mathrm{d}\eta^2}{\mathrm{d}t}, \text{ whereby} \\ &\frac{\mathrm{d}\eta}{\mathrm{d}t} = h_0\frac{1}{h}\frac{\mathrm{d}\eta}{\mathrm{d}t} + \frac{1}{2h}\frac{\mathrm{d}\eta^2}{\mathrm{d}t}.\end{aligned} \tag{4.32}$$

Now realizing that both $\langle n(t)\rangle = 0$ and $\langle \mathrm{d}\eta/\mathrm{d}t\rangle = 0$, when average values are taken across the second of eq. 4.32 we find that

$$\langle \frac{1}{h}\frac{d\eta}{dt}\rangle = -\frac{1}{2h_0}\langle \frac{1}{h}\frac{d\eta^2}{dt}\rangle \approx -\frac{1}{2h_0^2}\langle \frac{d\eta^2}{dt}\rangle. \tag{4.33}$$

Recall, that we have set things up so that $h(t) = h_0 + \eta(t) > 0$ which helps justify the above approximation. Using eq. 4.29 we find

$$\langle \frac{1}{h}\frac{d\eta}{dt}\rangle \approx \frac{kT}{m\gamma h_0^2}\,\mathrm{e}^{-\omega_0^2 t/\gamma}. \tag{4.34}$$

We note that when this is used with eq. 4.13 we find that the forecasted radial fluid velocities are of order $0.5-1.0\mu\mathrm{m}s^{-1}$ as was coincidentally found to be representative in the experimental study of Chary and Jain [157], and as was mentioned in the 1st ¶ of Section 4.1.

4.3.4 Diffusion-advection equation and its solution

The diffusion-advection equation reads as follows:

$$\frac{\partial c}{\partial t} = D\nabla^2 c - \nabla\cdot(c\mathbf{v}), \tag{4.35}$$

where c is concentration, D diffusion coefficient, and $\mathbf{v}$ again is the fluid velocity. We will transform this to a purely radial equation as follows. To begin we note that we have assumed radial symmetry, hence $c = c(r,z)$, $\mathbf{v} = \mathbf{v}(r,z)$. Recall the definition within the thin film approximation of $\bar{v}_r$ in eq. 4.13. The diffusion term involving $\nabla^2 c$ will be clear enough, but attention to the advective term requires comment.

In cylindrical coordinates, and in component form

$$\nabla\cdot(c\mathbf{v}) = \frac{1}{r}\frac{\partial}{\partial r}(rv_r c) + \frac{1}{r}\frac{\partial(cv_\theta)}{\partial\theta} + \frac{\partial(cv_z)}{\partial z}. \tag{4.36}$$

Carrying out the operations and grouping terms into 2 groups we find

$$\begin{aligned}\nabla\cdot(c\mathbf{v}) = &\\ &c\frac{1}{r}\frac{\partial}{\partial r}(rv_r)+c\frac{1}{r}\frac{\partial v_\theta}{\partial\theta}+c\frac{\partial v_z}{\partial z}\ (=0)\\ &+v_r\frac{\partial c}{\partial r}+\frac{v_\theta}{r}\frac{\partial c}{\partial\theta}+v_z\frac{\partial c}{\partial z}\ (\neq 0).\end{aligned} \tag{4.37}$$

The first group is zero since, in this case, $\nabla\cdot\mathbf{v}=0$. The second term in the second group is zero due to radial symmetry. Hence

$$\nabla\cdot(c\mathbf{v}) = v_r\frac{\partial c}{\partial r}+v_z\frac{\partial c}{\partial z}. \tag{4.38}$$

Now again in the spirit of our thin film approximation, we define $\bar{c}$ as

$$\bar{c}(r)=\int_0^h c(r,z)dz; \tag{4.39}$$

hence $\partial\bar{c}/\partial z=0$. Thus

$$\nabla\cdot(\bar{c}\mathbf{v}) = v_r\frac{\partial\bar{c}}{\partial r}. \tag{4.40}$$

The diffusion-advection equation thus reads

$$\begin{aligned}&\frac{\partial\bar{c}}{\partial t}=D\nabla_r^2\bar{c}-v_r\frac{\partial\bar{c}}{\partial r}\ \text{with}\\ &\nabla_r^2=\frac{\partial^2}{\partial r^2}+\frac{1}{r}\frac{\partial}{\partial r}.\end{aligned} \tag{4.41}$$

Recalling eq. 4.13, eq. 4.41 reads as, with eq. 4.34,

$$\frac{\partial\bar{c}}{\partial t}=D\nabla_r^2\bar{c}+\frac{1}{2}\Big(\frac{1}{h}\frac{\mathrm{d}h}{\mathrm{d}t}\Big)r\frac{\partial\bar{c}}{\partial r} \tag{4.42a}$$

$$\frac{\partial\bar{c}}{\partial t}=D\nabla_r^2\bar{c}+\frac{1}{2}\frac{kT}{m\gamma h_0^2}\,\mathrm{e}^{-\omega_0^2 t/\gamma}\,r\frac{\partial\bar{c}}{\partial r} \tag{4.42b}$$

4.3.5 Resolution of eq. 4.42

The boundary condition $c(R,t)=0$, now $\bar{c}(R,t)=0$, suggests a separated solution of the form

$$\bar{c}(r,t)=\sum_{m=1}^{\infty} A_m(t) J_0(\lambda_m r), \tag{4.43}$$

where the λ_m are chosen such that $\lambda_m R$ are the zeros of the Bessel function $J_0(x)$, that is $\lambda_m R = 2.40483, 5.52008, \ldots (m-1/4)\pi$, for $m \gg 1$. With this, there is the orthogonality condition

$$\int_0^R J_0(\lambda_m r) J_0(\lambda_n r)\, r \mathrm{d}r = \begin{cases} 1/2 R^2 J_1^2(\lambda_n R), & m=n \\ 0, & m \neq n \end{cases} . \tag{4.44}$$

Equation 4.42b is rewritten as

$$\frac{\partial \bar{c}}{\partial t} - D \nabla_r^2 \bar{c} - \frac{1}{2} \frac{kT}{m\gamma h_0^2} \mathrm{e}^{-\omega_0^2 t/\gamma}\, r \frac{\partial \bar{c}}{\partial r} = 0. \tag{4.45}$$

The procedure is standard, namely multiply through eq. 4.45 by $r J_0(\lambda_n r)$ and integrate over the range $[0,R]$ using eq. 4.44; we note however that the 3^{rd} term in eq. 4.45 would be handled by first using the fact that

$$r \frac{\partial}{\partial r} J_0(\lambda_m r) = \lambda_m \frac{\partial}{\partial \lambda_m} J_0(\lambda_m r). \tag{4.46}$$

This brings us to a critical step in which

$$\frac{\partial}{\partial \lambda_n} J_1^2(\lambda_n R) = 2 J_1(\lambda_n R) \Big\{ R J_0(\lambda_n R) - R/(\lambda_n R) J_1(\lambda_n R) \Big\} \tag{4.47}$$

where, of course, the first term in brackets is zero since $J_0(\lambda_n R)=0$.

When the terms are assembled we arrive at the ODE for $A_n(t)$, *viz.*

$$A_n'(t) + \left\{\lambda_n^2 D + \frac{kT}{m\gamma h_0^2}\,\mathrm{e}^{-\omega_0^2 t/\gamma}\right\} A_n(t) = 0, \text{ or} \tag{4.48a}$$

$$A_n'(t) + \left\{\lambda_n^2 D + \beta\,\mathrm{e}^{-st}\right\} A_n(t) = 0, \text{ with} \tag{4.48b}$$

$$\beta = \frac{kT}{m\gamma h_0^2}, \text{ and } s = \omega_0^2/\gamma. \tag{4.48c}$$

The solution to eq. 4.48b is

$$A_n(t) = A_n^\circ \exp(-\lambda_n^2 D t + \beta/s\,\mathrm{e}^{-st}) \tag{4.49a}$$

$$\text{with } A_n^\circ = A_n(0)\mathrm{e}^{-\beta/s} \tag{4.49b}$$

$$A_n(t) = A_n(0)\mathrm{e}^{-\beta/s} \exp(-\lambda_n^2 D t + \beta/s\,\mathrm{e}^{-st}). \tag{4.49c}$$

The coefficients $A_n(0)$ are determined from the initial condition

$$c_0 = \sum_{n=1}^{\infty} A_n(0) J_0(\lambda_n r), \tag{4.50}$$

which leads to

$$A_n(0) = \frac{2c_0}{(\lambda_n R) J_1(\lambda_n R)}. \tag{4.51}$$

Thus we find

$$\frac{\bar{c}}{c_0} = \sum_{n=1}^{\infty} \frac{2}{(\lambda_n R) J_1(\lambda_n R)} \mathrm{e}^{-\beta/s} \exp(-\lambda_n^2 D t + \beta/s\,\mathrm{e}^{-st})$$

$$J_0(\lambda_n r), \tag{4.52a}$$

$$\tilde{c} = \frac{\bar{c}}{c_0} = \mathrm{e}^{-\beta/s} \exp(\beta/s\,\mathrm{e}^{-st}) \sum_{n=1}^{\infty} \frac{2\,\mathrm{e}^{-\lambda_n^2 D t}}{(\lambda_n R) J_1(\lambda_n R)} J_0(\lambda_n r). \tag{4.52b}$$

A simple, yet, informative way to visualize this solution is to compute an area average of $\tilde{c}$; for this we need

$$\frac{1}{\pi R^2}\int_0^{2\pi}\int_0^R J_0(\lambda_n r)\mathrm{d}\theta r\mathrm{d}r = \frac{2}{\lambda_n R}J_1(\lambda_n R), \tag{4.53}$$

which when used with eq. 4.52b yields

$$\langle\tilde{c}\rangle = \mathrm{e}^{-\beta/s}\exp(\beta/s\,\mathrm{e}^{-st})\sum_{n=1}^{\infty}\frac{4}{(\lambda_n R)^2}\,\mathrm{e}^{-\lambda_n^2 Dt}, \tag{4.54}$$

where here the averaging $\langle.\rangle$ denotes that average taken in eq. 4.53. Indeed, when $t=0$, we find $\langle\tilde{c}\rangle = 1$ since

$$4\sum_{n=1}^{\infty}\frac{1}{(\lambda_n R)^2} = 1, \tag{4.55}$$

and recalling that the $\lambda_n R$ are the zeros of $J_0(x)$.

It is of interest to explore a few limits of eq. 4.54. For example, and obviously, when $t\to\infty$, and $D\neq 0$, $<\tilde{c}>\to 0$ since diffusion guarantees such given the boundary condition $c(R,t)=0$. More revealing, however, is the case where we set $D=0$ and thus suppress diffusion, leaving only advection to transport solute. In this case eq. 4.54 reads as

$$\langle\tilde{c}\rangle = \mathrm{e}^{-\beta/s}\exp(\beta/s\,\mathrm{e}^{-st}) \underset{t\to\infty}{\rightsquigarrow} \langle\tilde{c}\rangle = \mathrm{e}^{-\beta/s}, \tag{4.56}$$

given eq. 4.55. Since $\beta/s>0$, we see that advection indeed leads to a reduction in average solute concentration. Moreover, we note that the effects of advection are transient, and are focused on the initial time of the transport event.

Inspection of the simple results in eqs. 4.54 and 4.56 reveals some key aspects of the advection-diffusion coupling. Clearly the time scales for the two processes can be quite different. For advection, s determines the time scale whereas for diffusion the exponents $\lambda_n^2 D$ determine time scales. If advection is to couple to, *i.e.* compete, diffusion s should be comparable to the $\lambda_n^2 D$, or at least to $\lambda_1^2 D$, where $\lambda_1 = 2.40483/R$ is the first eigenvalue of $J_0(x)$. Thereby we define $\mathcal{A}^D \equiv s/\lambda_1^2 D$ as a sort of Peclet number.

We note here that the "inverse problem" is of value and is readily generated from the above solution; the inverse is defined so that the initial concentration is zero within the gap and c_0 outside. Detailed formulations are included in Appendix 4.5.

4.3.6 Regular disc motion: *e.g.* harmonic motion

Recall, even before exploring more detailed results that eq. 4.54 is based on a model that describes random motion of the disc and its induced fluid flow field. It is important to note this with respect to the reversibility of Stokes flow as discussed in connection with eq. 4.2. Specifically consider such harmonic motion that would specify

$$h(t) = h_0 + a \sin \omega t \text{ with} \tag{4.57a}$$

$$\frac{1}{h}\frac{\mathrm{d}h}{\mathrm{d}t} = \frac{\mathrm{d}\ln h}{\mathrm{d}t} = \frac{a\omega \cos \omega t}{h_0 + a \sin \omega t}. \tag{4.57b}$$

When eq. 4.57b is used in eq. 4.48b instead of $\beta \mathrm{e}^{-st}$, we find the following. Consider the ODE

$$A_n'(t) + p(t) A_n(t) = 0, \tag{4.58}$$

and its solution

$$A_n(t) = A_n^\circ \exp\left\{ -\int^t p(t) dt \right\}. \tag{4.59}$$

In our case

$$p(t) = \lambda_n^2 D + \frac{1}{h}\frac{\mathrm{d}h}{\mathrm{d}t} = \lambda_n^2 D + \frac{\mathrm{d}\ln h}{\mathrm{d}t}. \tag{4.60}$$

The solution to eq. 4.59 with eq. 4.60 is

$$A_n(t) = A_n^\circ \left(\frac{1}{h_0 + a \sin \omega t} \right) \mathrm{e}^{-\lambda_n^2 D t}. \tag{4.61}$$

Dimensional consistency is attained when we realize that $A_n(0) = A_n^\circ / h_0$, hence

$$A_n(t) = A_n(0)\left(\frac{h_0}{h_0 + a\sin\omega t}\right) \mathrm{e}^{-\lambda_n^2 Dt}, \tag{4.62}$$

where $A_n(0)$ is obtained *via* the initial condition as in eqs. 4.50 and 4.51.

Within the context of the simple model posed herein, the result of eq. 4.62 concerning the advection would go something like this: *what goes out, comes back in.* This arises due to the reversibility of Stokes flow [172, 173] when dealing with smooth reversible fluid flow. We recall, however, that the time average of the advection flow field is driven by the average quantity $\langle h^{-1}\mathrm{d}\eta/\mathrm{d}t\rangle$ that we have shown in Sections 4.3.2 and 4.3.3 is nonzero, yet decaying exponentially in time. Fluid flow in this case is not a smooth reversible flow but is stochastic in nature, and hence such simple reversibility does not apply [167].

4.4 Results

4.4.1 Numerics for parameters

Figures 4.1 and 4.3 illustrate key structural features of the synapse cleft (*i.e.* gap) and the release of neurotransmitters. From Savtchenko and Rusakov [158] we note the following dimensions (see also Fig. 4.2): $150\text{nm} \leq R \leq 300\text{nm}$ and $12.5\text{nm} \leq h_0 \leq 20\text{nm}$. We take the viscosity, μ, to be in the range $\sim 10^{-3}\,\text{Nsm}^{-2}$ [170]. For the mass, m, we use the range $10^{-15}\,\text{kg} \leq m \leq 10^{-15}\,\text{kg}$. This places γ, as per eq. 4.22, in the approximate range $10^{8}\,\text{s}^{-1} \leq \gamma \leq 10^{9}\,\text{s}^{-1}$. For D we use values in the range $10^{-12}\text{m}^2\text{s}^{-1} \leq D \leq 10^{-9}\text{m}^2\text{s}^{-1}$; this includes the range identified for glutamate within the synaptic cleft [158, 169].

The key parameters within eqs. 4.52a,b, 4.54 and 4.56 can be summarized as

$$\begin{gathered} \beta = \frac{\alpha kT}{m\gamma h_0^2}, \quad s = \frac{\omega_0^2}{\gamma}, \quad \beta/s = \frac{\alpha kT}{m\omega_0^2 h_0^2} \\ \omega_0^2 = \frac{E\pi R_a^2}{\ell_a m}, \qquad \gamma = \frac{3\pi}{2m}\frac{R^4}{h_0^3}\mu. \end{gathered} \tag{4.63}$$

We note that the scaling parameter α equals unity for thermal fluctuations alone as was originally envisioned in eq. 4.27. However, suppose that we allow for the inclusion of additional energy input, *e.g.* from ATP hydrolysis that is known to occur in the process of vesicle release and recycling in the synapse [182, 183]. For perspective, recall that the standard free energy of ATP hydrolysis is $\Delta G = -30.5\text{kJmol}^{-1}$. This translates to $\Delta g \approx -12kT$ per molecule. Moreover, with typical cell concentrations $c_{\text{ATP}} = 3\text{mM}, c_{\text{ADP}} = 0.8\text{mM}, c_{P_i} = 4\text{mM}$ [184], a simple calculation, for the reaction $\text{ATP} + \text{H}_2\text{O} \leftrightarrows \text{ADP} + \text{P}_i$, shows that $\Delta G = -48.1\text{kJmol}^{-1}$, *i.e.* $\Delta g \approx -19kT$ per molecule. Indeed, for some time now vibrations of microtubles and actin filaments have been suspected to be driven by hydrolysis of ATP and/or GTP [185]. More recently, ATP powered nonequilibrium fluctuations of the human red blood cell membrane have been analyzed [186] and are thought to be an important influence on cell shape. Hence metabolic energy release *per se* could justify α in the range $5 \leq \alpha \leq 10$, for instance. From the experimental results of Park *et al* [186] one would estimate $\alpha = 2$.

The parameters contained in eqs. 4.63 have been explained *via* the above developments with the exception of ω_0^2 which is now explained with reference to Fig. 4.3.

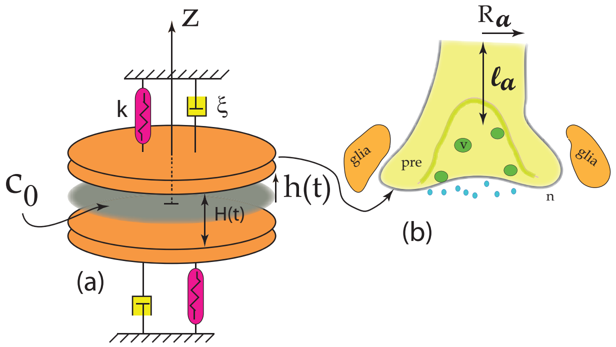

Figure 4.3. The synapse is modeled with more detail as a disc attached to a segment of axon that acts as a linear spring with constant $k = E\pi R_a^2/\ell_a$. Motion of the disc is also resisted by a viscous drag coefficient, ξ, given by eq. 4.17 and damping coefficient, γ, given in eq. 4.22.

Figure 4.3 again illustrates our synapse model but now attached to an elastic axon, with spring constant k (Fig. 4.3a), whose segment is of length ℓ_a (Fig. 4.3b) and radius R_a (not shown to scale). The radius is taken in the range $0.5\mu \leq R_a \leq 1\mu$, and its length in the range $\ell_a \sim 100\mu$. The linear spring constant would then be formed as $k = \pi R_a^2 E/\ell_a$ and hence the expression for ω_0^2 in eq. 4.63. Again, the disc-like synapse is resisted by a viscous drag ξ as given in eq. 4.17 that then prescribes γ in eq. 4.63.

As for the elastic modulus, E, we note recent measurements of chick nerve cell elasticity obtained *via* afm imaging [187, 188]. For chick neurons E was reported in the range $1\text{kPa} \leq E \leq 10\text{kPa}$ *in vivo* [187] whereas *in vitro* E was reported in the higher range $30\text{kPa} \leq E \leq 90\text{kPa}$ with a strong peak at $E \approx 70\text{kPa}$. In what follows we use a value of $E = 7\text{kPa}$ for numerical examples.

The relations in eq. 4.63 can be usefully combined, for use in eqs. 4.52a,b, 4.54 and 4.56, to yield

$$\begin{gathered} s = \frac{2}{3} E \frac{1}{\ell_a} \frac{R_a^2}{R^4} \frac{h_0^3}{\mu}, \quad \mathcal{A}^M = \beta/s = \frac{\alpha k T \ell_a}{\pi E R_a^2 h_0^2}, \\ \mathcal{A}^D = \frac{s}{\lambda_1^2 D} = \frac{2}{15} \frac{E}{\ell_a} \left\{ \frac{R_a}{R} \right\}^2 \frac{h_0^3}{D\mu}. \end{gathered} \tag{4.64}$$

We recall that eqs. 4.52a,b, 4.54 and 4.56 demonstrate that the parameters s and β/s are pivotal for yielding an influence of advection on solute transport. Equation eq. 4.56 shows that β/s, as in the term $\mathrm{e}^{-\beta/s}$, defines the prospective "magnitude" of the net advection contribution, but s controls the time scale, $\tau_a = 1/s$, on which advection occurs. Advection is in competition with diffusion occurring with time scales $\tau_d = 1/(\lambda_n^2 D)$. Hence for advection to contribute to solute transport $\mathcal{A}^D$ should be on the order of unity. The numerical factor in the last of eqs. 4.64 is obtained by noting that $\lambda_1 R = 2.40468$, *i.e.* the 1^{st} zero of $J_0(x)$. Since both s and β/s must be large enough for advection to have a noticeable influence eqs. 4.64 are seen to form a "tight box" in that varying individual parameters cannot produce arbitrarily optimal values. That is, there is indeed very little wiggle room and this feature provides additional credence to the model. Particular case examples of results from eqs. 4.52a,b, 4.54 and 4.56 provide further insight.

4.4.2 Results for case examples

For most of our cases we set $E = 7\text{kPa}$, $\ell_a = 100\mu\text{m}$, $R = 200\text{nm}$, $R_a = 1\mu\text{m}$, $\mu = 10^{-3}\,\text{Nsm}^{-2}$, $kT = 4 \times 10^{-21}$, $h_0 = 20 - 30\text{nm}$, and $D = 10^{-14} - 10^{-10}\text{m}^2\text{s}^{-1}$. Finally, we set $\alpha = 1 - 10$ assuming a modest additional random force input. These values specify the ranges $s \approx 250$ and $\beta/s \approx 0.25$. Also, with these values and for the values of D listed, $\mathcal{A}^D$ and $\mathcal{A}^M$, fall in the ranges $\mathcal{A}^D = 0.063 - 0.630$ and $\mathcal{A}^M = 0.0202 - 0.2021$.

Figure 4.4 shows $< \tilde{c} >$ *vs.* t for the parameters listed in each sub-figure; the following observations can be made. Note that in each set of cases we show results with $D = 0$; this illustrates the potential effect of advection alone as described by eq. 4.56.

Clearly when diffusion is relatively fast, *i.e.* $D \geq 10^{-10}\text{m}^2\text{s}^{-1}$, $\mathcal{A}^D$ is too small to allow advection to contribute to solute egress from the cleft-like geometry, yet when D is a low as $D = 10^{-11}\text{m}^2\text{s}^{-1}$ advection has a definite effect. This can also be appreciated by observing the time scales for measurable solute transport; with $D \geq 10^{-10}\text{m}^2\text{s}^{-1}$ the time scale is on order of 1ms, whereas if $D \leq 10^{-11}\text{m}^2\text{s}^{-1}$ time scales frow to order 10 ms. On the other hand, if $D \leq 10^{-12}\text{m}^2\text{s}^{-1}$ advection is seen to have a quite noticeable effect. This is seen by the trends shown in Fig. 4.4b. Thus it may be inferred that at least within the range of structural and physical properties used here advection would contribute to transport of only larger molecules with such low diffusion coefficients.

It should be noticed, however, that additional energy input, *i.e.* other than *via* thermal fluctuations, can have the significant effect of enhancing advective flow. This is clear from the trends shown in Fig. 4.4d-f.

Another feature of these results is that when advection does contribute, *i.e.* competes with diffusion, it happens at early times. This should be clear and anticipated from

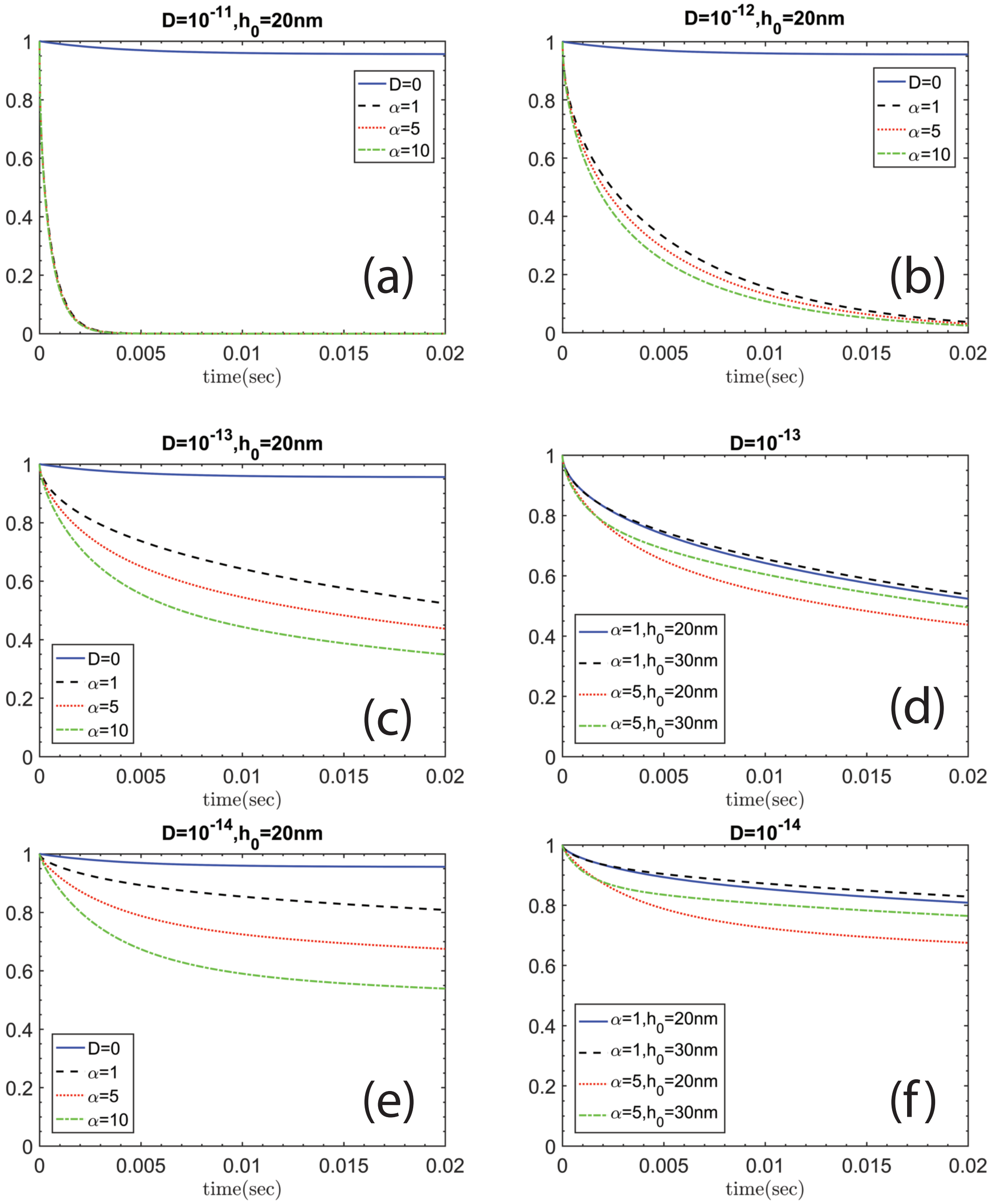

Figure 4.4. $< \tilde{c} >$ *vs.* t for the parameters listed on each of the six panels in the figure. Note that the effective diffusion coefficient ranges from $10^{-14} - 10^{-11}\mathrm{m}^2\mathrm{s}^{-1}$. For the cases a-c and e, we plot the result with $D = 0$ to more clearly reveal the effect of advection.

the transient nature of eq. 4.34. It can also be visualized by the larger slopes at short times for the cases shown in Figs. 4.4c-f.

4.5 Discussion and conclusions

The findings of Chary and Jain in 1989 [157] should have spurred a line of further inquiry into coupled effects of advection and diffusion in biological vessels, cells, and tissue, especially given the Starling's hypothesis [153] made in the 19th century. Indeed, earlier Swabb *et al.* [189] studied such effects in normal and neoplastic tissue and found that advection can dominate the flow especially for higher molecular weight molecules. Further note the ideas put forth by Nedergaard regarding advective flow in the brain [156]. We have commented on the fact that the fluid velocity range reported by Chary and Jain is quite comparable to what we forecast and that indeed when $D \sim 10^{-11}\mathrm{m}^2\mathrm{s}^{-1}$, we predict measurable advection contributions *vs* diffusion. It is informative to explore the respective forecasted pressure gradients as well. Chary and Jain report gradients of order $\partial p/\partial x \sim 4\mathrm{mmHg}/\mu\mathrm{m} \approx 5\times 10^{8}\mathrm{Pa\,m}^{-1}$, where this was based on assumed values for *hydraulic conductivity*, η, extracted from other literature. The initial value they used was $\eta = 10^{-12}\mathrm{cm}^4(\mathrm{dyne}-\mathrm{s})^{-1} = 10^{-15}\mathrm{m}^4(\mathrm{Ns})^{-1}$. They rightly questioned if such high gradients were sustainable *in-vivo* and hence proposed that the *hydraulic conductivity* could be 2-3 orders of magnitude higher so as to correctly lead to measured fluid velocities at more reasonable pressure gradients. If our eq. 4.6 is used, as in eq. 4.13, we find

$$\bar{v}_r = -\frac{h^2}{12\mu}\frac{\partial p}{\partial r} = -\eta\frac{\partial p}{\partial r}. \tag{4.65}$$

If we take $h = 20\,\mathrm{nm}$ and $\mu = 10^{-3}\,\mathrm{Ns\,m}^{-2}$ we find $\eta \sim 10^{-13}\mathrm{m}^4(\mathrm{Ns})^{-1}$, *i.e.* some 2 orders of magnitude larger that Chary and Jain's original estimate and that help verify their proposal of using larger hydraulic conductance. In fact, if we take $h \sim 60\,\mathrm{nm}$, *i.e.* mid-range of Chary and Jain's range $30-100\,\mathrm{nm}$, we find $\eta \sim 10^{-12}\mathrm{m}^4(\mathrm{Ns})^{-1}$, which is precisely what they proposed was possible. Thus our analysis indeed provides a pathway to explain, even quantitatively, experimental observations such as theirs.

We also note that our analysis shows that the effect of advection becomes significant when $D \leq 10^{-13}\mathrm{m}^2\mathrm{s}^{-1}$ with fluid velocities of order $v \sim 0.5\mu\mathrm{ms}^{-1}$ as found in Section 4.3.3. This forecast is consistent with the analysis of the experimental results of Koslover *et al.* [168] who report that advection effects become important for particle transport with diffusion coefficients with extracted (*via* their analysis) values of order $D \sim 2 \times 10^{-14} m^2 s^{-1}$; their measured fluid velocities were, indeed, in the range $v \sim 0.5\mu\mathrm{ms}^{-1}$. This again demonstrates a consistency of our model analysis with experiment in terms of observed phenomenology and the numerology regarding key parameters such as fluid velocity and diffusion whose values determine the competition between advection and diffusion.

Reviewing again eqs. 4.64, we see that simultaneously optimizing $s, \beta/s,$ and $\mathcal{A}^D$ is quite difficult. With slightly larger cleft widths, certainly verified for many types of biological channels, the time scale of advection can be shortened (*i.e.* quickened) so it competes more effectively with diffusion. However, this alone would reduce β/s, the magnitude of the eventual advection effect. To obtain an optimal set of values α, *i.e.* additional energy input, is required. This then poses a fundamental question: How does possible metabolic energy enter into such mechanical phenomena? Is it direct or indirect such as by participating in molecular restructuring? And, how much energy is involved and how is it triggered? Thus our model analysis indeed clearly points to the potential vital role of energetic input into biological transport processes.

Our analysis demonstrates that when advection is driven by structural motion, there are a rather rigid set of criteria that are required for it to compete with diffusion. It may be that our modeling of the synaptic-like body as a rigid disc is too restraining and explicit account should be taken of the flexible synaptic membranes. This would lead to enhanced structural motion, driving fluid motion, and increased advective solute current. This remains to be explored, especially in the context of other biological gap-like channels such as exist within the brain [156] for instance. But even here care must be taken to identify the energetic sources that drive fluid flow. Aspects of such scenarios have been addressed by Bickel [190] who has argued that random motion of opposing membranes indeed affects particle transport in viscous media.

We also note that our finding that $\mathcal{A}^D \sim 1/R^2$ is due to the fact that structural motion that drives fluid flow is resisted by a drag coefficient that scales as $\xi \sim R^4$. Péclet numbers are often defined *via* dimensional analysis leading to $\mathcal{P}_e = UL/D$, with U being fluid velocity and L diffusion distance. In our case, however, U is a strongly decreasing with L and it is this that leads to our $\mathcal{A}^D \sim 1/R^2$.

Finally, we comment that our choice of random telegraph noise used to describe either $\mathcal{F}(t)$ or $\eta(t)$ was based on geometric constraints discussed in Section 4.3.2 and that this choice provided a simple connection to thermal fluctuations *via* the equipartition theorem. Recall that our goal was a model scenario that would allow a clear assessment of the contributions of advection *vs.* diffusion and its link to a set of well defined physical parameters that mediate the system's response. As noted, however, in Section 4.3.2 the choice of telegraph noise provides an opportunity to explore cases where the physical system is biased in that $\langle \eta(t) \rangle \neq 0$, *i.e.* $\nu_1 \neq \nu_2$. Such may well the case where the stimulus for motion is in the form of energetic bursts or pulses such as exist in the synapse, for example. This is, indeed, a topic of future research.

Acknowledgement

Chapter 4, in full, is a reprint of the material as it appears in *Physical Review E* 97.4 (2018): 042401. Asaro, Robert; Zhu, Qian; Lin, Kuan-Po, 2017. The dissertation author was the primary investigator and author of this paper.

Appendix A: Opposing discs model of synapse

Still another model for the synapse is that shown in Fig. 4.5 in which we envision the pre- and post synapses as two opposing identical discs. Here we describe the discs lying at elevations $z = \pm h(t)$; hence the total gap is $H(t) = 2h(t)$. Note that now the no slip boundary condition reads as $v_z(r, z = \pm h) = 0$. The solution to eq. 4.5 is then

$$v_r = \frac{1}{2\mu}\frac{\partial p}{\partial r}(z^2 - h^2). \tag{4.66}$$

Incompressibility, *via* eq. 4.7, now leads to

$$v_z = -\frac{1}{2\mu r}\frac{\partial}{\partial r}(r\frac{\partial p}{\partial r})\Big\{\frac{z^3}{3} - h^2 z\Big\}. \tag{4.67}$$

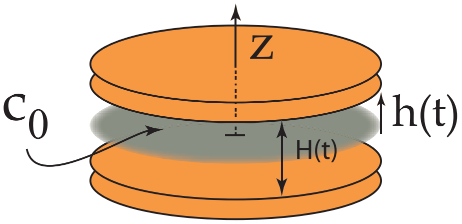

Figure 4.5. Here the pre- and post synapses are modeled as two identical opposing discs separated by $H(t) = 2h(t)$.

Following the procedure outlined above, we find that

$$[p]^{\text{in}}_{\text{out}} = p(r) - p_0 = \frac{3\mu}{4h^3}\frac{\mathrm{d}h}{\mathrm{d}t}(r^2 - R^2) = \frac{3\mu}{H^3}\frac{\mathrm{d}H}{\mathrm{d}t}(r^2 - R^2). \tag{4.68}$$

Comparing this to the pressure difference in eq. 4.15 we find that the friction coefficient, ξ, in eq. 4.17 is recovered. Moreover, the through thickness radial fluid velocity is

$$\bar{v}_r = -\frac{1}{H}\frac{\mathrm{d}H}{\mathrm{d}t}r, \tag{4.69}$$

and thereby of the same form as in eq. 4.13 as per the total cleft width of either $h(t)$ or $H(t)$.

Appendix B: The *Inverse problem*

The inverse problem is one where the initial and boundary conditions are $c(r,0) = 0$ within the gap and $c(R,t) = c_0$ on the perimeter of the disc as depicted in Fig. 4.6.

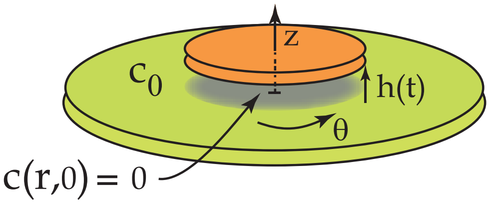

Figure 4.6. The inverse problem assumes that the initial cleft concentration is $c(r,0) = 0$ and $c(R,t) = c_0$.

In such case we write the solution in the form

$$\bar{c}(r,t) = c_0 + \sum_{m=1}^{\infty} A_m(t) J_0(\lambda_m r), \tag{4.70}$$

but as opposed to eqs. 4.50 and 4.51, invoking the initial conditions leads to

$$-c_0 = \sum_{n=1}^{\infty} A_n(0) J_0(\lambda_n r), \text{ and} \tag{4.71}$$

$$A_n(0) = -\frac{2c_0}{(\lambda_n R) J_1(\lambda_n R)}. \tag{4.72}$$

Other details are as worked out above for our original problem.

Chapter 5

Summary and Conclusions

5.1 Summary

The main goal of this dissertation was to provide new insight into number of fundamental cellular mechanisms. In Chapter 2, a realistic model of cell adhesion and the development of traction force was presented. There it was demonstrated how the substrate's physical characteristics such as stiffness and time-dependent force response are felt all along the cell adhesome, as opposed to being seen to be localized at a single anonymous site. The effects of the rate of retrograde flow of the actin cytoskeleton are also detailed in a novel manner and revealed a number of effects not yet noted. In addition, to our knowledge, new insights are introduced concerning the role of substrate stiffness and time-dependent response on the density of integrin clusters and thereby on traction force levels possible. Model parameters are discussed in terms of what is required for truly predictive capability of traction stress.

In Chapter 3, we present a flexible and adaptable model to address the basic clustering nature of nascent adhesion formation. Nascent adhesions are the common forerunner to the formation of focal adhesions that are a fundamental mechanism for cell adhesion necessary for cell proliferation, migration, and mechanotransduction. The model we present provides a clear explanation of how these conserved clustering features come about. Our model is based on the interaction among ligated and un-ligated integrins that arise due to deformations that are induced in the cell membrane/glycocalyx and substrate system due to integrin activation and ligation. Our simulations reveal effects of various key parameters related to integrin activation and ligation as well as some unexpected and previously unappreciated effects of parameters including integrin mobility and substrate rigidity.

In chapter 4, we examine the significance of advection in the transport within thin biological gaps. The process driven by stochastic fluid flow caused by random thermal structural motion, and we compare it with transport via diffusion. The model geometry chosen resembles the synaptic cleft, which allows for well-defined mechanical and physical features that control the advection process. Our analysis defines a Péclet-like number, $\mathcal{A}^D$, that quantifies the ration of time scales of advection versus diffusion. Another parameter, $\mathcal{A}^M$, is also defined by the analysis that quantifies the full potential extent of advection in the absence of diffusion. These parameters provide a clear and compact description of the interplay among the well-defined structural, geometric, and physical properties *vis-á-vis* the advection versus diffusion process. Our model analysis thus provide unambiguous insight into the prospect of competition of advection versus diffusion within biological gap-like structures.

5.2 Conclusions

1. A number of notable features of force transmission along the adhesome is presented. The effects of mechanosensitivity appear all along the force train. These effects are directly related to the time rate of force development, as seen in the behavior of both talin and integrin bonding.

2. Various parameters and elements of our cell adhesome model play important roles in the development of traction force and stress. Both "clutch bonds" and "catch bonds" theoretical framework are considered in our analysis model.

3. Estimation of traction stress in cell adhesome is attempted, and the need for quantitative study on integrin density, integrin-ligand bond survival, and integrin distribution is illustrated.

4. A framework for the formation of nascent adhesions based on reported phenomenology is presented. The framework of our model allows wide flexibility with regard to including additional features such as,1) patterned ligand distributions; 2) variable integrin mobility; 3) kinetic descriptions of ligation and unligating; and 4) the influence of "applied forces" as may arise due to actin-myosin contractility, by simply extending the model to include actin-myosin forces, the evolution of mature may be explored.

5. The driving force for clustering adhesion molecules coming about from the energy reductions is illustrated by the attractive pairwise forces that exists between integrins. The attracting force do not depend strongly on the system rigidity(stiffness), however, the force within an integrin does depend on system rigidity and that will affects ligation bond survival time.

6. Our simulations reveal important quantitative and qualitative effects of integrin mobility. For example, clusters tend to be larger when the mobility of unligated integrins is increased. It is recommend that experimental studies of clustering should also report this information to be adequate.

7. Our model for motion driven advection-diffusion demonstrates that when advection is driven by structural motion, the competition with diffusion must be accounted for to explain a range of phenomena. We show that the effect of advection becomes significant when $D \leqslant 10^{-13} m^2 s^{-1}$ with fluid velocities of order $\mathcal{O}(0.5 \mu m s^{-1})$.

8. Our analysis demonstrate unambiguous insight into the prospect of competition of advection versus diffusion within biological gap-like structures. The importance

of the random versus a regular, nature of structural motion and of the resulting transient nature of advection under random motion is made clear in our analysis.

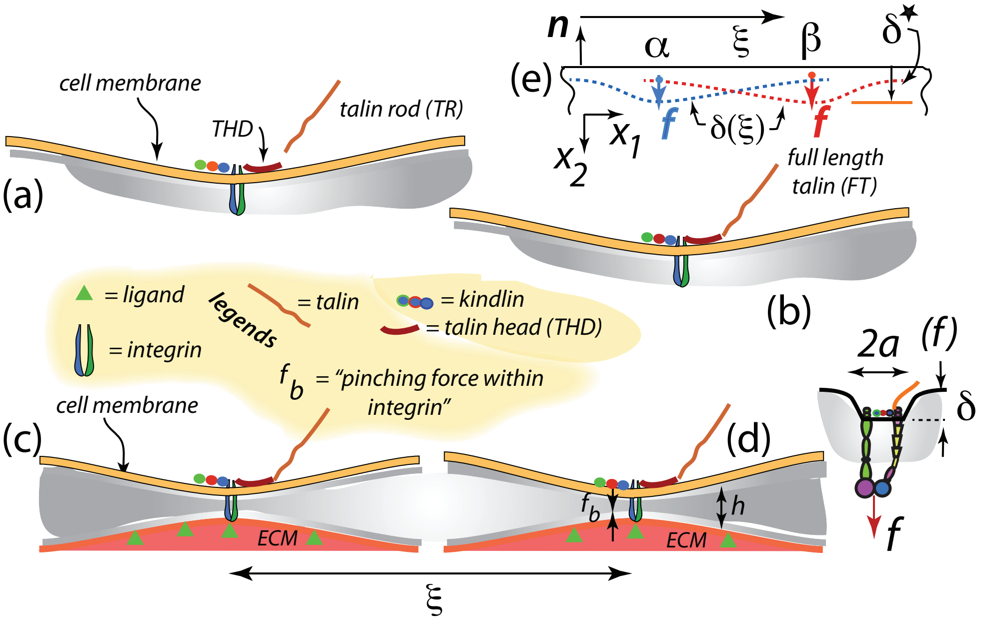

Figure 5.1. (a) THD and kindlins associate with the integrin β tail causing membrane distortion. (b) TR re-associates with THD and connects to actin cytoskeleton *via* vinculin (shown in Fig. 3.2c-d). (c,d) Two nearby and activated integrins, ligated or not, that interact via the deformation fields created by membrane distortion. (e) Integrins viewed as point forces, f, causing distortions; the distortions caused by each alone are sketched by the respective colored dashed lines. Note the displacement downward, $u_2(\xi)$ is called $\delta(\xi;\delta_0)$ where δ_0 is the maximum displacement beneath each point force. For a system modeled as linear elastic $\delta_0 = 1/kf$, k being a specific model dependent constant, and the total displacement is the linear sum of each dashed line. (f) A circular patch uniformly depressed, with a net force f_b, where $f_b = k\delta_0$ if this patch is not affected by other integrins.

5.3 Outstanding issues and future studies

As noted in the introduction to Chapter 3, nascent adhesions tend to have a transient lifetime, that is if they do not mature into focal adhesions [63]. Focal adhesions are connected to the actin cytoskeleton and experience the force stabilizing influence of the skeleton's retrograde flow, as depicted in Fig. 1.1. However, in time nascent adhesions tend to dissipate (disappear). It is reported that they persist for longer times on more compliant substrates. The mechanism for their disappearance is, as yet, unclear and is, therefore, an important object of future study. Some preliminary ideas follow below.

The initial setup in Fig. 5.2 illustrates a typical distribution of nascent adhesion clusters; the parameters are listed in the figure and for comparison they reflect the case shown in Fig. 3.8 Case 2 of Chapter 3. We recall what essentially drives the clustering process. When integrins activate and bind to ECM ligands, they induce a deformation of the cell membrane and glycocalyx as well as possibly the ECM. The deformation of cell membrane creates the pairwise internal attraction force within the integrins and an elastic deformation field as sketched in Fig. 5.1. Thus, these interaction forces promotes the integrin clustering.

Since the cell's glycocalyx as well as the membrane/skeleton complex is visco-elastic, we expect that with time relaxation will reduce the level of force that exists within ligated integrins, we have modeled this as a reduction in δ^*. Of the key parameters involved in time relaxation process, the pre-force, f_0^b , is released to zero since there is no "pinching force" when membrane relaxation; the $D_{ligated}$ is increased to near the order of $D_{unligated}$ due to the relaxation. Considering that the net displacement caused by all other integrins would also be limited due to the relaxation, the diffusion coefficient, D would increase as such the ligated integrins would behave more like un-ligated integrins in the time relaxation nature.

Figure 5.2 shows results for a compatible set of cases as where δ^* is assumed to be released as indicated by the values in the figures. As the relaxation of the membrane/skeleton happens, nascent clusters start to disappear overtime. We can tell, as expected, the nascent clusters fade away faster when the value of δ^* is lower. Note that the interaction force is decreased with δ^*. Although the effect of relaxation time difference is hard to tell in the preliminary results by comparing cases below, from the Maxwell-Wiechert model for visco-elastic materials, relaxation time is proportional to $1/E$. This agrees with what

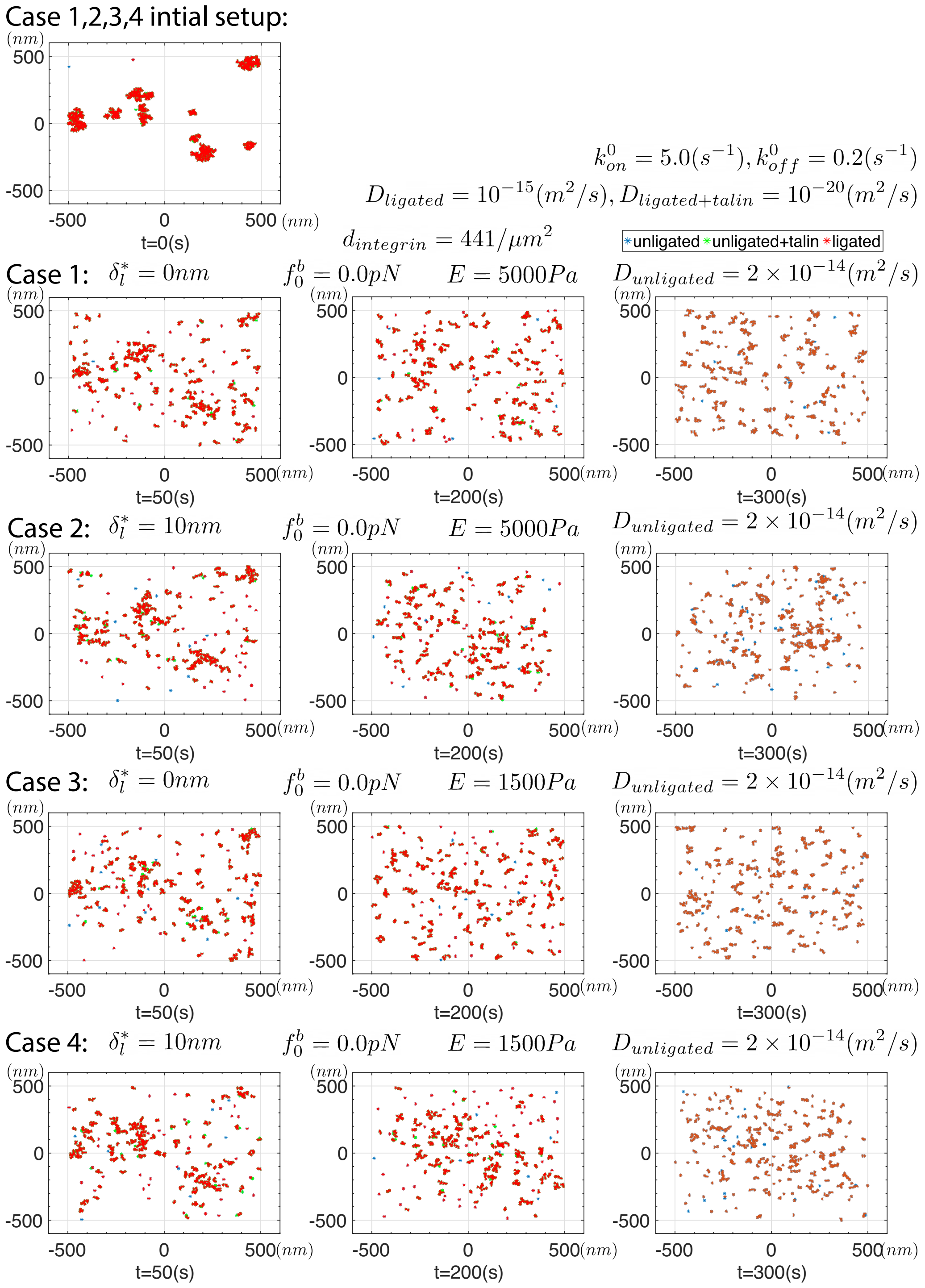

Figure 5.2. Results for a series of simulations where δ^* is released to indicated values; the frames are snapshots of a continuous simulation. All parameters are listed for the 4 cases considered. The initial integrins distribution is shown in the upper left.

Changede *et al.* [63] mentioned that nascent clusters tended to be less persistent on stiff, *viz.* glass, substrates than on less rigid, *viz.* supported lipid bilayer.

Notwithstanding the relatively limited experiment data supported, these preliminary results offer valuable insights into the nascent clusters dissipate mechanism. Further experimental investigations are needed to estimate and provide more definitive evidence. These new experimental studies should document the magnitudes of integrin mobility, *i.e* diffusion rates, as this is seen here to be an important factor.

Further research could usefully explore how the morphology and topology of extracellular matrix(ECM) could affect the cell adhesions. The results of Maheshwari *et al.* [103] are most relevant here in that they demonstrated how fibroblast cell adhesion depended quite sensitively on ligand cluster patterns as well as on overall ligand density. Also, the work of Changede *et al.* [191] showed that ligand geometry is an important factor in cluster formation and cell spreading. They find that initial nanoclusters form on "less dense ligand" substrates can not mature into regular focal adhesions. One possible explanation proposed by Changede *et al.* is that the liganded integrins are unable to support forces on unliganded integrins; activate integrins but unligated integrins could also participate in focal adhesion formations. To verify this possible hypothesis, we must explore the behavior of the clusters into mature focal adhesions. A reasonable approach to tackle this topics could be discuss below.

Follow the nascent adhesion clustering model framework in chapter 3, we can further include the actin-myosin forces into the nascent clusters with our adhesome's force train in chapter 2. Notice that the ligands are assumed to be affluent in chapter 3, ligand densities are not considered. To consider the effect of ligand densities, we might restrain integrins cannot be ligated in certain regions. On the other hand, the component of talin dimer must be considered here. Noted that two end of talin dimer cannot be bound under a certain distance, or it might break the dimer; unliganded integrins can still bind with talin dimer, but are unable to support forces. With these modification on the model, we should be able to reproduce the experiment results and provide some insights on the role of morphology and topology of ECM in adhesion formation.

Bibliography

[1] M. Yao, B. T. Goult, H. Chen, P. Cong, M. P. Sheetz, and J. Tan. Mechanical activation of vinculin binding to talin locks talin in an unfolded conformation. *Sci. Rep*, 4:4610–4621, 2014.

[2] M. Yao, B. T. Goult, B. Klapholtz, X. Hu, C. P. Toseland, Y. Guo, P. Cong, M. P. Sheetz, and J. Yan. The mechanical response of talin. *Nature Comm*, 7:11966, 2016.

[3] F. Kong, A. J. Garcia, A. P. Mould, M. J. Humphries, and C. Zhu. Demonstration of catch bonds between an integrin and its ligand. *J. Cell Biol*, 185:1275–1284, 2009.

[4] A. Elosegui-Artola, E. Bazellères, M. D. Allen, I. Andreu, R. Oria, R. Sunyer, J. J. Gomm, J. F. Marshall, J. L. Jones, X. Trepat, and P. Roca-Cusachs. Rigidity sensing and adaptation through regulation of integrin types. *Nature Mater*, 13(6):631–637, 2014.

[5] J. Li, Y. Su, W. Xia, M. J. Humphries, D. Vestweber, C. Caba nas, C. Lu, and T. A. Springer. Conformational equlibria and intrinsic affinities define integrin activation. *EMBO J.*, 36:629–645, 2017.

[6] D. L. Huang, N. A. Bax, C. D. Buckley, W. I Weis, and A. Dunn. Vinculin forms a directionally asymmetric catch bond with f-actin. *Science*, 357:703–706, 2017.

[7] B. Klapholz and N. H. Brown. Talin - the master of integrin adhesions. *J. Cell Sci*, 130:2435–2446, 2017.

[8] P. Roca-Cusachs, T. Iskratsch, and M. P. Sheetz. Finding the weakest link - exploring integrin-mediated mechanical molecular pathways. *J. Cell Biol*, 125:3025–3038, 2012.

[9] R. Zaidel-Bar, S. Itzkovitz, A. Ma'ayan, R. Iyengar, and B. Geiger. Functional atlas of the integrin adesome. *Nat. Cell Biol*, 9:858–867, 2007.

[10] M. S. Lord, M. Foss, and F. Besenbacher. Influence of nanoscale surface topography on protein adsorption and cellular response. *Nano Today*, 5:66–78, 2010.

[11] M. Alessandro, L. Hanqing, and J. Greer. Three-dimensional nano-architextured scaffolds with tunable stiffness for efficient bone tissue growth. *Acta Biomaterialia*, 63:294–305, 2017.

[12] A.E. Medvedev, A. Neumann, H.P. Ng, R. Lapovok, C. Kasper, T.C. Lowe, V.N. Anumalasetty, and Y. Estrin. Combined effect of grain refinement and surface modification of pure titanium on the attachment of mesenchymal stem cells and osteoblast-like saos-2 cells. *Materials Science and Engineering: C*, 71:483–497, 2017.

[13] T. J. Webster and J. U. Ejiofor. Increased osteoblast adhesion on nanophase metals: Ti, ti6al4v, and cocrmo. *Biomaterials*, 25:4731–4739, 2004.

[14] M. J. Dalby, M. O. Riehle, H. Johnstone, S. Affrossman, and A. S. G. Curtis. In vitro reaction of endothelial cells to polymer demixed nanotopology. *Biomaterials*, 23:2945–2954, 2002.

[15] M. J. Dalby, M. O. Riehle, D. S Sutherland, H. Agheli, and A. S. G. Curtis. Use of nanotopography to study mechanotransduction in fibroblasts - methods and perspectives. *Eur. J. Cell Biol*, 83:159–169, 2004.

[16] T. J. Webster, L. S. Schadler, R. W. Siegel, and R. Bizios. Mechanisms of enhanced osteoblast adhesion on nanophase alumina involve vitronectin. *Tissue Engineering*, 7(3):291–301, 2001.

[17] K. Rechendorff, M. B. Hovgaard, M. Foss, V. P. Zhdanov, and F. Besenbacher. Enhancement of protein adsorption induced by surface roughness. *Langmuir*, 22:10885–10888, 2006.

[18] A. S. G Curtis and M. Varde. Control of cell behavior: topological factors. *J of the National Cancer Institute*, 33:15–26, 1964.

[19] P. Atherton, B. Sttchbury, D. Y. Wang, D. Jethwa, R. Tsang, E. Meiler-Rodriqhez, P. Wang, N. Bate, R. Zent, I. L. Barsukov, B. T. Golut, D. R. Critchley, and C. Ballestram. Vinculin controls talin engagement with the actomyosin machinery. *Nature Comm*, 6:10038, 2015.

[20] A. R. Gingras, N. Bate, B. T. Goult, L. Hazelwood, I. Canestrelli, J. G. Grossman, N. Sm Putz H. Liu, G. Ck Roberts, N. Volkmann, D. Hanein, I. L. Barsukov, and D. R. Critchley. The structure of the c-terminal actin-binding domain of talin. *The EMBO J.*, 27:458–469, 2008.

[21] J. D. Humphries, P. Wang, C. Streuli, B. Geiger, M. J. Humphries, and C. Ballestrem. Vinculin controls focal adhesion formation by direct interactions with talin and actin. *J. Cell Biol*, 179:1043–1057, 2007.

[22] Armando Del Rio, Raul Perez-Jimenez, Ruchuan Liu, Pere Roca-Cusachs, Julio M Fernandez, and Michael P Sheetz. Stretching single talin rod molecules activates vinculin binding. *Science*, 323(5914):638–641, 2009.

[23] Qiang Zhu and Robert J Asaro. Spectrin folding versus unfolding reactions and rbc membrane stiffness. *Biophysical journal*, 94(7):2529–2545, 2008.

[24] J. H. Weiner. *Statistical Mechanics of Elasticity.* Dover, Mineola, NY, 1983.

[25] M. Gardel, B. Sabass, L. Ji, G. Danuser, U. S. Schwarz, and C. M. Waterman. Traction stress in focal adhesions correlates biphasically with actin retrograde flow speed. *J Cell Biol*, 183:999–1005, 2008.

[26] G. W. Fisher, P. A. Conrad, R. I. DeBiasio, and D. L. Taylor. Centripetal transport of cytoplasm, actin, and the cell surface in lamellipodia of fibroblasts. *Cell Motil. Cytoskeleton*, 11:235–247, 1988.

[27] P. Forscher and S. J. Smith. Actions of cytochalasins on the organization of actin filaments and microtubules in a neuronal growth cone. *J. Cell Biol*, 107:1505–1516, 1988.

[28] J. A. Theriot and T. J. Mitchison. Actin microfilament dynamics in locomoting cells. *Nature*, 352:126–131, 1991.

[29] G. Cuda, E. Pate, R. Cooke, and J. R. Sellers. In vitro actin filamenr sliding velocities oroduced by mixtures of different types of myosin. *Biophys. J.*, 72:1767–1779, 1997.

[30] Yuriy V Pereverzev, Oleg V Prezhdo, Manu Forero, Evgeni V Sokurenko, and Wendy E Thomas. The two-pathway model for the catch-slip transition in biological adhesion. *Biophysical journal*, 89(3):1446–1454, 2005.

[31] Paul A Janmey, Jessamine P Winer, Maria E Murray, and Qi Wen. The hard life of soft cells. *Cell motility and the cytoskeleton*, 66(8):597–605, 2009.

[32] Celeste M. Nelson, Ronald P. Jean, John L. Tan, Wendy F. Liu, Nathan J. Sniadecki, Alexander A. Spector, and Christopher S. Chen. Emergent patterns of growth controlled by multicellular form and mechanics. *Proceedings of the National Academy of Sciences*, 102(33):11594–11599, 2005.

[33] A. J. Engler, S. Sen, H. L. Sweeney, and D. E. Discher. Matrix elasticity directs stem cell linkage specification. *Cell*, 126:677–689, 2006.

[34] N. Gorfinkiel, G. B Blanchard, R. J. Adams, and A. Martinez Arias. Mechanical control of global cell behavior during dorsal closure in drosophila. *Development*, 136:1889–1898, 2009.

[35] T. Mammoto and D. E. Ingber. Mechanical control of tissue and organ development. *Development*, 137(9):1407–1420, 2010.

[36] S. Kumar and V. M. Weaver. Mechanics, malignancy, and metatasis: the force journey of a tumor cell. *Cancer Matastasis Rev*, 28:113–127, 2009.

[37] M. J. Paszek, N. Zahir, K. R. Johnson, J. N. Lakins, G. I. Rozenberg, and A. Gefen et al. Tensional homeostasis and the malignant phenotype. *Cancer Cell*, 8(3):241–254, 2005.

[38] C. S. Chen, M. Mrksich, S. Huang, G. M. Whitesides, and D. E. Ingber. Geometric control of cell life and death. *Science*, 276:1425–1428, 1997.

[39] M. Chrzanowska-Wodicka and K. Burridge. Rho-stimulated contractility drives the formation of stress fibers and focal adhesions. *J. Cell Biol*, 133:1403–1415, 1996.

[40] J. Folkman and A. Moscona. Role of cell shape in growth control. *Nature*, 273:354–359, 1978.

[41] G. Fenteany, P. A. Janmey, and T. P. Stossel. Signaling pathways and cell mechanics involved in wound closure by epithelial cell sheets. *Curr. Biol*, 10:831–838, 2000.

[42] A. Bruguès, A. Ester, V. Conte, J. H. Veldhuis, M. Gupta, J. Colombelli, J. J. Munõz, G. W. Brodland, B. Ladoux, and X. Trepat. Forces driving epithelial wound healing. *Nature Phys*, 10(9):683–690, 2014.

[43] N. Q. Balaban, U. S. Schwarz, D. Riveline, P. Goichberg, G. Tzur, D. Sabanay, S. Mahalu, S. Safran, A. Bershadsky, L. Addadi, and B. Geiger. Force and focal adhesion: a close relationship studied using elastic micropatterned substrates. *Nat Cell Biol*, 2:466–472, 2001.

[44] K. A. Beningo, M. Dembro, I. Kaverina, J. V. Small, and Y. L. Wang. Nascent focal adhesions are responsible for the generation of strong propulsive forces in migrating fibroblasts. *J. Cell Biol*, 153:881–888, 2001.

[45] A. D. Bershadsky, N. Q. Balaban, and B. Geiger. Adhesion-dependent cell mechanosensitivity. *Annu. Cell Dev Biol*, 19:677–695, 2003.

[46] J. P. Spatz Geiger, B. and A. D. Bershadsky. Environmental sensing through focal adhesions. *Nat. Rev. Mol. Cell Biol*, 10:21–33, 2009.

[47] S. E. Winograd-Katz, R. Fassier, R. Geiger, and K. R. Legate. The integrin adhesome: from genes and proteins to human disease. *Nat. Rev. Mol. Cell Biol*, 15:273–288, 2014.

[48] A. P. Maartens and N. H. Brown. Anchors and signals: the diverse roles of integrins in development. *Curr. Top. Dev. Biol*, 112:233–272, 2015.

[49] C. M. Lo, H. B. Wang, M. Dembro, and Y. L. Wang. Cell movement is guided by the rigidity of the substrate. *Biophys. J.*, 79:144–152, 2000.

[50] M. Saxena, L. Shuaimin, B. Yang, C. Hajal, R. Changede, J. Hu, H. Wolfenson, J. Hone, and M. P. Sheetz. Egfr and her2 activate rigidity sensing only on rigid matrices. *Nat Mater*, 16(7):775–781, 2017.

[51] K. Burridge and C. Guilly. Focal adhesions, stress fibers and mechanical tension. *Exp. Cell Res*, 343(1):14–20, 2016.

[52] H. B. Wang, M. Dembro, and Y. L. Wang. Substrate flexibility regulates growth and apoptosis of normal but not transformed cells. *Am J Physiol.*, 279(5):C1345–1350, 2000.

[53] William J Hadden, Jennifer L Young, Andrew W Holle, Meg L McFetridge, Du Yong Kim, Philip Wijesinghe, Hermes Taylor-Weiner, Jessica H Wen, Andrew R Lee, Karen Bieback, et al. Stem cell migration and mechanotransduction on linear stiffness gradient hydrogels. *Proceedings of the National Academy of Sciences*, 114(22):5647–5652, 2017.

[54] S. V. Plotnikov, A. M Pasapera, B. Sabass, and C. M. Waterman. Force fluctuations within focal adhesions mediate ecm-rigidity sensing to guide directed cell migration. *Cell*, 151(17):1–13, 2012.

[55] T. Yeung, P. C. Georges, L. A. Flanagan, B. Marg, M. Funaki M. Ortiz, N. Zahir, W. Ming, V. Weaver, and P. A. Janney. Effects of substrate stiffness on cell morphology, cytoskeleton structure, and adhesion. *Cell Motility and the cytoskeleton*, 60:24–34, 2005.

[56] W. E. Thomas, D. E. Discher, and V. P. Shastri. Mechanical regulation of cells by materials and tissues. *MRS Bull*, 35:578–583, 2010.

[57] A. M. Lipski, C. J. Pino, F. R. Haseiton, I. W. Chen, and V. P. Shastri. The effect of silica nanoscale-modified surfaces on cell morphology, cytoskeletal organization and function. *Biomaterials*, 29(28):3836–3846, 2008.

[58] A. J. Engler, C. Carag-Krieger, C. P. Johnson, M. Raab, H. Y. Tang, D. W. Speicher, J. W. Sanger, J. M. Sanger, and D. E. Discher. Embryonic cardiomyocytes beat best on a matrix with heart-like elasticity: scar-like rgiidity inhibits beating. *J Cell Sci*, 121(22):3794–3802, 2008.

[59] T. C. Lowe and R. A. Reiss. Understanding the biological responses of nanostructured metals and surfaces. *Mat Sci. and Engin. 012172*, 63, 2014.

[60] S. Bagherifard, R. Ghelichi, A. Khademhosseini, and M. Guagliano. Cell response to nanocrystallized substrates obtained through severe plastic deformation. *Applied Materials and Interfaces*, 6(11):7963–7985, 2014.

[61] E. R. Horton, J. D. Humphries, J. D. James, M. C. Jones, J. A. Askari, and M. J. Humphries. The integrin adhessome at a glance. *J. Cell Sci*, 129:4159–4163, 2016.

[62] C. Cluzel, F. Saltel, J. Lussi, F. Paulhe, B. A. Imhof, and B. Wehrle-Haller. The mechanisms and dynamics of αvβ3 integrin clustering in livibg cells. *J. Cell Biol*, 171:383–3392, 2005.

[63] R. Changede, X. Xu, F. Margadant, and M. P. Sheetz. Nascent integrin adhesions form on all matrix rigidities after integrin activation. *Developmental Cell*, 35:614–621, 2015.

[64] R. Changede and M. Sheetz. Integrin and cadherin clusters: a robust way to organize adhesions foe cell mechanics. *Bioessays*, 39:1–12, 2016.

[65] C. Ballestram, B. Hinz, B. E. Imhof, and B. Wehrle-Haller. Marching at the front and dragging behind: differential αvβ3- integrin turnover regulates focal adhesion behavior. *J. Cell Biol*, 155:1319–1332, 2001.

[66] P. W. Wiseman, C. M. Brown, D. J. Webb, B. Hebert, N. L. Johnson, J. A. Squier, M. H. Ellisman, and A. F. Horwitz. Spatial mapping of integrin interactions and dynamics during cell migration by image correlation microscopy. *J. Cell Sci*, 117:5521–5534, 2004.

[67] Pere Roca-Cusachs, Nils C Gauthier, Armando Del Rio, and Michael P Sheetz. Clustering of $\alpha 5\beta 1$ integrins determines adhesion strength whereas αvβ3 and talin enable mechanotransduction. *Proceedings of the National Academy of Sciences*, 106(38):16245–16250, 2009.

[68] L. Cao, J. Nicosia, J. Larouche, Y. Zhang, H. Bachman, A. C. Brown, L. Holmgren, and T. H. Barker. Detection of an integrin-binding mechanoswitch within fibronectin during tissue formation and fibosis. *ACS Nano*, 11(7):7110–7117, 2017.

[69] Matthew J Paszek, David Boettiger, Valerie M Weaver, and Daniel A Hammer. Integrin clustering is driven by mechanical resistance from the glycocalyx and the substrate. *PLoS Comput Biol*, 5(12):e1000604, 2009.

[70] A. Bachir, J. Zareno, K. Moissoglu, E. Plow, E. Gratton, and A. R. Horwitz. Integrin-associated complexes form hierarchically with variable stochiometry during nascent adhesion formation. *Curr. Biol*, 24(16):1845–1853, 2014.

[71] Colin K Choi, Miguel Vicente-Manzanares, Jessica Zareno, Leanna A Whitmore, Alex Mogilner, and Alan Rick Horwitz. Actin and α-actinin orchestrate the assembly and maturation of nascent adhesions in a myosin ii motor-independent manner. *Nature cell biology*, 10(9):1039–1050, 2008.

[72] O. Chaudhuri, L. Gu, M. Darnell, D. Klumpers, S. A. Bencherif, J. C. Weaver, N. Huebsch, and D. J. Mooney. Substrate stress relaxation regulates cell spreading. *Nat Commun*, 6:6364–6378, 2015.

[73] D. Lepzeiter and M. H. Zaman. Clustered diffusion of integrins. *Biophys. J.*, 99:L106–L108, 2010.

[74] Akihiro Kusumi, Chieko Nakada, Ken Ritchie, Kotono Murase, Kenichi Suzuki, Hideji Murakoshi, Rinshi S Kasai, Junko Kondo, and Takahiro Fujiwara. Paradigm shift of the plasma membrane concept from the two-dimensional continuum fluid to the partitioned fluid: high-speed single-molecule tracking of membrane molecules. *Annu. Rev. Biophys. Biomol. Struct.*, 34:351–378, 2005.

[75] E. S. Welf, U. P. Naik, and B. A. Ogunnaike. A spatial model for integrin clustering as a result of feedback between integrin activation and integrin binding. *Biophys. J*, 103:1379–1389, 2012.

[76] D. A. Calderwood. Talin controls integrin activation. *Biochem. Soc. Trans.*, 32:434–437, 2004.

[77] A. Smith, Y. R. Carrasco, P. Stanley, N. Kieffer, F. D. Batista, and N. Hogg. A talin-dependent lfa-1 focal zone is formed by rapidly migrating t lymphocytes. *J. Cell Biol*, 170:141–151, 2005.

[78] M. J. Paszek, C. C. DuFort, O. Rossier, R. Bainer, and J. K. Mouw et al. The cancer glycocalyx mechaincally primes integrin-mediated growth and survival. *Nature*, 511:319–324, 2014.

[79] W. Thomas, M. Forero, O. Yakovenko, L. Nilsson, P. Vicini, E. Sokurenko, and V. Vogel. Catch-bond model derived from allostery explains force-activated bacterial adhesion. *Biophys. J.*, 90:753–764, 2006.

[80] G. I. Bell, M. Dembro, and P. Bongrand. Competition between nonspecific and specific bonding. *Biophys J.*, 45:1051–1064, 1984.

[81] R. J. Asaro and V. A. Lubarda. *Mechanics of Solids and Materials.* Cambridge Univ Press, New York, 2006.

[82] L. D. Landau and E. M. Lifshitz. *Theory of Elasticity.* See Ch II) Pergamon Press, New York, 1959.

[83] C. V. Carman and T. A. Springer. Integrin avidity regulation: are changes in affinity and conformation underemphasized? *Curr. Opinion in Cell Biology*, 15:547–556, 2003.

[84] Jing Li and Timothy A Springer. Integrin extension enables ultrasensitive regulation by cytoskeletal force. *Proceedings of the National Academy of Sciences*, 114(18):4685–4690, 2017.

[85] Paul E Hughes, Federico Diaz-Gonzalez, Lilley Leong, Chuanyue Wu, John A McDonald, Sanford J Shattil, and Mark H Ginsberg. Breaking the integrin hinge: a defined structural constraint regulates integrin signaling. *Journal of Biological Chemistry*, 271(12):6571–6574, 1996.

[86] Tong-Lay Lau, Chungho Kim, Mark H Ginsberg, and Tobias S Ulmer. The structure of the integrin αiibβ3 transmembrane complex explains integrin transmembrane signalling. *The EMBO journal*, 28(9):1351–1361, 2009.

[87] F. Ye, G. Hu, D. Taylor, B. Ratnikov, A. A. Bobkov, M. A. McLean, S. G. Sligar, K. A. Taylor, and M. H. Ginsberg. Recreation of the terminal events in physilogical integrin activation. *J. Cell Biol*, 188:157–173, 2010.

[88] R. O'Callaghan, K. M. Job, R. O Dull, and V. Hlady. Stiffness and heterogeneity of the pulonary endothelial glycocalyx measured by atomic force microscopy. *Am. J. Physiol. Lung Mol. Physiol.*, 301(3):L353–L360, 2011.

[89] Q. Zhu, S. Salehyar, P. Cabrales, and R. J. Asaro. Prospects for human erythrocyte skeleton-bilayer dissociation during splenic flow. *Biophys J.*, 113:900–912, 2017.

[90] Nataliia Guz, Maxim Dokukin, Vivekanand Kalaparthi, and Igor Sokolov. If cell mechanics can be described by elastic modulus: study of different models and probes used in indentation experiments. *Biophysical journal*, 107(3):564–575, 2014.

[91] A. Kumar, M. Ouyang, K. van den Dries, E. J. McGhee, K. Tanaka, M. D. Anderson, A. Griosman, B. T. Goult, K. I. Anderson, and M. A. Schwartz. Talin tension sensor reveals novel features of focal adhesion force transmission and mechanosensitivity. *J Cell Biol*, 213:371–383, 2016.

[92] P. Atherton, F. Lausecker, Z. Miskolczi, A. Gilmore, I. Barsukov, and C. Ballestram. Activation mechanisms that control the association of the mechanosensors talin and vinculin. in-press. 2018.

[93] B. T. Marshall, M. Long, J. W. Piper, T. Yago, R. P. McEver, and C. Zhu. Direct observation of catch bonds involving cell-adhesion molecules. *Nature*, 423:190–193, 2003.

[94] K. K. Sarangapani, T. Yago, S. G. Klopocki, M. B. Lawrence, C. B. Fieger, S. D. Rosen, R. P. McEver, and C. Zhu. Low force decelerates l-selectin dissociation from p-selectin glycoprotein ligand-1 and endoglycan. *J. Biol. Chem*, 279:2291–2298, 2004.

[95] E. Evans, A. Leung, V. Heinrich, and C. Zhu. Mechanical switching and coupling between two dissociation pathways in a p-selectin adhesion bond. *PNAS*, 101:11281–11286, 2004.

[96] Denis Bartolo, Imre Derényi, and Armand Ajdari. Dynamic response of adhesion complexes: beyond the single-path picture. *Physical Review E*, 65(5):051910, 2002.

[97] R. I. Litinov, A. Mekler, H. Shuman, J. S. Bennett, V. Barsegov, and J. W. Weisel. Resolving two-dimensional kinetics of the integrin αIIbβ3-fibrinogen interactions using binding-unbinding correlation spectroscopy. *J. Biol. Chem*, 287:35275–35285, 2012.

[98] C. E. Chan and D. J. Odde. Traction dynamics of filopodia on compliant substrates. *Science*, 322:1687–1691, 2008.

[99] A. Elosegui-Artola, R. Oria, Y. Chen, A. Kosmalska, C. Perez-Gonzalez, N. Castro, C. Zhu, X. Trepat, and P. Roca-Cusachs. Mechanical regulation of a molecular clutch defines force transmission and tranduction in response to matrix rigidity. *Nature Cell Biol*, 18:540–548, 2016.

[100] S. Munevar, Y. L. Wang, and M. Dembro. Traction force microscopy of migrating normal and h-ras transformed 3t3 fibroblasts. *Biophys. J.*, 80:1744–1757, 2001.

[101] H. S. Lee, C. J. Lim, W. Puzon-McLaughlin, S. J. Shattil, and M. H. Ginsberg. Riam activates integrins by linking talin to ras gtpase membrane-targeting sequences. *J. Biol Chem*, 284:5119–5127, 2009.

[102] O. Chaudhuri, L. Gu, D. Klumpers, M. Darnell, S. A. Bencherif, J. C. Weaver, N. Huebsch, H. Lee, E. Lippens, G. N. Duda, and D. J. Mooney. Hydrogels with tunable stress relaxation regulate stem cell fate and activity. *Nat Mater*, 15(3):326–334, 2016.

[103] G. Maheshwari, G. Brown, D. A. Lauffenburger, A. Wells, and L. G. Griffith. Cell adhesion and motility depend on nanoscale rgd clustering. *J. Cell Sci*, 113:1677–1686, 2000.

[104] Erich Sackmann and Ana-Sunčana Smith. Physics of cell adhesion: some lessons from cell-mimetic systems. *Soft matter*, 10(11):1644–1659, 2014.

[105] Laetitia Seguin, Maria F Camargo, Hiromi I Wettersten, Shumei Kato, Jay S Desgrosellier, Tami von Schalscha, Kathryn C Elliott, Erika Cosset, Jacqueline Lesperance, Sara M Weis, et al. Galectin-3, a druggable vulnerability for kras-addicted cancers. *Cancer discovery*, 7(12):1464–1479, 2017.

[106] Jay S Desgrosellier and David A Cheresh. Integrins in cancer: biological implications and therapeutic opportunities. *Nature Reviews Cancer*, 10(1):9–22, 2010.

[107] David A Cheresh, John R Harper, Gregor Schulz, and Ralph A Reisfeld. Localization of the gangliosides gd2 and gd3 in adhesion plaques and on the surface of human melanoma cells. *Proceedings of the National Academy of Sciences*, 81(18):5767–5771, 1984.

[108] Xuan Cao, Yuan Lin, Tristian P Driscoll, Janusz Franco-Barraza, Edna Cukierman, Robert L Mauck, and Vivek B Shenoy. A chemomechanical model of matrix and nuclear rigidity regulation of focal adhesion size. *Biophysical journal*, 109(9):1807–1817, 2015.

[109] Xuan Cao, Ehsan Ban, Brendon M Baker, Yuan Lin, Jason A Burdick, Christopher S Chen, and Vivek B Shenoy. Multiscale model predicts increasing focal adhesion size with decreasing stiffness in fibrous matrices. *Proceedings of the National Academy of Sciences*, 114(23):E4549–E4555, 2017.

[110] Sam Walcott, Dong-Hwee Kim, Denis Wirtz, and Sean X Sun. Nucleation and decay initiation are the stiffness-sensitive phases of focal adhesion maturation. *Biophysical journal*, 101(12):2919–2928, 2011.

[111] Shijie He, Yewang Su, Baohua Ji, and Huajian Gao. Some basic questions on mechanosensing in cell–substrate interaction. *Journal of the Mechanics and Physics of Solids*, 70:116–135, 2014.

[112] Z. Sun, M. Costell, and R. Fässler. Integrin activation by talin, kindlin and mechanical forces. *Nature Cell Biol*, 21:25–31, 2019.

[113] M. Schvartzman, M. Palma, J. Sable, J. Abramson, et al. Nanolithographic control of the spatial organization of cellular adhesion receptors at the single-molecule level. *Nano Lett*, 11:1306–1312, 2011.

[114] E. A. Cavalcanti-Adam, D. Aydin, V. C. Hirechfeld-Warneken, and J. P. Spatz. Cell adhesion and response to synthetic nanopatterned environments by steering clustering and spatial location. *HFSP J.*, 2:276–285, 2006.

[115] D. F. Kucik. Rearrangement of integrins in avidity regulation by leukocytes. *Immunologic Res*, 26(1):199–206, 2002.

[116] Fabiana Martino, Ana R Perestrelo, Vladimír Vinarskỳ, Stefania Pagliari, and Giancarlo Forte. Cellular mechanotransduction: from tension to function. *Frontiers in physiology*, 9:824, 2018.

[117] H. Wolfenson, B. Yang, and M. P. Sheetz. Steps in mechanotransduction pathways that control cell morphology. *Annu. Rev. Physiol*, 81:585–605, 2019.

[118] Y. L. Dorland and S. Huveneers. Cell-cell junctional mechanotransduction in endothelial remodeling. *Cell Mol. Life Sci*, 74:279–292, 2017.

[119] S. J. Shattil, C. Kim, and M. H. Ginsberg. The final steps of integrin activation: the end game. *Nat. Rev. Mol. Cell Biol*, 11(4):288–300, 2010.

[120] D. R. Calderwood, R. Zent, R. Grant, D. Jasper, G. Rees, R. O. Hynes, and M. H. Ginsberg. The talin head domain binds to integrin β subunit cytoplasmic tails and regulates integrin activation. *J. Biol. Chem*, 274(40):28071–28074, 1999.

[121] B. Garcia-Alvarez, J. M. de Pereda, D. A. Calderwood, T. S. Ulmer, D. A. Critchley, I. D. Campbell, M. H. Ginsberg, and R. C. Liddington. Structural determinants of integrin recognition by talin. *Mol. Cell*, 11:49–58, 2003.

[122] D. A. Calderwood, I. D. Campbell, and D. R. Critchley. Talin and kindlins: partners in integrin-mediated adhesion. *Nat Rev Mol Biol*, 14(8):503–517, 2013.

[123] C. Kim, F. Ye, H. Xiaohui, and M. H. Ginsberg. Talin activates integrins by altering the topology of the β transmembrane domain. *J. Cell Biol*, 197(5):605–611, 2011.

[124] M. H. Ginsberg. Integrin activation. *BMB*, 47(12):655–659, 2014.

[125] X. Du, M. Gu, J. W. Weisel, C. Nagaswami, J. S. Bennett, R. Bowditch, and M. H. Ginsberg. Long range propagation of conformational changes in integrin $\alpha_{III}\beta_3$. *J. Biol. Chem*, 268:23087–23092, 1993.

[126] Marina Theodosiou, Moritz Widmaier, Ralph T Böttcher, Emanuel Rognoni, Maik Veelders, Mitasha Bharadwaj, Armin Lambacher, Katharina Austen, Daniel J Müller, Roy Zent, et al. Kindlin-2 cooperates with talin to activate integrins and induces cell spreading by directly binding paxillin. *Elife*, 5:e10130, 2016.

[127] Frédéric Saltel, Eva Mortier, Vesa P Hytönen, Marie-Claude Jacquier, Pascale Zimmermann, Viola Vogel, Wei Liu, and Bernhard Wehrle-Haller. New pi (4, 5) p2- and membrane proximal integrin–binding motifs in the talin head control β3-integrin clustering. *Journal of cell biology*, 187(5):715–731, 2009.

[128] B. Reynwar, G. Illya, V. A. Hamandaris, M. M. Mullër, K. Krermer, and M. Deserno. Aggregation and vesiculation of membrane proteins by curvature-mediated interactions. *Nature*, 447:461–464, 2007.

[129] B. Reynwar and M. Deserno. Membrane-mediated interactions between circular particles in strongly curved regieme. *Soft Matter*, 7:pp 8567, 2011.

[130] Casper Van Der Wel, Afshin Vahid, Anđela Šarić, Timon Idema, Doris Heinrich, and Daniela J Kraft. Lipid membrane-mediated attraction between curvature inducing objects. *Scientific reports*, 6(1):1–10, 2016.

[131] P. Kammerer, J. Aretz, and R. Fässler. Lucky kindlin: a cloverleaf at the integrin tail. *PNAS*, 114(35):0234–0236, 2017.

[132] K. L. Johnson. *Contact Mechanics*. Cambridge Univ Press, New York, NY, 2003.

[133] G. Goennenwein, M. Tanaka, B. Hu, L. Moroder, and E. Sackmann. Functional incorporation of integrins into solid supported membranes on unltrathin films of cellulose: impact on adhesion. *Biophys. J.*, 85:646–655, 2003.

[134] Z. Bagi, Y. Couch, Z. Broskova, F. Perez-Balderas, and T. Yeo. *et al.* Extracellular vesicle integrins act as a nexus for platelet adhesion in cerebral microvessels. Sci. Rep, 2019.

[135] P. Heitjans and J. Kärger. *Diffusion in Condensed Matter*. Springer, Heidelberg, 2005.

[136] A. C. Brànka and D. M. Heyes. Algorithms for brownian dynamics computer simulations: multivariable case. *Phys. Rev E*, 60:2381–2387, 1999.

[137] L. Sun, Q. H. Cheng, H. Gao, and Y. W. Zhang. Computational modeling for cell spreading on a substrate mediated by specific interactions, long-range recruiting interactions, and diffusion of binders. *Phys Rev E*, 79, 2009.

[138] T. Erdmann and U. S. Schwartz. Stability of adhesion clusters under constant force. *Phys. Rev Lett.*, 92(10):pp 108102, 2004.

[139] G. I. Bell. Models for the specific adhesion of cells to cells. *Science*, 200:618–627, 1978.

[140] M. Dembo, D. C. Torney, K. Saxaman, and D. A. Hammer. The reaction-limited kinetics of membrane-to-surface adhesion and detachment. In *Proc. R*, pages 55–83, Soc. Lond. B 234, 1988.

[141] Wendy Thomas. Catch bonds in adhesion. *Annu. Rev. Biomed. Eng.*, 10:39–57, 2008.

[142] Robert J Asaro, Kuanpo Lin, and Qiang Zhu. Mechanosensitivity occurs along the adhesome's force train and affects traction stress. *Biophysical journal*, 117(9):1599–1614, 2019.

[143] L. Sun, Q. H. Cheng, H. J. Gao, and Y. W. Zhang. Effect of loading conditions on the dissociation behavior of catch bond clusters. *J. R. Soc Interface*, 9:928–937, 2011.

[144] J. Qian and H. Gao. Soft matrices suppress cooperation behaviors among receptor-ligand bonds in cell adhesions. *PLoS ONE*, 5:pp e12342, 2010.

[145] B. H. Luo, K. Strokovich, T. Walz, and T. A. Springer. Allosteric β_1 integrin antibodies that stabilize the low affinity state by preventing the swingout of the hybrid domain. *J. Biol. Chem*, 279:27466–27471, 2004.

[146] B. Alberts, A. Johnson, J. Lewis, M. Raff, K. Roberts, and P. Walter. *The Cell*. Garland Science, 2002.

[147] Sheldon Weinbaum, John M Tarbell, and Edward R Damiano. The structure and function of the endothelial glycocalyx layer. *Annu. Rev. Biomed. Eng.*, 9:121–167, 2007.

[148] J. M. Soler, S. Desplat-Jego, B. Vacher, L. Ponsonnet, and M. Fraterno. et al. *Adhesion-related glycocalyx study: quantitative approach with imaging-spectrum in the energy filtering transmission microscope (EFTEM). FEBS Lett*, 429:89–94, 1998.

[149] J. M. Squire, M. Chew, G. Nneji, C. Neal, and J. Barry et al. Quasi-periodic substructure in the microvessel endothelial glycocalyx: a possible explanation for molecular filtering. *J. Struct Biol*, 136:239–255, 2001.

[150] G. J. Bakker, C. Eich, J. A. Torreno-Pina, R. Diez-Ahedo, G. Perez-Samper, T. S. van Zanten, C. G. Figdor, A. Cambi, and M. F. Garcia-Parajo. Lateral mobility of individual integrin nanoclusters orchestrates the onset for leukocyte adhesion. *PNAS*, 109:4869–4874, 2012.

[151] Robert L Yauch, Dan P Felsenfeld, Stine-Kathrein Kraeft, Lan Bo Chen, Michael P Sheetz, and Martin E Hemler. Mutational evidence for control of cell adhesion through integrin diffusion/clustering, independent of ligand binding. *The Journal of experimental medicine*, 186(8):1347–1355, 1997.

[152] Olivier Rossier, Vivien Octeau, Jean-Baptiste Sibarita, Cecile Leduc, Béatrice Tessier, Deepak Nair, Volker Gatterdam, Olivier Destaing, Corinne Albiges-Rizo, Robert Tampé, et al. Integrins β 1 and β 3 exhibit distinct dynamic nanoscale organizations inside focal adhesions. *Nature cell biology*, 14(10):1057–1067, 2012.

[153] Ernest H. Starling. On the absorption of fluids from the connective tissue spaces. *The Journal of Physiology*, 19(4):312–326, 1896.

[154] Morton H Friedman. *Principles and models of biological transport*. Springer Science & Business Media, 2008.

[155] Jared M. Diamond and William H. Bossert. Standing-Gradient Osmotic Flow : A mechanism for coupling of water and solute transport in epithelia . *Journal of General Physiology*, 50(8):2061–2083, 09 1967.

[156] Maiken Nedergaard. Garbage truck of the brain. *Science*, 340(6140):1529–1530, 2013.

[157] S R Chary and R K Jain. Direct measurement of interstitial convection and diffusion of albumin in normal and neoplastic tissues by fluorescence photobleaching. *Proceedings of the National Academy of Sciences*, 86(14):5385–5389, 1989.

[158] Leonid P. Savtchenko and Dmitri A. Rusakov. The optimal height of the synaptic cleft. *Proceedings of the National Academy of Sciences*, 104(6):1823–1828, 2007.

[159] JD Clements, RA Lester, G Tong, CE Jahr, and GL Westbrook. The time course of glutamate in the synaptic cleft. *Science*, 258(5087):1498–1501, 1992.

[160] B. Corti. *Osservazione microscopishe sulla tremella e sulla cirulazione del fluido in una planta acquaguola. Lucca.* Appresso Giuseppe Rocchi, Lucca, Italy, 1774.

[161] W. F. PICKARD. The role of cytoplasmic streaming in symplastic transport. *Plant, Cell & Environment*, 26(1):1–15, 2003.

[162] Raymond E. Goldstein and Jan-Willem van de Meent. A physical perspective on cytoplasmic streaming. *Interface Focus*, 5(4):20150030, 2015.

[163] Motoki Tominaga and Kohji Ito. The molecular mechanism and physiological role of cytoplasmic streaming. *Current Opinion in Plant Biology*, 27:104–110, 2015. Cell signalling and gene regulation.

[164] Yuji Kimura, Nobutada Toyoshima, Noboru Hirakawa, Keiichirou Okamoto, and Akihiko Ishijima. A kinetic mechanism for the fast movement of chara myosin. *Journal of Molecular Biology*, 328(4):939–950, 2003.

[165] Teruo Shimmen and Etsuo Yokota. Cytoplasmic streaming in plants. *Current Opinion in Cell Biology*, 16(1):68–72, 2004.

[166] Albert Fannjiang and George Papanicolaou. Convection-enhanced diffusion for random flows. *Journal of Statistical Physics*, 88(5):1033–1076, 1997.

[167] Leonid Piterbarg and A Ostrovskii. *Advection and diffusion in random media: implications for sea surface temperature anomalies.* Springer Science & Business Media, 1997.

[168] Elena F Koslover, Caleb K Chan, and Julie A Theriot. Disentangling random motion and flow in a complex medium. *Biophysical journal*, 110(3):700–709, 2016.

[169] Thomas A Nielsen, David A DiGregorio, and R Angus Silver. Modulation of glutamate mobility reveals the mechanism underlying slow-rising ampar epscs and the diffusion coefficient in the synaptic cleft. *Neuron*, 42(5):757–771, 2004.

[170] Dmitri A Rusakov. The role of perisynaptic glial sheaths in glutamate spillover and extracellular ca2+ depletion. *Biophysical journal*, 81(4):1947–1959, 2001.

[171] Knut Petter Lehre and Dmitri A Rusakov. Asymmetry of glia near central synapses favors presynaptically directed glutamate escape. *Biophysical journal*, 83(1):125–134, 2002.

[172] David J Acheson. Elementary fluid dynamics, 1991.

[173] Constantine Pozrikidis and D Jankowski. *Introduction to theoretical and computational fluid dynamics*, volume 675. Oxford university press New York, 1997.

[174] Ted Bennett. *Transport by advection and diffusion.* Wiley Global Education, 2012.

[175] Nicolaas Godfried Van Kampen. *Stochastic processes in physics and chemistry*, volume 1. Elsevier, 1992.

[176] Martina Pannuzzo, Antonio Grassi, and Antonio Raudino. Hydrodynamic enhancement of the diffusion rate in the region between two fluctuating membranes in close opposition: A theoretical and computational study. *The Journal of Physical Chemistry B*, 118(29):8662–8672, 2014.

[177] Patrick Tabeling. *Introduction to microfluidics.* OUP Oxford, 2005.

[178] AMJ Davis. Stokes drag on a disk sedimenting toward a plane or with other disks; additional effects of a side wall or free surface. *Physics of Fluids A: Fluid Dynamics*, 2(3):301–312, 1990.

[179] G. Falkovich, S. Musacchio, L. Piterbarg, and M. Vucelja. Inertial particles driven by a telegraph noise. *Phys. Rev. E*, 76:026313, Aug 2007.

[180] J Rogel-Salazar. Statistical mechanics, 3rd edn., by rk pathria and pd beale: Scope: textbook. level: postgraduate or advanced undergraduate, 2011.

[181] S.K. Ma. *Statistical Mechanics*. World Scientific, 1985.

[182] Divya Pathak, Lauren Y Shields, Bryce A Mendelsohn, Dominik Haddad, Wei Lin, Akos A Gerencser, Hwajin Kim, Martin D Brand, Robert H Edwards, and Ken Nakamura. The role of mitochondrially derived atp in synaptic vesicle recycling. *Journal of Biological Chemistry*, 290(37):22325–22336, 2015.

[183] Vidhya Rangaraju, Nathaniel Calloway, and Timothy A Ryan. Activity-driven local atp synthesis is required for synaptic function. *Cell*, 156(4):825–835, 2014.

[184] Donald Voet, Judith G Voet, and Charlotte W Pratt. *Fundamentals of biochemistry: life at the molecular level*. John Wiley & Sons, 2016.

[185] Jiri Pokornỳ, Filip Jelínek, V Trkal, Ingolf Lamprecht, and R Hölzel. Vibrations in microtubules. *Journal of Biological Physics*, 23(3):171–179, 1997.

[186] YongKeun Park, Catherine A. Best, Thorsten Auth, Nir S. Gov, Samuel A. Safran, Gabriel Popescu, Subra Suresh, and Michael S. Feld. Metabolic remodeling of the human red blood cell membrane. *Proceedings of the National Academy of Sciences*, 107(4):1289–1294, 2010.

[187] Elise Spedden, James D White, Elena N Naumova, David L Kaplan, and Cristian Staii. Elasticity maps of living neurons measured by combined fluorescence and atomic force microscopy. *Biophysical journal*, 103(5):868–877, 2012.

[188] Mirela Mustata, Ken Ritchie, and Helen A. McNally. Neuronal elasticity as measured by atomic force microscopy. *Journal of Neuroscience Methods*, 186(1):35–41, 2010.

[189] Edward A Swabb, James Wei, and Pietro M Gullino. Diffusion and convection in normal and neoplastic tissues. *Cancer research*, 34(10):2814–2822, 1974.

[190] Thomas Bickel. Brownian motion near a liquid-like membrane. *The European Physical Journal E*, 20(4):379–385, 2006.

[191] Rishita Changede, Haogang Cai, Shalom J Wind, and Michael P Sheetz. Integrin nanoclusters can bridge thin matrix fibres to form cell–matrix adhesions. *Nature materials*, 18(12):1366–1375, 2019.